Non-equilibrium dynamics of bacterial colonies

Inaugural-Dissertation

zur
Erlangung des Doktorgrades
der Mathematisch-Naturwissenschaftlichen Fakultät
der Universität zu Köln
vorgelegt von

Kai Zhou
aus Henan, China

Köln
2023

The dissertation has been accepted by the Faculty of Mathematics and Natural Sciences of the University of Cologne in 2024.

Date of the Submission: December 18, 2023

Date of the Oral Examination: March 25, 2024

Berichterstatter: **Prof. Dr. Benedikt Sabass**
(Gutachter) **Prof. Dr. Tobias Bollenbach**

Abstract

Colonies of bacteria endowed with a pili-based self-propulsion machinery are ideal models for investigating the structure and dynamics of active many-particle systems. We study *Neisseria gonorrhoeae* colonies with a molecular-dynamics-based approach. A generic, adaptable simulation method for particle systems with fluctuating bond-like interactions is devised. In a first study, the simulations are employed to investigate growth of bacterial colonies and the dependence of the colony structure on cell-cell interactions. In colonies, pilus retraction enhances local ordering. For colonies consisting of different types of cells, the simulations show a segregation depending on the pili-mediated interactions among different cells. These results agree with experimental observations. Next, we quantify the power-spectral density of colony-shape fluctuations *in silico*. Simulations predict a strong violation of the equilibrium fluctuation-response relation. Furthermore, we show that active force generation enables colonies to spread on surfaces and to invade narrow channels. The methodology can serve as a foundation for future studies of active many-particle systems at boundaries with complex shape.

Bacterial colonies can attach and wet on surfaces like liquid droplets. Little is known about what factors affect the wetting of bacterial colonies. In a second study, we combine experimental data with our particle-based simulations and analytical calculations to show that azithromycin treatment enhances the wettability of *Neisseria gonorrhoeae* colonies. We show that the steady-state contact angle is not only determined by parameters that determine an equilibrium state, but also depends on dynamical quantities like the friction constant. Thus, surface-wetting of *Neisseria gonorrhoeae* colonies is a genuine non-equilibrium process. The thickness of the diffuse interface of the colonies is non-negligible compared to the colony radius, which gives rise to a finite Tolman length and a contact angle that depends on the size of the colony. The spreading dynamics is changed with azithromycin treatment, different spreading power laws are shown.

In a third study, we investigate the dynamics of colonies consisting of two types of bacteria. In certain growth conditions, one finds experimentally that bacteria inside of the colony change the dynamics of their pili and become less adhesive. In simulations, we show that the configuration of such mixed colonies can become unstable, leading to a rapid folding and reorganization of the colony structure, which one can interpret as a non-equilibrium capillary instability.

In a fourth study, we investigate bacterial colonies directionally migrate on geometrically asymmetric surfaces. The binding of bacterial pili to the asymmetric surfaces generates unbalanced forces, which drive the colony to migrate forward.

Overall, we have demonstrated the versatility and predictive power of particle-based simulations of bacteria, which enable the discovery of novel non-equilibrium phenomena in bacterial collectives.

Acknowledgements

I would like to sincerely thank the members of my thesis defense committee. I am deeply grateful to two reviewers, Prof. Dr. Benedikt Sabass and Prof. Dr. Tobias Bollenbach, for taking the time to review this thesis. I would like to thank Prof. Dr. Peter Schilke for chairing the defense committee and Dr. Joscha Mecke for being the minutes taker.

I am very grateful to my supervisor, Prof. Dr. Benedikt Sabass, without you this thesis could not have been completed. Thank you for giving me the opportunity to work with you. Thank you for guiding my research projects, providing ideas and figuring out how to make them happen. Thank you for instructing me how to write a well-structured paper. Thank you for your patience and enthusiastic support throughout my doctoral journey.

I would like to express warm thanks to Prof. Dr. Gerhard Gompper, director of the Theoretical Physics of Living Matter (IBI-5/IAS-2) group at Forschungszentrum Jülich. Thank you for the helpful and enjoyable discussions during lunchtime. I appreciate the opportunity you provided for me to give a presentation in the group.

I would also like to thank all the great colleagues in this group. Special thanks for the discussions with Dr. Dmitry Fedosov, Dr. Marisol Ripoll and Dr. Thorsten Auth. Appreciation for the discussions and chats with Joscha, Yunfei, Zihan, Chaojie, Kai Qi, Bohan, Rajendra, Sameh, Segun, Rodrigo, Ahmet and others. Thank you for your help and the good times we have had together.

Many thanks to Prof. Dr. Berenike Maier and Dr. Marc Hennes at the University of Cologne for carrying out experiments and providing experimental data. Thanks for many discussions with you that helped us to solve many questions. Appreciation for the ideas you suggested for experiments, analysis and simulations.

I would like to thank Prof. Dr. Christine Selhuber-Unkel and Malin Schmidt at the Heidelberg University for designing and carrying out the experiments for us.

I sincerely thank all my family members for their full support.

Kai Zhou
Forschungszentrum Jülich

December 2023

Contents

List of Figures

List of Tables

To my family...

Chapter 1

Introduction

1.1 Motility of bacteria

In many organisms, motility plays a crucial role for the acquisition of resources and the dispersal of their offspring. Bacteria, in particular, have developed diverse motility mechanisms to exploit available resources and environments, ultimately facilitating their colonization. These mechanisms can be categorized into two main classes: the first involves the uninhibited swimming of bacteria in aqueous solutions, while the second class comprises various types of motion across solid surfaces within aqueous environments [1].

1.1.1 Surface motility

The common motility of bacteria on surfaces can be categorized into swimming, swarming, gliding, twitching, and sliding [1–3], as shown in Fig. 1.1. Swarming motility can be defined as a rapid collective movement of bacteria across a surface, facilitated by the coordinated action of rotating flagella. Notably, swarming, as observed in bacteria like *Proteus*, represents a form of collective movement, while swimming is an individual behavior. Both swimming and swarming modes of bacterial motility rely on flagella for propulsion, but they operate in different environments. Swimming can occur in a three-dimensional liquid medium, while swarming takes place in a quasi-two-dimensional context on a solid surface. Swarming requires the formation of a thin liquid layer on the surface for cells to participate in this collective movement. This necessary condition for the movement of fluid at the boundary emphasizes the need for particular chemical elements, like osmolytes or surfactants, to be in close proximity to the forefront of the bacterial colony [1].

Bacterial twitching motility is driven by the attachment of their type IV pili (T4P) to a surface. In the case of *Neisseria gonorrhoeae*, these bacteria do not exhibit active swimming in a liquid medium or the ability to sense chemical gradients [4]. Instead, their mechanism of surface twitching motility is mediated by the retraction of T4P [5–7]. Additionally, the twitching motility of bacteria on surfaces can be influenced by the topography of the substrate [8–10].

Sliding motility is an expansive movement for a colony growing on a surface, and it is a passive form of surface spreading [2, 3]. This mode of motility does not rely on the involvement of an active motor. During sliding, certain bacterial species produce surfactants that effectively reduce surface tension. This reduction in surface tension contributes to the overall spreading movement. The spreading speed of the colony front during sliding ranges from $0.03\,\mu\mathrm{m/s}$ to $6\,\mu\mathrm{m/s}$ [2].

1.1.2 Type IV pili-driven migration in detail

Filamentous appendages known as pili are a common feature of many bacterial species. There are several different types of pili, including type IV pili (T4P), chaperone-usher pili (CUP fimbria) and so on [11]. A important role of typie IV pili in some organisms like is to facilitate adherence to host cells and abiotic surfaces, as well as adherence to other bacteria. Other, often essential functions of pili include the facilitation of DNA uptake in competent bacteria.

T4P are helical polymers characterized by a diameter ranging from 5 to 8 nm and a remarkable length of several micrometers. The main structural component of these pili is the major pilin, identified by the protein names PilE or PilA, as shown in Fig. 1.2. The assembly of a pilus polymer is composed of a large number of pilin subunits, with each individual pilin subunit within the pilus being approximately 0.8 nm in length. These pilin subunits are typically stored within the inner membrane of the bacterium. The crucial process of T4P polymerization is enabled by an ATPase, specifically either PilF or PilB, located in the cytoplasm [10]. T4P undergo polymerization and depolymerization processes, resulting in cycles of elongation and retraction. This dynamic behavior generates significant mechanical forces that distinguish T4P from other types of pili [11].

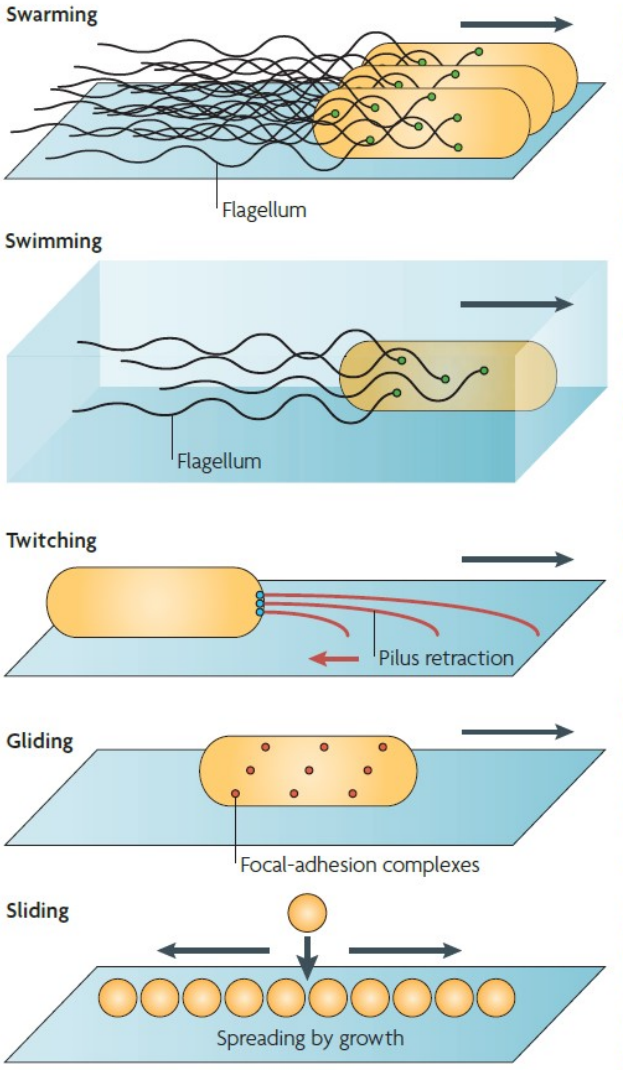

Figure 1.1: Bacteria migrate on surfaces. The motility of bacteria on surfaces by swimming, swarming, gliding, twitching, and sliding. The figure is adapted from [3] by permission from Springer Nature.

In spherical bacteria like *N. gonorrhoeae* and *N. meningitidis*, pili are thought to usually extend uniformly in all directions. In contrast, rod-shaped bacteria, like *Pseudomonas aeruginosa* and *Myxococcus xanthus*, typically display T4P extending from their poles, with a common observation being the presence of pili at only one pole at a time [12].

For *N. gonorrhoeae*, which is the bacterium that is primarility studied here, the T4P are helical polymers consisting mainly of the major subunit PilE. Anchored in a transmembrane complex, T4P are isotropically displayed on the whole cell surface [13],as shown in Fig. 1.3. Their elongation and retraction is driven by the dedicated ATPases PilF and PilT, respectively. PilF is required for pilus polymerization and PilT drives pilus retraction and depolymerization. During retraction, T4P are capable of generating high forces exceeding $100\,\mathrm{pN}$ [6, 14], which is 20 times higher than the force generated by muscle myosin and makes T4P one of the strongest molecular machines known so far [15]. The retraction proceeds with velocities up to $2\,\mu\mathrm{m/s}$ [13, 16]. T4P assemble into bundles that can cooperate to generate forces in the nN range [17]. When individual cells come into proximity of abiotic surfaces such as glass, cells can attach via T4P. Since *N. gonorrhoeae* generates multiple pili simultaneously, a tug-of-war between pili on different sides of the cell body ensues. On glass surfaces, the average detachment force is an order of magnitude smaller than the maximum force generated by pili. Therefore, the tug-of-war leads to a random walk of individual bacteria on surfaces [7, 13, 18–21].

1.1.3 Bacterial colonies

Bacterial colonies consisting of cells with nearly identical geometry and mechancial properties are uniquely suited for studying the non-equilibrium statistical mechanics of living matter [16, 22, 23]. A well-established biological model system is the coccoid/diplococcoid bacterium *N. gonorrhoeae*. With a spherical cell body with a diameter of roughly $1\,\mu\mathrm{m}$, the bacterium forms colonies that are reminiscent of nonliving colloidal assemblies. However, bacteria grow and reproduce. Moreover, while colloidal assemblies are held together by passive attractive interactions, such as depletion forces, *N. gonorrhoeae* colonies are held together by T4P [11]. The fact that the cell-cell interaction is caused by time-dependent non-equilibrium forces affects the shape, dynamics, and sorting behavior of bacterial colonies. *N. gonorrhoeae* mutants without T4P cannot aggregate into colonies [24]. The strength of cell-cell

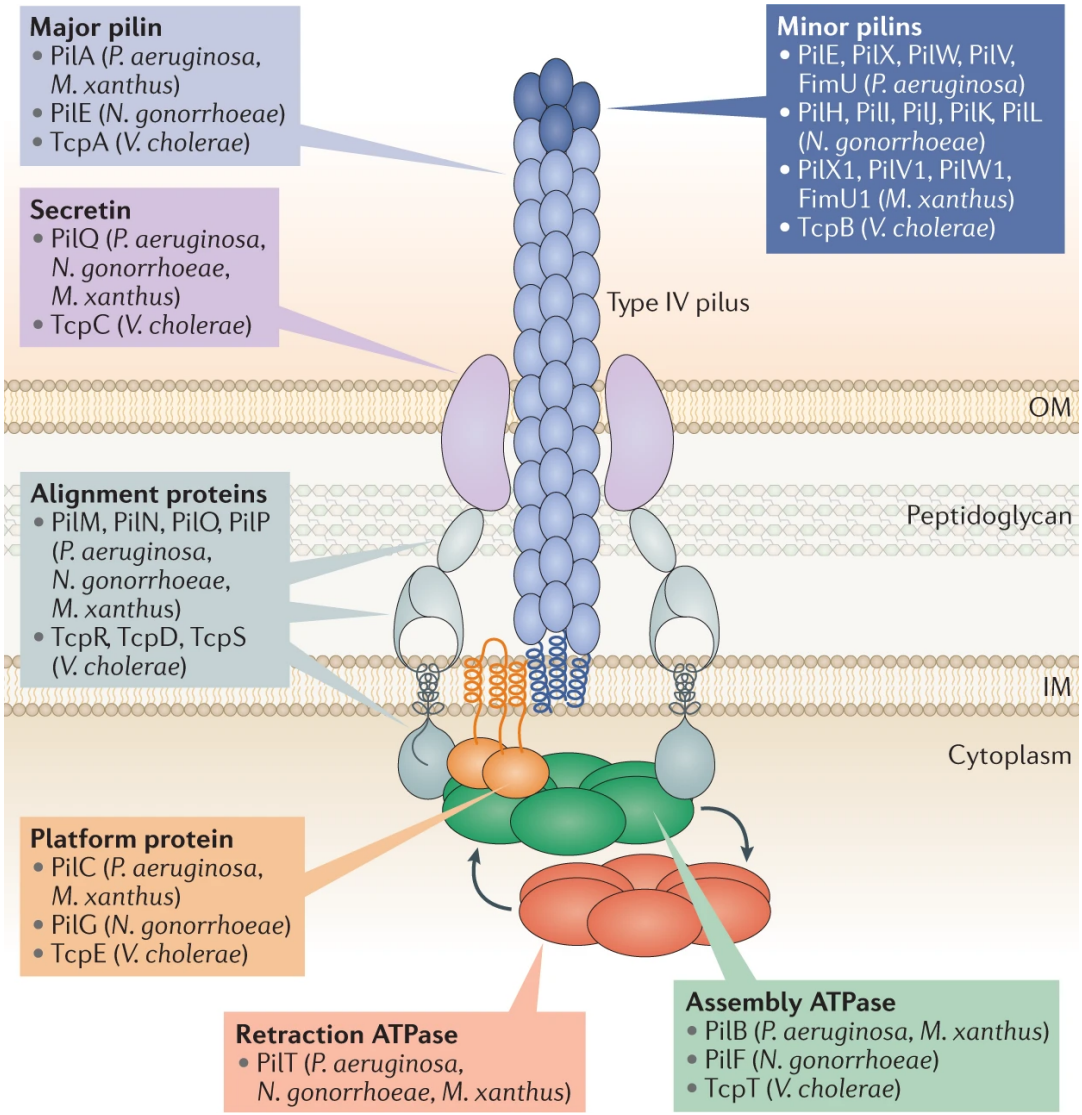

Figure 1.2: T4P structure. The figure is adapted from [11] and reproduced with permission from Springer Nature.

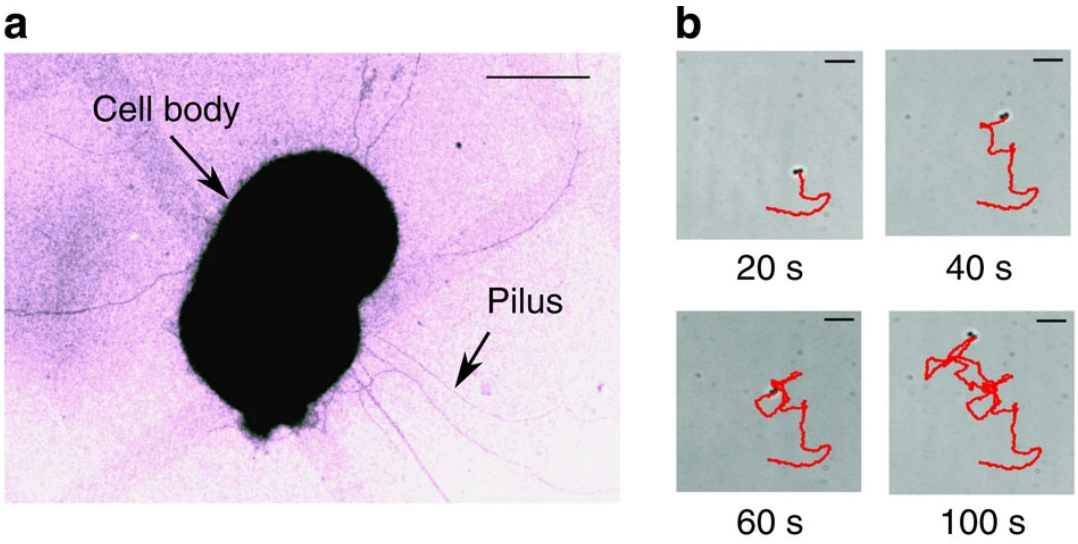

Figure 1.3: (a) A cell body with T4P. (b) A bacterium twitching on a surface. The figure is adapted from [13] by permission from Springer Nature.

attraction is affected by T4P post-translational modifications and can be controlled by inhibiting or activating different steps of the pilin glycosylation pathway [25].

The material properties of *Neisseria* colonies have been characterized as liquid-like [22] with effective viscosities of $\eta \sim 350\,\mathrm{Pa\,s}$ for *N. gonorrhoeae* [16]. Microcolonies display properties that are partially reminiscent of droplets exhibiting an effective surface tension. Evidence for an effective surface tension is firstly the spherical shape of microcolonies formed by *N. gonorrhoeae* with retractile T4P [26]. Secondly, upon contact, two microcolonies fuse to form a sphere with larger radius [16, 24, 27]. Depending on the strength and activity of T4P interactions, initial fusion is however followed by slow coalescence of the two microcolonies that can take hours [20, 28] and the mechanical response of colonies certainly contains elastic components on some time scales.

1.1.4 Swimming

Bacteria endowed with flagella as cellular appendages, such as *Escherichia coli* and *Salmonella typhimurium*, exhibit the capability for active swimming in their surrounding medium. These microorganisms typically feature between five to eight flagella, emerging from the cellular surface, each flagellum being associated with a dedicated motor at its base. The flagellum itself consists of a helical filament, typically adopting a left-handed helical structure with variable length, commonly ranging from 5 to 10 micrometers, with

a diameter of approximately 20 nanometers.

The rotation of flagellar motors in the counterclockwise (CCW) direction induces the propagation of a helical wave, resulting in a propulsive force acting upon the cell. The collective action of the flagellar bundle, responding to CCW motor rotation, leads to a phenomenon commonly referred to as "smooth swimming". This mode of locomotion enables the bacterium to navigate along relatively straight trajectories, achieving speeds of up to 40 micrometers per second. Conversely, when the motors rotate in the clockwise (CW) direction, the flagellar filaments experience a right-handed torsional load, engendering a distinctive behavior known as "tumbling". Consequently, the cell undergoes a process of random reorientation and thereby changes its travel direction.

Within a stable environmental context,the typical movement pattern of bacterial cells exhibits periods of random walk, featuring runs lasting approximately 1 second, which are intermittently interrupted by 0.1-second tumbling events. These movement patterns can be influenced by the chemotaxis signal transduction network. When the bacterium detects changes in its chemical environment, it adjusts its behavior by reducing the frequency of tumbling. This adaptive response introduces a bias into its random movement pattern, promoting preferential movement aligned with the gradient of chemical cues.

It is worth noting that, while flagella are a key determinant of motility in many bacteria, other types of swimming motility exist. For instance, certain microorganisms like *Synechococcus* have evolved the capability for swimming driven by spicules, diverging from the typical reliance on flagella for motility.

1.2 A gentle introduction to Brownian motion

Brownian motion, initially observed by biologist Robert Brown, is characterized by the random motion exhibited by small particles, typically with radii ranging from a few nanometers (10^{-9} m) to micrometers (10^{-6} m), when they are suspended in a fluid with a density not too different from the density of the particles. This phenomenon was also investigated by Albert Einstein, who studied the relationship between random motion, ambient temperature,

and dissipation, which resulted in a formula for the diffusion constant as

$$D = \frac{k_B T}{6\pi\eta R}, \tag{1.1}$$

where k_B is the Boltzmanns constant, T is the temperature, η is the viscosity of the fluid, R is the radius of the Brownian particle. The random motion of these particles arises from the stochastic, high-frequency collisions with the fluid atoms.

In a colloidal system, there are typically three distinctly different timescales. The fast atomic timescale $\tau_a \sim 10^{-12}\,\mathrm{s}$, the relaxation timescale of the particle velocity

$$\tau_r \approx \frac{m}{\gamma} \sim 10^{-3}\,\mathrm{s}, \tag{1.2}$$

where m is the mass of the particle, γ is the friction coefficient, and the characteristic diffusive time scal

$$\tau_d \approx \frac{R^2}{D}. \tag{1.3}$$

Generally,

$$\tau_a \ll \tau_r \ll \tau_d. \tag{1.4}$$

Phenomenologically, the random motion of a particle in one dimension with time-dependent position $x(t)$, velocity $v(t)$ can be described with a Langevin equation

$$\begin{aligned} \frac{\mathrm{d}x(t)}{\mathrm{d}t} &= v(t), \\ m\frac{\mathrm{d}v(t)}{\mathrm{d}t} &= -\gamma v(t) + \xi(t), \end{aligned} \tag{1.5}$$

where $\xi(t)$ is the thermal noise, which satisfies

$$\langle \xi(t) \rangle = 0, \qquad \langle \xi(t_1)\xi(t_2) \rangle = g\delta(t_1 - t_2). \tag{1.6}$$

The Langevin equation (1.5) has an explicit solution

$$v(t) = v(0)e^{-t/\tau_r} + \frac{1}{m}\int_0^t \mathrm{d}s e^{-(t-s)/\tau_r}\xi(s). \tag{1.7}$$

Therefore, the average velocity over all of Brownian particles is given by

$$\langle v(t) \rangle = v(0)e^{-t/\tau_r}. \tag{1.8}$$

The velocity autocorrelation is obtained as

$$\langle v^2(t)\rangle = [\langle v(0)^2\rangle - \frac{g\tau_r}{2m^2}]e^{-2t/\tau_r} + \frac{g\tau_r}{2m^2}. \tag{1.9}$$

In thermal equilibrium, equipartition of energy implies $\langle v^2(t)\rangle = k_BT/m$, which combined with Eq. (1.9) yields an expression that relates noise strength to the temperature and friction

$$g = 2\gamma k_BT. \tag{1.10}$$

Thus, the noise autocorrelations must obey

$$\langle \xi(t_1)\xi(t_2)\rangle = 2\gamma k_BT\delta(t_1 - t_2). \tag{1.11}$$

The displacement of the particle can be solved by making use of the Langevin equation (1.5)

$$x(t) = x(0) + \int_0^t \mathrm{d}s v(0)e^{-s/\tau_r} + \frac{1}{m}\int_0^t \mathrm{d}s \int_0^s \mathrm{d}u e^{-(s-u)/\tau_r}\xi(u). \tag{1.12}$$

The average displacement is

$$\langle x(t)\rangle = x(0) + v(0)\tau_r(1 - e^{-t/\tau_r}). \tag{1.13}$$

The mean squared displacement (MSD) can be calculate as

$$\langle [x(t) - x(0)]^2\rangle = \tau_r^2[1 - e^{-t/\tau_r}]^2[v(0) - \frac{k_BT}{m}] + \frac{2k_BT}{\gamma}[t - \tau_r(1 - e^{-t/\tau_r})]. \tag{1.14}$$

At thermal equilibrium, we have the MSD for short and long time

$$\langle [x(t) - x(0)]^2\rangle = \begin{cases} \frac{k_BT}{m}t^2 & (t \to 0) \\ \frac{2k_BT}{\gamma}t & (t \to \infty) \end{cases}. \tag{1.15}$$

On small timescales, the particle experiences ballistic motion. On large timescales, the particle undergoes diffusive motion and the MSD can be written as

$$\langle [x(t) - x(0)]^2\rangle = 2Dt, \tag{1.16}$$

where the Stokes-Einstein relation follows from comparison with Eq. (1.15) as

$$D = \frac{k_B T}{\gamma} = \frac{k_B T}{6\pi\eta R}. \tag{1.17}$$

1.3 Introduction to particle-based simulation methods

1.3.1 Overview

At the macroscopic scale, fluid motion can be described in a hydrodynamic framework where conservation of momentum yields the Navier-Stokes Equations (NSEs). However, systems consisting only of few particles in a bath or systems consisting of subunits that actively generate mechanical forces on small lengthscales cannot always be described by the language of hydrodynamics. Indeed, computers can meticulously simulate experimental systems, serving as invaluable tools for the theoretical analysis of experimental results. Various simulation methods have been developed over the past few decades to computationally model biological systems at the microscopic and mesoscopic scale.

At the microscopic scale, motion of complex fluids can be simulated by capturing the movement of individual solute and solvent molecules, this approach is known as Molecular Dynamics (MD) simulation. MD simulation is a computational technique used to determine the positions and velocities of individual solvent particles by applying Newton's law. It can capture both thermal fluctuations and hydrodynamics, providing valuable insight into microscopic systems. However, MD simulations are limited by their computational expense and are typically applicable to small length and time scales. Therefore, a method that connects macroscopic and microscopic scales in simulations is needed, and it is generally referred to as mesoscopic scale simulation [29, 30].

The mesoscale is typically characterized by spatial dimensions ranging from $10 - 10^4$ nm and temporal dimensions ranging from $1 - 10^6$ ns [31]. Simulating systems at this scale using MD method is quite costly due to the substantial number of atoms and timesteps required. To study mesoscopic systems, which involve larger length and time scales, coarse-grained or mesoscopic simulation methods have been developed. These methods provide a computationally efficient approach for investigating mesoscopic systems while

retaining essential system properties. Thus, they serve as a bridge connecting the realms of microscopic and macroscopic scales in the field of molecular modeling and simulation.

In Brownian Dynamics (BD) simulations, particle motion is described by an overdamped Langevin equation. In particular, the original BD method does not account for hydrodynamic interactions. To account for hydrodynamic interactions, an enhancement can be achieved by introducing the Oseen tensor, thereby refining the simulation's ability to capture the influence of fluid dynamics on particle dynamics.

The Lattice-Boltzmann (LB) method is a computational approach used to simulate fluid flow [32–35]. Unlike solving the Navier-Stokes Equations (NSE), the LB method involves a lattice-based solution of the Boltzmann equation. This technique ensures the conservation of both mass and momentum, providing an effective means of modeling fluid behavior in a computationally efficient manner.

Another popular simulation technique is Multi-Particle Collision (MPC) dynamics, which successfully integrates both thermal fluctuations and hydrodynamics [36–42]. However, it is important to note that the MPC fluid is modeled asa gass-like collection of particles and thus possesses high compressibility. Therefore, compressibility issues may represent challenges when attempting to accurately model certain physical systems, such as binary mixtures.

1.3.2 Dissipative particle dynamics

The Dissipative Particle Dynamics (DPD) method differs from conventional molecular simulations by representing a small fluid cluster as one particle rather than as individual molecules [43–47]. The number of molecules N_m in this cluster is referred to as the coarse-graining parameter, it has been demonstrated that DPD is approximately $1000\, N_m^{8/3}$ times faster compared to MD method [48]. Another advantage of DPD over MD is that the hard-core Lennard-Jones (LJ) potential between molecules can be replaced by a soft-core potential between DPD particles that represents the coarse-grained interaction among many molecules. Such a soft potential allows the use of larger time steps in DPD simulations [49].

In Dissipative Particle Dynamics (DPD), pairwise interactions guarantee momentum conservation, contrasting with original Brownian dynamics. This distinction gives rise to proper hydrodynamics at larger scales [50–53].

The standard DPD method has some inherent limitations. Therefore, to simulate more complex systems, some improved DPD methods have been proposed. The dissipative and random forces in DPD are chosen to obey the fluctuation-dissipation theorem and function as a thermostat. As a result, the standard DPD method is not energy conserving and is particularly suited for modeling isothermal systems. To overcome the energy conservation limitation in standard DPD, a modified version known as Energy-conserving Dissipative Particle Dynamics (EDPD) has been developed [44, 54, 55].

In the original DPD method, the soft interaction potential imposed limitations on the Equation Of State (EOS) for the simulated system [56, 57]. Therefore, the Many-body DPD (MDPD) method has been proposed, where the interaction potential between particles is derived from many-body potentials [58–67]. Such many-body potentials are analogous to the potentials between atoms in MD simulations. For coexistence of multiple components, the interaction potential in MDPD depends on the local density. This approach has the potential to produce an equation of state that is more widely applicable than the original DPD. A classic example is liquid-vapor coexistence, where the MDPD can achieve a van der Waals loop in the EOS [57].

Furthermore, the Smoothed DPD (SDPD) method combines DPD and Smoothed Particle Hydrodynamics (SPH) to provide an improved approach to simulating complex fluid systems. SDPD integrates the advantages of other improved DPD methods and overcomes some limitations present in the standard DPD method. Energy conservation is maintained in SDPD method, consistent with the principles of EDPD method. SDPD has a wide range of applicability and has been used to simulate various complex fluid systems [68–81].

DPD and its improved versions have been widely used to simulate various complex systems [31]. Numerous studies have focused on simulating colloidal suspensions using DPD, with utilizing different approachs to represent the solute [82]. One approach is to assemble a colloidal particle composed of DPD particles that move rigidly or are connected by springs [51, 83–85]. This strategy simplifies the representation of arbitrary shapes and allows the inclusion of confinement effects resulting from walls [86, 87]. An

alternative approach, in which a single DPD particle represents each colloidal particle [88–91], is less computationally costly. The colloidal system of blood has been studied with original DPD and SDPD [72, 73, 92–95].

Liquid droplets have been simulated as an example of gas-liquid phase separation [96]. The wetting behavior of droplets on solid surfaces has been simulated by DPD [97]. Additionally, MDPD has been employed in extensive simulations to further investigate the properties and dynamics of droplets [57, 98]. The simulation of biological membranes and their complex mechanisms has been achieved using DPD [48, 99–103]. DPD has been used extensively to simulate polymers with and without entanglements [104–112].

To reduce computational costs, methods for solvent-free DPD simulations have been proposed [100, 113]. This approach assumes that solutes are always in equilibrium, allowing for the implicit treatment of solvent particles. However, to achieve results comparable to explicit solvent simulations, adjustments to the interaction potentials between solutes are required. By significantly reducing the number of simulated particles, implicit solvent DPD offers advantages over explicit solvent DPD, including faster simulation speeds and smaller memory and storage requirements. Additionally, the simulation results of the two methods are consistent [100]. Methods similar to implicit solvent DPD have been used extensively in simulations, including simulations of bacterial colonies [114] , tissues [115, 116], and self-propelled particle systems [117].

1.3.3 Time integration algorithms for dissipative particle dynamics

In early implementations of DPD, the Euler algorithm was utilized to update the velocities and positions of particles by integrating the DPD equations [50, 52]. For a particle with the index i, the position $\mathbf{r}_i$, velocity $\mathbf{v}_i$, and force $\mathbf{f}_i$ of the particle, over a small time step Δt, are given by

$$\begin{aligned} \mathbf{r}_i(t+\Delta t) &= \mathbf{r}_i(t) + \Delta t\, \mathbf{v}_i(t), \\ \mathbf{v}_i(t+\Delta t) &= \mathbf{v}_i(t) + \Delta t\, \mathbf{f}_i(t), \\ \mathbf{f}_i(t+\Delta t) &= \mathbf{f}_i(\mathbf{r}_i(t+\Delta t), \mathbf{v}_i(t+\Delta t)). \end{aligned} \tag{1.18}$$

As a more efficient scheme, a modified velocity-Verlet algorithm has been proposed in Ref. [118]:

$$\begin{aligned}
\mathbf{r}_i(t+\Delta t) &= \mathbf{r}_i(t) + \Delta t\, \mathbf{v}_i(t) + \frac{1}{2}(\Delta t)^2 \mathbf{f}_i(t), \\
\widetilde{\mathbf{v}}_i(t+\Delta t) &= \mathbf{v}_i(t) + \lambda \Delta t\, \mathbf{f}_i(t), \\
\mathbf{f}_i(t+\Delta t) &= \mathbf{f}_i(\mathbf{r}_i(t+\Delta t), \widetilde{\mathbf{v}}_i(t+\Delta t)), \\
\mathbf{v}_i(t+\Delta t) &= \mathbf{v}_i(t) + \frac{1}{2}\Delta t\, (\mathbf{f}_i(t) + \mathbf{f}_i(t+\Delta t)).
\end{aligned} \tag{1.19}$$

Here, the factor λ is a constant whose value is $1/2$ in the original Verlet algorithm but may also be chosen differently.

A number of alternative time integration algorithms for DPD simulations have been suggested over the years [81, 119–128].

1.4 Objectives of this thesis

Internally driven many-particle systems exhibit a rich behavior, including various types of non-equilibrium phase transitions, pattern formation, and so-called giant fluctuations. Many of these phenomena were studied with particles that, in addition to being active, have some internal orientation, either in their geometry or through a directed active motion. Coccoid bacteria with an active force that is on average isotropic are an arguably simpler form of active matter which is known to exhibit certain non-equilibrium features, such as demixing of active and passive bacteria. While some of these behaviors have already been studied theoretically and experimentally, a plethora of non-equilibrium behaviors that could also be biologically relevant remain to be studied. In this thesis, focusing on *N. gonorrhoeae* as a model system, we have constructed a simulation model for bacterial colonies, incorporating a force analogous to the force generated by T4P. The model is designed for the simulation of colony growth and formation, enabling the study of colony behavior both in solution and on solid surfaces. Comparative analysis of simulation results with experimental data can offer valuable insights into the non-equilibrium physics that governs the behavior of these colonies.

In Chapter 2, we introduce the effective model that is employed in our study. The interactions between bacteria are represented by DPD. A DPD particle represents a single bacterium and the volume repulsion, dissipation and thermal fluctuations of the bacteria are included. By adding an additional force

to represent the interaction between T4P, the binding, retraction and rupture of pili are also taken into account. Bacterial growth is modeled by a pair of bound particles, with the rest length between them slowly increasing until a cell division threshold is reached, at which point they divide into two daughter cells. The selection of appropriate parameter values is informed by a comparative analysis with existing experimental data.

The material properties of *N. gonorrhoeae* colonies have been characterized as liquid-like [22] with effective viscosities [16]. The motor activity of T4P accelerates the processes of local ordering and shape relaxation during colony fusion have been shown. How the molecular properties of motor proteins affect colony dynamics is difficult to quantify experimentally, but is possible for simulations. We investigate the effect of pili properties, such as binding rate, retraction velocity and number of pili, on the RDF and MSD of the colonies in Chapter 3. The results of our simulations and experiments are comparable.

In thermodynamic equilibrium, the velocity correlation measured in particle systems is generally proportional to the linear response with respect to a small perturbation, which is called a fluctuation-response relation [129]. The extent of the violation of this fluctuation-response relation in non-equilibrium states can be related to the rate of energy dissipation [130, 131]. For bacterial colonies, active force-generation by T4P changes the fluctuations of the conservative forces experienced by the cells and entails energy dissipation. Therefore, the fluctuation-response relation is expected to be violated in bacterial colonies under the premise that colonies can be described as physical particle system [132–134]. In Chapter 3 we devise a model for quantifiying the power spectral density of active bacterial colonies and compare the results with experimental data. Then, by simulating an experimental setup for probing the colony response to an external force, we investigated violation of the equilibrium fluctuation-response relation in bacterial colonies.

Unlike passive liquids whose spreading behavior has been extensively studied, little is known about the spreading behavior of active bacterial colonies. Do such active matter systems exhibit similar spreading behavior on surfaces as passive liquids? Through the integration of experimental observations, computational simulations, and theoretical analyses, we investigate the spreading behavior of colonies on solid surfaces in Chapter 4.

Experiments have shown that bacteria within colonies decrease pili activity

in response to oxygen and nutrient depletion. Such colonies undergo sorting, which is sometimes accompanied by the colony folding. What factors determine the occurrence of folding in bacterial colonies? In Chapter 5, we investigate the folding of bacterial colonies by implementing an appropriate simulation model.

Chapter 2

Computational model for simulation of bacterial colonies

2.1 Assumptions and model description

In our simulations, colonies are grown from individual cells through cell division. An individual cell is also called a coccus. A pair of dividing *N. gonorrhoeae* cells is called a diplococcus and has the shape of two partially overlapping spheres. During the growth, each diplococcus divides approximately with rate α into a pair of individual cocci, which in turn again become diplococci after some time. The fraction of dead cells in *N. gonorrhoeae* colonies is reported to be below $5\,\%$ [135] and cell death is therefore neglected in our model. Each individual coccus is endowed with a repulsive potential modeling volume exclusion. In addition, cells experience dissipative forces resulting from relative motion of neighboring cells and thermal fluctuations. Each cell has a fixed number of pili. By modeling the pili as dynamic springs that can extend, retract, bind and unbind either with other pili or with the environment, we faithfully represent the stochatic nature of cell-generated forces.

2.1.1 Cell geometry and bacterial growth

All simulations are conducted in a three-dimensional, Cartesian coordinate system. Individual cells are modeled as soft spheres with radius R. The position of the center of bacterium i is denoted by $\mathbf{r}_i$. The vector between a pair of bacteria with indices (i, j) is denoted by $\mathbf{r}_{ij} = \mathbf{r}_i - \mathbf{r}_j$ and their distance is $r_{ij} = |\mathbf{r}_{ij}|$.

The division of a cell with index i is modeled by insertion of a second sphere with index j on top of i so that the excluded volume remains the same during insertion. The pair of cells is initially connected by an elastic spring with time-dependent rest length $l(t)$, thus forming a diplococcus. The initial orientation of the vector connecting the cell pair is chosen randomly. Then, growth of the diplococcus is simulated by increasing the rest length of the spring that connects the cell pair as

$$\frac{\mathrm{d}l(t)}{\mathrm{d}t} = \frac{\alpha}{\nu_\mathrm{r}}, \tag{2.1}$$

with a rate constant α and a constant with units of length $1/\nu_\mathrm{r}$. This linear growth of the long axis of the diplococcus with time is consistent with experimental data presented in Ref. [136]. Note that the geometry of the growth of the diplococcus implies that the volume growth rate increases with size of the individual diploccus. As a generalization, one could also include a growth rate α that explicitly depends on the size of the diplococcus to represent an arbitrary volume-dependency of the growth on the single-cell level [137]. A further complication that has not been included in the model, for simplicity, is that the direction of growth and division in *Neisseria* likely follows a complex pattern determined by alternating perpendicular division planes [136]. Once the length $l(t)$ reaches a threshold l_t, the connecting spring is removed and the two spheres are treated as individual cocci. Instantaneous forces acting on either of the two cocci during their separation are equally distributed among the two cocci to ensure momentum conservation. The time between creation of a diplococcus and separation of the two daughter cells is given by $t_\mathrm{r} = l_\mathrm{t}\nu_\mathrm{r}/\alpha$.

After separation of a diplococcus, the two individual cocci do not become diplococci instantaneously. Rather, individual cells are turned into diplococci at a constant rate per cell, for which we employ for simplicity the same rate constant α that also appears in Eq. (2.1). This means that the separation of a diplococcus (division) is followed by a random refractory time, which prevents an unphysical synchronization of the division events in the simulations.

The growth and division model employed in this work is primarily motivated by its simplicity and numerical stability. For several bacterial organisms, experimental studies have demonstrated that homeostasis of cell size can be explained by a phenomenological “adder rule”, whereby cells

increase by a constant volume each generation, regardless of initial size at division [138–140]. Thereby, the volume increment during each generation sets the division time and division times obey a Gaussian distribution. For our model, however, we choose to keep the sizes of the spheres always the same to enable a robust parametrization. This choice produces a natural scale for cell division and insofar determines the division times. The additive noise in bacterial division times that reportedly results in their Gaussian distribution [139] is represented in our model approximately by the random refractory time between pair separation and creation of daughter cells in the next generation.

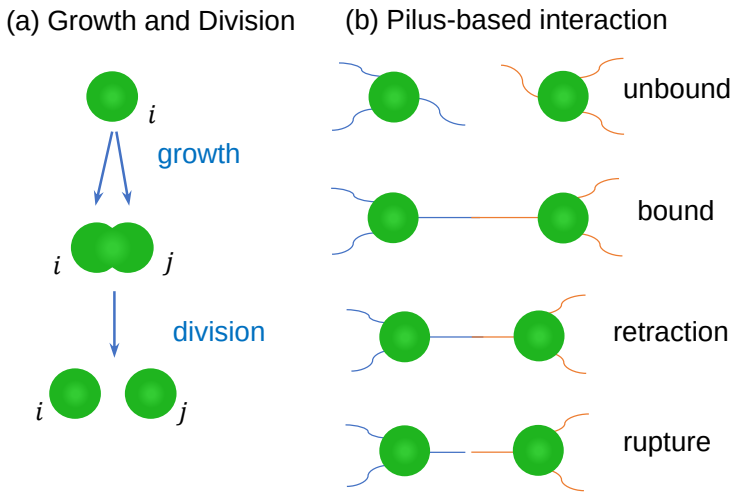

Figure 2.1: Schematic representation of the two active processes occurring in the simulations: (a) A bacterium grows into a diplococcus and then divides into two individual bacteria. (b) Two cells bind to each other via pili. Subsequently, pili are retracted by the bacteria leading to a force build-up. The bond connecting the pili ruptures stochastically in a force-dependent manner.

2.1.2 Dynamics of type IV pili

Each cell is assumed to have a constant number of pili, typically around 7, see Tab. 2.1. A pilus of bacterium i is assumed to bind with a rate k_{bind} to one pilus of a neighboring bacterium j. For binding, the distance between i and j, r_{ij}, is required to be less than a cutoff distance d_{bind}. This cutoff distance ensures that only bacteria bind to each other when they are in proximity to each other. In some simulations, a distance-based criterion and a Voronoi tessellation are combined to limit pilus interactions only to immediate neighbors that have a distance from each other that is smaller than the cutoff for pilus binding. For simplicity, we assume that pilus-based forces act along the

straight lines connecting the centers of cell pairs. It is assumed that two bacteria can only have one pair of pili adhering to each other. Likewise, bundling of pili [13] is also neglected due to its unknown role in cell colonies. Pili of the two cells in a diplococcus do not bind to each other. The pilus-based cell-cell connection is modeled as a spring connecting the centers of two cells. The rest length of the pilus connecting two cells with indices i and j is denoted by L_{ij}. The force exerted on the pair of cells is purely attractive and given by

$$f_{ij}^{p} = \min\left[0, -k[r_{ij}(t) - L_{ij}(t)]\right], \tag{2.2}$$

where k is the pilus' spring constant. Once the pilus is bound, it is assumed to retract. Thus, the effective pilus dynamics employed for our model exclude non-retracting pili that form passive bonds among cells, see, e.g. Ref. [19]. Pilus retraction leads to a continuous shortening of its rest length as

$$L_{ij}(t) = \max\left[2R, r_{ij}(0) - \int_0^t v_{\mathrm{re}}(t)\mathrm{d}t\right], \tag{2.3}$$

where v_{re} is the force-dependent retraction velocity of pili. To describe the force-velocity relationship for T4P retraction motors [14], we employ the linearized relation

$$v_{\mathrm{re}}(t) = \max\left[0, v_{\mathrm{re}}(0)\left(1 - \frac{f_{ij}^{p}}{f_{\mathrm{s}}}\right)\right], \tag{2.4}$$

where the stall force f_{s} represents the maximal force a retracting pilus can generate. Furthermore, it is assumed that the bonds between the pili rupture under stress with a force-dependent rate as

$$\gamma_{\mathrm{rupt}} = \frac{1}{t_1 e^{-f_{ij}^{p}/F_{\mathrm{c},1}} + t_2 e^{-f_{ij}^{p}/F_{\mathrm{c},2}}}, \tag{2.5}$$

where t_1 and t_2 are two characteristic rupture time, $F_{\mathrm{c},1}$ and $F_{\mathrm{c},2}$ are two characteristic rupture force. To simplify the analysis the effect of characteristic rupture time on colony dynamics in Secs. 3.4, 3.5, 3.6, we employ a simplified pilus-pilus rupture rate formula in these sections as

$$\gamma_{\mathrm{rupt}} = k_{\mathrm{rupt}} e^{f_{ij}^{p}/F_{\mathrm{rupt}}}, \tag{2.6}$$

where k_{rupt} is the pilus rupture rate without loading and F_{rupt} is a characteristic rupture force. See, e.g., Refs. [13, 19, 20, 141] for related models of pilus dynamics.

2.1.3 Dynamics of bacteria

For simulating the cell dynamics, we employ an algorithm similar to dissipative particle dynamics (DPD) [118, 142], where we assume a soft repulsion between cells, a frictional force proportional to the relative velocity of neighboring cells, and thermal noise forces that satisfy the Einstein relation. Underdamped equations of motion for every cell i with mass m_i, position $\mathbf{r}_i$, velocity $\mathbf{v}_i$, and force $\mathbf{f}_i$ are assumed as

$$\frac{\mathrm{d}\mathbf{r}_i}{\mathrm{d}t} = \mathbf{v}_i, \qquad m_i \frac{\mathrm{d}\mathbf{v}_i}{\mathrm{d}t} = \mathbf{f}_i. \tag{2.7}$$

The force acting on each pair of cells consists of conservative forces $\mathbf{F}^c_{ij}$, dissipative forces $\mathbf{F}^d_{ij}$, thermal fluctuations $\mathbf{F}^r_{ij}$ and forces from active pilus retraction $\mathbf{F}^p_{ij}$. Overall, the sum of these forces is

$$\mathbf{f}_i = \sum_{j \neq i} (\mathbf{F}^c_{ij} + \mathbf{F}^d_{ij} + \mathbf{F}^r_{ij} + \mathbf{F}^p_{ij}). \tag{2.8}$$

For defining the individual force terms, we employ the vector between the centers of masses $\mathbf{r}_{ij} = \mathbf{r}_i - \mathbf{r}_j$ and the unit vector pointing towards cell i denoted by $\widehat{\mathbf{r}}_{ij} = \mathbf{r}_{ij}/r_{ij}$.

The conservative force acting between pairs of unbound bacteria is

$$\mathbf{F}^c_{ij} = \begin{cases} a_0(1 - r_{ij}/d_{\mathrm{con}})\widehat{\mathbf{r}}_{ij} & (r_{ij} < d_{\mathrm{con}}) \\ 0 & (r_{ij} \geq d_{\mathrm{con}}) \end{cases}, \tag{2.9}$$

where a_0 is the maximum conservative force between bacterium i and j, the cutoff distance for the repulsive cell-cell interaction is denoted by $d_{\mathrm{con}} = 2R$. For a diploccus consisting of two spheres, the conservative force due to growth is

$$\mathbf{F}^c_{ij} = a_{\mathrm{growth}}(l_i - r_{ij})\widehat{\mathbf{r}}_{ij}, \tag{2.10}$$

where a_{growth} is the elastic constant of the spring connecting the two cells of a diplococcus. The dissipative and random forces are, respectively, given by

$$\mathbf{F}^d_{ij} = -\gamma \omega^D(r_{ij})(\widehat{\mathbf{r}}_{ij} \cdot \mathbf{v}_{ij})\widehat{\mathbf{r}}_{ij}, \tag{2.11}$$

$$\mathbf{F}^r_{ij} = \sqrt{2\gamma k_{\mathrm{B}} T}\, \omega^R(r_{ij})\theta_{ij}\widehat{\mathbf{r}}_{ij}, \tag{2.12}$$

where γ is a friction coefficient, ω^D and ω^R are distance-dependent weight functions, k_{B} is the Boltzmann constant, T is the ambient temperature and

$\theta_{ij} = \theta_{ji}$ is a random number drawn from a Gaussian distribution with zero mean and unit variance. For the distance-dependence of the friction force we choose

$$\omega^D(r) = [\omega^R(r)]^2 = \begin{cases} (1 - r_{ij}/d_{\mathrm{dpd}})^2 & (r_{ij} < d_{\mathrm{dpd}}) \\ 0 & (r_{ij} \geq d_{\mathrm{dpd}}) \end{cases}, \tag{2.13}$$

where d_{dpd} is the cutoff distance for dissipative and random forces. Finally, the forces resulting from retraction of pili are given in their vectorial form by

$$\mathbf{F}^p_{ij} = f^p_{ij}\widehat{\mathbf{r}}_{ij}. \tag{2.14}$$

Note that we do not consider the torques generated by T4P between pairs of cells, see Ref. [20] for such a model.

2.2 Computational methods

2.2.1 Simulation details and parameter values

The simulation code is integrated into the molecular dynamics simulator LAMMPS [143], which allows an efficient parallelization while providing great flexibility regarding the model choice. To model the cellular dynamics described above, we wrote a new C++ code. The velocity-Verlet algorithm is used to advance the set of positions, velocities and forces. The code is parallelized for execution on CPUs and large colonies consisting of ten-thousands of bacteria can be simulated efficiently. The colonies are visualized with OVITO [144].

The characteristic scales that are used as simulation units are the cell diameter $d_{\mathrm{c}} = 2R = 1\,\mu\mathrm{m}$, a time scale given by the inverse of the default value of the pilus-unbinding rate constant $t_{\mathrm{c}} = 1/k_{\mathrm{rupt}} = 1\mathrm{s}$, and a force scale of $f_{\mathrm{c}} = 1\,\mathrm{pN}$. Parameters values that are used for the simulations are listed in Tab. 2.1. Whenever alternative parameter values are used, they are provided with the results.

2.2.2 Separation of time scales

In the simulations, the time scale of viscous relaxation is smaller than the time-scale of pilus-based interaction. Thus, inertial effects are negligible. Moreover, the time scale of the pilus-based interaction is much smaller than the time-scale of cell division $t_{\mathrm{c}} \ll 1/\alpha$. Simulations typically start with one

Table 2.1: The choice of parameters for the simulations.

Parameter	Value	Unit	Reference
cell radius R	0.5	d_c	[16]
cell mass m	0.1	$f_\mathrm{c} t_\mathrm{c}^2 d_\mathrm{c}^{-1}$	
pilus spring constant k	500	$f_\mathrm{c} d_\mathrm{c}^{-1}$	
pilus stall force f_s	180	f_c	
maximum retraction velocity of pili v_0	2	$d_\mathrm{c} t_\mathrm{c}^{-1}$	
number of pili per cell	7		[18]
simulation time step Δt	1×10^{-4}	t_c	
division rate α	1/500	t_c^{-1}	
diplococcus growth parameter ν_r	1.0	d_c^{-1}	
pilus characteristic rupture time t_1	0.5	t_c	
pilus characteristic rupture time t_2	0.091	t_c	
pilus characteristic rupture force $F_{\mathrm{c},1}$	4.5	f_c	
pilus characteristic rupture force $F_{\mathrm{c},2}$	60	f_c	
pilus rupture rate k_rupt	3	t_c^{-1}	
pilus binding cutoff distance d_bind	2.5	d_c	
pilus binding rate k_bind	10	t_c^{-1}	
pilus-pilus bond rupture force scale F_rupt	22.5	f_c	[16, 145]
maximum conservative force a_0	4000	$f_\mathrm{c} d_\mathrm{c}^{-1}$	
conservative force cutoff $d_\mathrm{con} = 2R$	1.0	d_c	
diplococcus spring constant a_growth	4000	$f_\mathrm{c} d_\mathrm{c}^{-1}$	
friction coefficient γ	50	$f_\mathrm{c} t_\mathrm{c} d_\mathrm{c}^{-1}$	
thermal energy scale $k_\mathrm{B}T$	1×10^{-5}	$f_\mathrm{c} d_\mathrm{c}$	
dissipative and random force cutoff d_dpd	1.5	d_c	

bacterium and colonies are formed by letting the cells grow and divide. The colony structures emerge during growth due to the repulsive interactions, thermal noise, and pilus-based interactions, as shown in Fig. 3.1(a). In some simulations, it is desirable to completely remove the effect of cell growth on the bacterial dynamics. For this purpose, cell growth and division are switched off after a sufficient colony size is reached.

2.3 Experimental data

Experiments were carried out in the laboratory of Prof. Dr. Berenike Maier at University of cologne. Bacterial colonies were grown as described previously [25, 146]. The presented data, with the exception of the data for Fig. 5c, was originally generated for work summarized in Refs. [25, 147, 148]. Briefly, for assessing colony structure and dynamics, bacteria were incubated within a flow chamber under continuous nutrient supply for one hour to several hours hours. Constant supply of nutrients and, if used, antibiotics was ensured by applying continuous flow. For calculation of the RDF, bacteria were stained with Syto 9 to enable detection of the position of individual cells and to determine the cell volume. Colony dynamics were assessed with gfp and mcherry expressing cells [25]. In detail, the origin of the data is as follows. The confocal section of a microcolony of fluorescently labeled bacteria in Fig. 3.1b) was produced as described in [148]. The rupture forces of T4P bonds shown in Fig. 3.2a) were measured with an optical trap and experimental methods are described in Ref. [25]. Diffusion coefficients and RDFs were shown in Figs. 3.2c),f) were measured as described in [147]. The PSDs of the colony boundary fluctuations shown in Fig. 3.4(c) were calculated from time-lapse images of colonies recorded at 10 Hz for one minute. The corresponding experimental methods are detailed in Refs. [16, 25].

Chapter 3

Growth, active fluctuations, segregation, adhesion and invasion of bacterial colonies

This chapter is published in Communications Physics with the title "Non-equilibrium dynamics of bacterial coloniesgrowth, active fluctuations, segregation, adhesion, and invasion" in 2022 [114].

3.1 Introduction

While material properties of *N. gonorrhoeae* colonies have been characterized [22], many non-equilibrium effects resulting from active bacterial force-generation remain to be explored. In thermodynamic equilibrium, the velocity correlation measured in particle systems is generally proportional to the linear response with respect to a small perturbation, which is called a fluctuation-response relation [129]. The extent of the violation of this fluctuation-response relation in non-equilibrium states can be related to the rate of energy dissipation [130, 131]. For bacterial colonies, active force-generation by T4P changes the fluctuations of the conservative forces experienced by the cells and entails energy dissipation. Therefore, the fluctuation-response relation is expected to be violated in bacterial colonies under the premise that colonies can be described as physical particle system [132–134]. However, the frequency-characteristics and measurability of this violation are unknown. Thus, an aim of this work is to establish theoretical predictions regarding the non-equilibrium fluctuations of *N. gonorrhoeae* colonies.

Internally driven many-particle systems can also exhibit non-equilibrium phase transitions, which has been investigated for some classes of model systems,

see, e.g., Refs. [149–152]. Notably, for active particles that undergo rotational motion and thus on average obey rotational symmetry, density fluctuations are Gaussian and the non-equilibrium phase transitions can be understood in a framework similar to equilibrium phase transitions [153, 154]. For *N. gonorrhoeae* colonies, the average force generation by individual bacteria is presumably almost spherosymmetric and therefore it may be challenging to distinguish genuine non-equilibrium colony dynamics from dynamics that are also be observable in passive systems. However, it has been shown experimentally that mechanical forces govern the sorting of different cells during the early formation of *N. gonorrhoeae* colonies [145]. Mutants with different T4P density and rupture forces of T4P-mediated adhesion spatially segregate inside colonies, suggesting a sorting process driven by pilus retraction that also depends on differential adhesiveness [28, 145]. Self-sorting of *Neisseriae* colonies has been studied experimentally by changing the post-translational modification of T4P, their activity, and computer simulations have been conducted [22, 28, 145].

In general, physical properties of large bacterial colonies are ideally studied with a combination of experiments, theory, and detailed computer simulations. Previous work includes simulations of the dynamics of single cells due to individual pili [13, 19–21] and coarse-grained approaches or continuum theories for the description of *Neisseria* colonies [155]. Furthermore, multiscale simulations combining overdamped cell dynamics with stochastic pilus activity have shown great promise for the investigation of the behavior of *Neisseria* colonies on different length scales [20, 22]. Mechanical forces in bacterial colonies are not only actively generated by T4P but also by cell growth and division. For the case of mammalian cells, tissue growth has been studied extensively with particle-based simulations where individual cells are represented as spheres [115, 156, 157]. The sphericity and growth dynamics assumed for cells with these models are also appropriate for simulating coccoid bacteria.

3.2 Exponential colony growth

Figures 3.1 shows simulation results for colony growth. As for experimental systems, colonies approximately maintain a spherical shape during growth. In the simulations, both the number of bacteria and the colony radius increase exponentially with time. Colony radii are quantified by measuring

the distance between the center of mass and cells on the boundary at a fixed polar angle and azimuth. Since we have not taken into account a position-dependence of nutrient availability inside colonies, we expect to see such growth dynamics in experiments only for small cell colonies in rich media. Experimentally, an exponential increase of the radii of *N. gonorrhoeae* colonies has been observed for about three hours during the initial growth of young colonies [135].

Next, analytical formulas are derived for the simulated growth dynamics. The cell-growth simulations are based on the assumption of two growth phases - consisting of single cocci and diplococci. The advantage of this two-phase model is that it allows the introduction of a controllable randomization of division events and thus the avoidance of artificial division synchronization. A single coccus can divide to form a diplococcus, which is a random event that occurs with rate α. The resulting diplococcus cannot divide immediately but grows on average for a time t_r until it separates into two single cocci that can then divide. We denote the average number of all cells forming the cocci and diplococci by $N(t)$. The average number of cells that are single cocci is denoted by $N_\mathrm{c}(t)$. Since only the single cocci are assumed to divide, the overall number of bacteria is determined by

$$\frac{\mathrm{d}N(t)}{\mathrm{d}t} = N_\mathrm{c}(t)\alpha. \tag{3.1}$$

We next consider the governing equation for the number of single cocci $N_\mathrm{c}(t)$, which increases at time t through separation of diplococci. The separating diplococci, in turn, were formed at time $t-t_\mathrm{r}$ through division of single cocci. Hence, the increase of single cocci at time t is given by $2\alpha N_\mathrm{c}(t-t_\mathrm{r})$, where the factor 2 results from cell doubling during division. Simultaneously, the number of single cocci is reduced through formation of diplococci with rate $\alpha N_\mathrm{c}(t)$. Overall, we obtain

$$\frac{\mathrm{d}N_\mathrm{c}(t)}{\mathrm{d}t} = 2\alpha N_\mathrm{c}(t-t_\mathrm{r}) - \alpha N_\mathrm{c}(t). \tag{3.2}$$

Growth is assumed to obey an exponential time dependence and the ansatz $N_\mathrm{c}(t) = N_\mathrm{c}(0)e^{\alpha p t}$ with a constant p is inserted into Eq. (3.2). This yields a nonlinear equation determining p as

$$p = 2e^{-p\alpha t_\mathrm{r}} - 1. \tag{3.3}$$

Insertion of this result into Eq. (3.1) yields the final result for the overall cell number as

$$N(t) = N_c(0)e^{\alpha p t}/p. \tag{3.4}$$

Thus, the effective growth rate of the cell number in simulations is given by αp. Formula (3.4) has no free parameters and fits the simulation results very well, see the inset of Fig. 3.1(c).

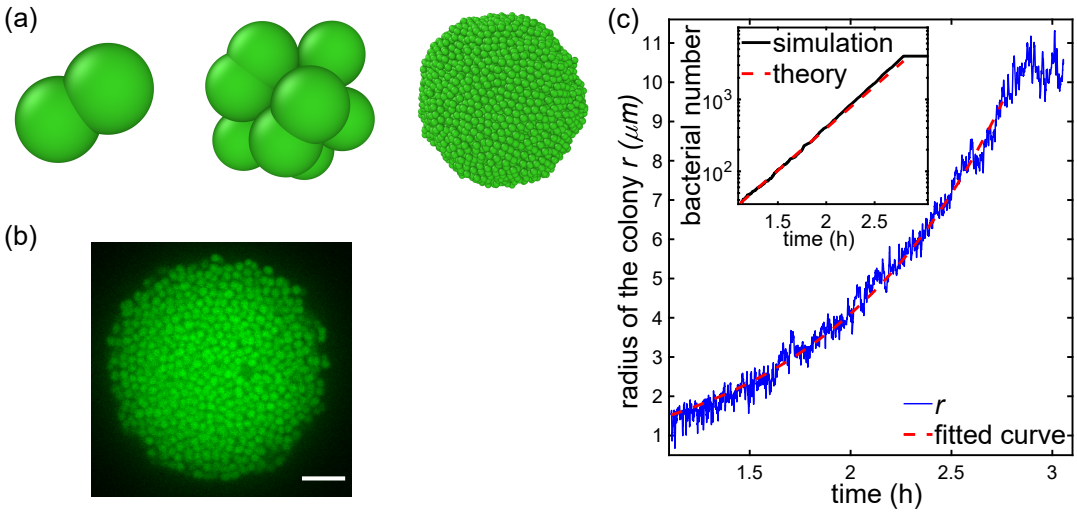

Figure 3.1: Simulations of growing colonies. (a) Simulation snapshots showing colony formation. (b) Confocal section of a microcolony of fluorescently labeled *N. gonorrhoeae*. Scale bar: $5\,\mu$m. (c) Cell numbers and colony radii increase exponentially with time in the simulations before growth and division are switched off.

3.3 Pilus-mediated interactions determine local colony order

To establish that the parameter values chosen for simulating pilus dynamics and forces correspond to measured values for *N. gonorrhoeae*, the distributions of rupture forces in our simulations are recorded. For adjusting the parameters governing pilus binding and rupture, simulation results are compared with measured rupture force distributions, see Fig. 3.2(a,b). The rupture-force values used for Fig. 3.2(a) correspond to data in Ref. [16], where the experimental procedures are explained in detail. To examine how the active force generation affects the mobility of cells in colonies, we next compare the simulated long-time diffusion coefficient of cells in colonies with stationary size with experimental data published in Ref. [147], see Fig. 3.2(c). Consistent with the experimental results and previous computational work [28,

147], diffusive motion of cells decreases at the center of the colonies. These gradients in mobility are not a result of graded mechanical activity because all cells in the simulations have the same properties. Rather, the reduced motion inside the colonies is due to a "caging" of every cell by its neighbors [148]. This mutual obstruction of movement is reduced at the periphery of the colony as a result of the lower cell density. Treatment of the colonies with the antibiotic azithromycin reduces the T4P-T4P binding among neighboring cells. Accordingly, cell motility in colonies treated with azithromycin is increased, Fig. 3.2(c,inset) [147]. Note that the employed concentrations of azithromycin do not completely abolish T4P retraction or lead to a high cell death rate. In simulations, the reduced pilus interaction of azithromycin-treated cells are represented by variation of the binding constant for T4P, k_{bind}, Fig. 3.2(c).

Next, the local order in simulated colonies is investigated. The degree of local ordering is characterized by the radial distribution function (RDF), which is the average local particle density at distance r from any reference particle, normalized by the average particle density of the system [158, 159]. The RDF is defined as

$$g(r) = \frac{V}{N} \sum_{i=1}^{N} \frac{\phi_i(r)}{N V_{\mathrm{shell}}(r)}, \tag{3.5}$$

where $\phi_i(r)$ is the number of particles whose distance to the ith particle is between $r - \Delta r$ and $r + \Delta r$ with $\Delta r = 0.05\,\mu\mathrm{m}$, $V_{\mathrm{shell}}(r)$ is the volume of the shell between radii $r - \Delta r$ and $r + \Delta r$, N is the total number of particles in the system, and V is the volume of the colony. In Fig. 3.2(d,e), the RDFs of bacteria inside stationary, non-growing colonies are displayed. For cells carrying $2 - 12$ pili, which corresponds to the experimentally established number for wild-type *N. gonorrhoeae*, the RDFs have the typical characteristics seen for liquids with multiple, maxima that are decreasing in magnitude with increasing r. Hence, pilus-based cell-cell interaction generates structures with short-range order. Since the pili also cause relative motion of the bacteria, decreasing pilus retraction speed increases the spatial ordering as can be seen in Fig. 3.2(d). Higher numbers of pili result in more pronounced maxima and therefore to a higher degree of spatial ordering, Fig. 3.2(e). Experimentally, a lower number of T4P can be induced by treatment of the colonies with sub-inhibitory concentrations of antibiotics [146, 147]. Figure 3.2(f) displays experimentally measured RDFs for wild-type cells and azithromycin-treated cells. Distances in this plot are scaled by the different mean diameters of the bacteria. Lowering the number of T4P by azithromycin treatment reduces the

local ordering, which is in good qualitative agreement with the simulation results. Experiments were performed as described previously in Ref. [147].

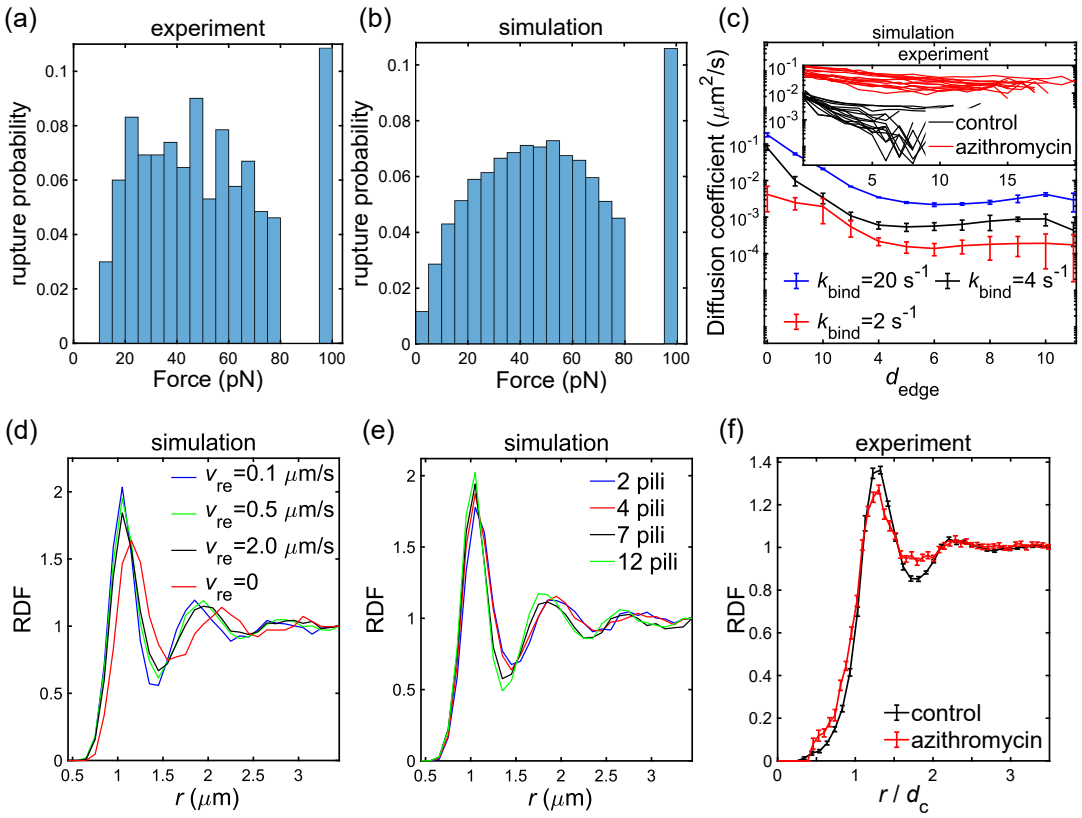

Figure 3.2: Pilus-generated forces and local colony order. (a) Experimental results for the distribution of pilus-pilus bond rupture forces measured with an optical trap [25]. Forces above 80pN cannot be measured precisely, the histogram bar at 100pN represents the contribution of all forces over 80pN. (b) Distribution of pilus-pilus bond rupture forces in simulations. (c) Diffusion coefficient of bacteria as a function of distance from the colony edge d_{edge} in simulations. Error bars show standard deviations of 3 samples. Inset: experimental data for wild-type cells and azithromycin-treated cells [147]. (d) Radial distribution function (RDF) of cells inside simulated colonies for different pilus retraction velocities. The shape of the functions, with decreasing, quasi-periodic maxima resembles the RDF of a liquid. For passive pili ($v_{\mathrm{re}} = 0$), $k_{\mathrm{bind}} = 2\,\mathrm{s}^{-1}$ is used, compare Tab. 2.1. (e) The maxima in the RDF become more pronounced with increasing numbers of pili per cell, thus, pili promote ordering. (f) Experimentally determined RDF for wild-type cells and azithromycin-treated cells with fewer T4P [147]. The cell diameter d_{c} is 1.02μm for the untreated control cells and is 1.42μm for the azithromycin-treated cells. Error bars are the standard error of the mean, over 24 colonies.

3.4 Active phase segregation in mixed colonies

Experimentally, strains carrying mutations affecting the T4P machinery have been found to segregate during formation of colonies [28, 145]. Bacterial segregation was seen to be dependent on the number of pili per cell, on post-translational pilus modifications that modify binding properties, and on the ability of bacteria to retract their pili. The observed colony morphotypes were suggested to be in agreement with the so-called differential-strength-of-adhesion hypothesis [160], which proposes that contractive activity of cells in addition to differential adhesiveness drives cell sorting. While active force generation was seen to be necessary for defined morphologies of mixed microcolonies, an experimental separation of the effect of pilus activity from differential adhesiveness is challenging due to the molecular complexity of pili. Simulations allow the systematic study of how variation of different parameters affects segregation.

To establish that the simulations produce results that are consistent with experimental data, experimentally studied cases of colony segregation are re-investigated. We first simulate simultaneous growth of two kinds of strains carrying different numbers of pili, as studied experimentally in Ref. [145]. In simulations, the growing colonies segregate and the cells that have many pili concentrate in the center of the colony, while cells with fewer pili form a spherical shell in the periphery, see Fig. 3.3(a). Qualitatively, this configuration can be explained by the hierarchy of interaction strengths, as explained in Ref. [145]. The mutual attraction of a pair of cells with many pili is larger than the attraction of a cell with many pili to a cell with few pili. The weakest attraction occurs among pairs of cells with few pili. The formation a shell of weakly-binding cells in the periphery is energetically advantageous because of the reduction of surface-energy cost. For binary mixtures of bacteria with different pilus-rupture probabilities, other hierarchies of interaction strength are possible. For a mixture of two cell types that have high pilus rupture forces among each other, but lower rupture forces for pairs of different cells, simulations show the formation of two segregated half-spheres during growth, see Fig. 3.3(b). This is consistent with experimental results, where wild-type cells were mixed with mutants deficient in post-translational pilin glycosylation [145].

Previous work on pilus-driven self-assembly of colonies has shown that binary cell mixtures consisting of cells with intact and retraction-deficient pili

segregate [20, 28]. To learn more about the segregation dynamics in this case, we start our simulations with fully grown colonies consisting of random binary cell mixtures, see Fig. 3.3(c). Half of the cells can retract their pili and the other half are retraction-deficient. Since both cell types have the same number of pili, no differential in adhesiveness exists. Nevertheless, the initially random distribution of different cell types gradually disappears and the retraction-deficient cells accumulate at the periphery of the simulated colony, as found in Ref. [20]. Unexpectedly, our simulations also predict the existence of a metastable intermediate state, in which active, pilus-retracting cells form a concentric spherical shell inside the colony, see Fig. 3.3(c, t_2). This intermediate state has to our knowledge not yet been observed experimentally. The lifetime of the predicted intermediate state depends on the pilus-based interactions and on the strength of the cell-cell repulsion. We quantify the effect of pilus-retraction velocity and cell-cell repulsion on the appearance of the metastable concentric shell. Heat-maps of the average lifetimes of the concentric spheres as a percentage of the simulation time are shown in Fig. 3.3(d) and (e). For short-ranged pilus interactions, the concentric shell of retracting cells inside the colony hardly appears, see Fig. 3.3(d), ($d_{\mathrm{bind}} = 2$). Likewise, this metastable state is suppressed if pilus-mediated interactions are limited to the next neighbors via Voronoi tesselation. The appearance of the metastable state requires long-ranged pilus-pilus interactions and rather stiff repulsive potentials among cells, see Fig. 3.3(e) ($d_{\mathrm{bind}} = 3$). Through such long-ranged pilus-pilus interactions, cells can exert forces on other cells that are not their direct neighbors. Experimentally, it has been established that the length of T4P follows an exponential distribution with a length scale around $0.8\,\mu\mathrm{m}$ and measured maximum lengths up to $5\,\mu\mathrm{m}$ [161]. Thus, the average T4P length is about the diameter of a coccus. For our simulations, we therefore chose a default binding cutoff equal to 1.5 times the cell diameter plus two times the cell radius ($d_{\mathrm{bind}} = 2.5$). Experimentally, longer-ranged interaction forces could occur for bacteria under stress conditions that affect T4P dynamics [161] or in situations where extracellular matrix constituents, such as polysaccarides or DNA, transmit forces inside colonies. The simulation results suggest that an experimental observation of a metastable concentric shell during phase separation would point toward the existence of such long-ranged, pilus-based interactions among bacteria.

Figure 3.3(f) shows plots of the diffusion coefficient of cells as a function of the distance from the colony center. For cell colonies consisting of one cell

type, diffusive motion of cells decreases at the center of the colonies as already shown above. In contrast, for segregated colonies consisting of cells with retracting and non-retracting pili, the diffusion constant decreases with the distance from the colony center. This position-dependence of the cell mobility is consistent with the increasing concentration of pilus-retraction-deficient cells at the periphery of the colony, see Fig. 3.3(g).

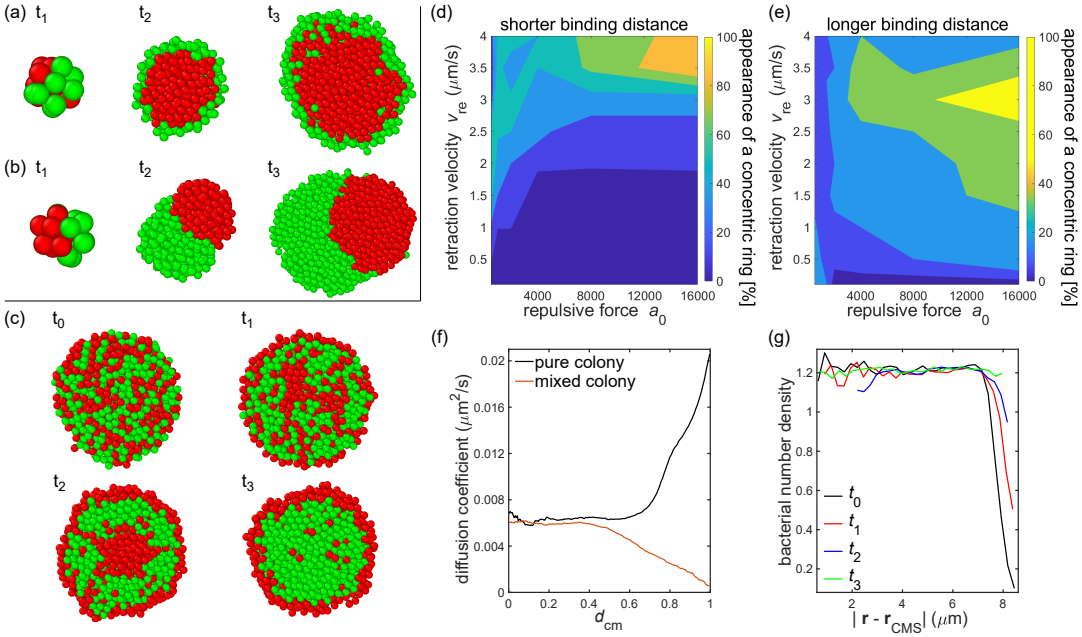

Figure 3.3: Caption next page.

Figure 3.3: (Previous page.) Phase segregation of mixed colonies. (a) Simulation snapshots for a growing colony from t_1 to t_3 consisting of cells with 14 pili (red) and cells with 7 pili (green). (b) Snapshots of the simulated growth from t_1 to t_3 of a mixture of wild-type cells (WT, green) and mutants deficient in post-translational pilin glycosylation (GD, red) [145]. Pilus rupture forces are as follows: $F_{\rm rupt}^{\rm WT-WT} = 22.5\,{\rm pN}$, $F_{\rm rupt}^{\rm GD-WT} = 20\,{\rm pN}$, $F_{\rm rupt}^{\rm GD-GD} = 45\,{\rm pN}$. In (a) and (b), Voronoi tessellation is used to locate neighbors for pilus binding. (c) Segregation of a binary mixture of wild-type bacteria (green) and pilus-retraction-deficient cells (red). Pilus-mediated interactions are long-ranged in this example with $d_{\rm bind} = 2.5\,\mu{\rm m}$. At time t_0, the colony is randomly mixed. Over time, the proportion of pilus-retraction-deficient cells increases in the colony periphery, t_1, and wild-type cells then accumulate in a concentric sphere inside the colony, t_2. The concentric sphere eventually disappears and wild-type cells accumulate in the colony center, t_3. (d) Lifetime of the concentric sphere arrangement for short-ranged pilus interactions, $d_{\rm bind} = 2.5\,\mu{\rm m}$. Lifetimes are given in percent of the longest observed lifetime (3000s). (e) Lifetime of the concentric sphere arrangement for long-ranged pilus interactions, $d_{\rm bind} = 3.5\,\mu{\rm m}$. Lifetimes are given in percent of $3000\,{\rm s}$. (f) Diffusion coefficients of individual cells as a function of their distance from the colony center divided by the colony radius, $d_{\rm cm}$. Pure colonies consist of one type of cells, the mixed colony is the segregated system shown in (c, t_3). (g) The mean radial number density of wild-type cells (green) for the simulation snapshots shown in (c).

3.5 Non-equilibrium fluctuations of colony boundaries

The position fluctuations of cells in colonies on the one hand provide information about the viscoelastic properties of the system and, on the other hand, carry information about the non-equilibrium forces holding the system together. While it is trivial to keep track of cell positions in simulations, a high-precision measurement of cell positions inside a three-dimensional colony is challenging in experiments. However, it is possible to image whole colonies with high frame rate and subsequently extract the colony edges from the images. Thus, the non-equilibrium fluctuations of colony boundaries are observable. We mimic here such a measurement in simulations by tracking cells located in a fixed small sector at the edge of colonies in the stationary state, as shown in Fig. 3.4(a). In this setup, a movement of bateria at the colony edge can either result from thermal noise or the activities of pili. Colonies are grown in simulations using wild-type cells. After switching off colony growth, the role of pilus activity for the stationary state is studied.

The decay time of the velocity autocorrelation function (VACF) in the stationary state without active pilus-mediated forces, $v_{\mathrm{re}} = 0$, corresponds to the inertial time scale in simulations. Thus, we roughly have an inertial decay time $t_{\mathrm{inert}} \simeq 0.1\, k_{\mathrm{rupt}}^{-1}$ (simulation units), see Fig. 3.4(b). The cell motion resulting from pilus retraction strongly increases the VACF below the time scale of pilus-bond rupture $k_{\mathrm{rupt}}^{-1} = 1\,\mathrm{s}$.

With the radial distance $r_{\mathrm{CMS}}(t)$ between the center of mass and the edge of the colony, the deviations from the time average are given by $X(t) = (r_{\mathrm{CMS}}(t) - \langle r_{\mathrm{CMS}} \rangle)$. The power spectral density (PSD) of the displacement is given by

$$P(\omega) = \frac{|\widetilde{X}(\omega)|^2}{s\, n}, \tag{3.6}$$

where $\widetilde{X}(\omega)$ is the discrete Fourier transform of $X(t)$, s is the sampling rate, and n is the number of data points. The PSDs of the radial motion of bacteria at the boundary in our simulated colonies are shown as Fig. 3.4(c). Fluctuations with frequencies $\omega \lesssim 10\,\mathrm{Hz}$ are expected to be experimentally accessible. For $\omega > 2\pi/t_{\mathrm{inert}} \simeq 50\,\mathrm{Hz}$, the results are not expected to match with experiments since here inertial effects start to play a role the in simulations.

First, retraction-deficient, passive pili with $v_{\mathrm{re}} = 0$ are considered. Since these pili only form temporary bonds between the cells, they produce an effective friction among cells. The boundary fluctuation are similar to the motion of an overdamped particle in a purely viscous environment $P(\omega) \propto \omega^{-2}$. Second, for retraction-deficient, passive pili that form permanent bonds ($v_{\mathrm{re}} = 0$, no rupture), we find boundary fluctuations that are similar to the motion of an overdamped particle in an harmonic potential with $P(\omega) \propto \mathrm{const.}$ at low frequencies and $P(\omega) \propto \omega^{-2}$ for high frequency (not shown). Third, wild-type cells with retracting T4P are considered ($v_{\mathrm{re}} = [0.5, 2]\,\mu\mathrm{m/s}$). In this case, pilus retraction on the one hand enhances the elastic forces among cells, on the other hand, increases the rupture rate of bonds formed by T4P. Overall, the activity of T4P results in visco-elastic material properties with a pronounced elastic response at low frequencies. Simulations show that this elastic response does not occur if temporary cell-cell connections are formed by passive links.

The inset of Fig. 3.4(c) show experimental results for the PSDs of wild-type cells and a strain carrying inactivating deletions in genes that encode the phosphotransferase *pptA*, which required for the post-translational modification of T4P (*ΔpptA*). Experiments were carried out as described in Ref. [25].

For wild-type cells, where colony contains around 4000 cells, the experimentally measured colony boundary fluctuations up to 10 Hz are in good qualitative agreement with our simulation results. For a qualitative assessment of the experimental data for the *ΔpptA* strain, a smaller colony with about 600 mutants is simulated. Here, the parameters governing T4P dynamics are adjusted to mimic the higher binding probablility and lower rupture frequency measured for the *ΔpptA* strain in comparison to the wild-type [25]. A binding rate of $k_{\mathrm{bind}}^{\mathrm{mutant}} = 50\,\mathrm{s}^{-1}$ and lower rupture rate $k_{\mathrm{rupt}}^{\mathrm{mutant}} = 1\,\mathrm{s}^{-1}$ were chosen, compare Tab. 2.1. We also find that a lower retraction velocity needs to be chosen for the simulated mutant strain, compared to the wild-type strain ($v_{\mathrm{re}} = 0.5\,\mu\mathrm{m/s}$). This lower retraction velocity is necessary in simulations to mimic the lower retraction frequency of the mutant [25] and reduces the apparent elastic modulus at low frequencies. Overall, the higher plateau value of the PSD at low frequencies suggest that post-translational modification of T4Ps in wild-type cells leads to "stiffer" *N. gonorrhoeae* colonies.

Since shape fluctuations of a wild-type cell colony mainly result from active forces, a violation of the equilibrium fluctuation-response relation is expected. To find out how a fluctuation-response relation can be measured experimentally, we simulate a setup for controlled mechanical perturbation of the colony boundary. This setup is inspired by techniques for measuring active fluctuations in cell membranes [162]. We fix a simulated colony between walls and stick a bead with radius $R_{\mathrm{B}} = 1.5\,\mu\mathrm{m}$ onto one side of the colony, see Fig. 3.4(d). The same parameter values are used to describe pilus interaction with walls and pilus-pilus interaction. The pairwise interactions between the bead and the cells is modeled with a Morse potential. Denoting the distance between the bead and any neighboring cell i by $r_{i,\mathrm{B}}$, the potential is given by

$$\Psi_i^B(r_{i,\mathrm{B}}) = c_{\mathrm{mors}}\left[e^{-2\beta(r_{i,\mathrm{B}}-R_{i,\mathrm{B}})} - 2e^{-\beta(r_{i,\mathrm{B}}-R_{i,\mathrm{B}})}\right], \qquad \text{for } r_{i,\mathrm{B}} \le d_{\mathrm{mors}}, \tag{3.7}$$

$$\Psi_i^B(r_{i,\mathrm{B}}) = \Psi_i^B(d_{\mathrm{mors}}), \qquad \text{for } r_{i,\mathrm{B}} > d_{\mathrm{mors}}, \tag{3.8}$$

where sum of the radii of cell and beads is given by $R_{i,\mathrm{B}} = R + R_{\mathrm{B}}$. The cutoff for the interaction potential is set at $d_{\mathrm{mors}} = 3.1\,\mu\mathrm{m}$. Other parameter values of the potential are fixed as $c_{\mathrm{mors}} = 10\ \mathrm{pN}\mu\mathrm{m}$ (energy unit: $f_c d_c$) and $\beta = 1\,\mu\mathrm{m}^{-1}$. The radial displacement of the bead relative to the center of the colony, $x(t)$, is employed to quantify the fluctuations of the colony boundary through a PSD $P(\omega)$ given by Eq. (3.6). Alternatively, a sinusoidally varying force $F_{\mathrm{ext}}(t)$ is applied to the beads' center, pointing towards the colony center. The Fourier

transform of the force is given by $\hat{F}_{\mathrm{ext}}(\omega)$ with angular frequency ω. The response function is given by

$$\hat{\chi}(\omega) \equiv \frac{\hat{x}(\omega)}{\hat{F}_{\mathrm{ext}}(\omega)}. \tag{3.9}$$

The imaginary part of the response function $\hat{\chi}(\omega)$ is denoted by $\hat{\chi}'(\omega)$ and we define the quantity $H(\omega) \equiv -\hat{\chi}'(\omega)2k_BT/\omega$. For systems in thermal equilibrium, the fluctuation-response theorem states that

$$P(\omega) = H(\omega). \tag{3.10}$$

For colonies consisting of bacteria with retraction-deficient, passive pili and permanent bounds ($v_{\mathrm{re}} = 0$), Eq. (3.10) is satisfied and the fluctuation-response theorem holds as expected, see Fig. 3.4(e). In simulations of colonies consisting of wild-type bacteria that can retract their pili ($v_{\mathrm{re}} = 1.0\,\mu\mathrm{m/s}$) and form dynamic bonds with other cells, the equilibrium fluctuation response relationship is violated across the whole experimentally relevant frequency range of $[0 - 10]\,\mathrm{Hz}$. Note that constraining the colony in between walls and then tracking the motion of a bead is not equivalent to tracking the distance of the colony boundary from its center. Hence the spectral densities in Figs. 3.4(c),(f) are different. For wild-type bacteria, the simulations predict a very strong deviation from Eq. (3.10), where $P(\omega)$ is several orders of magnitude larger than $H(\omega)$. Such deviations are likely measurable in experiments.

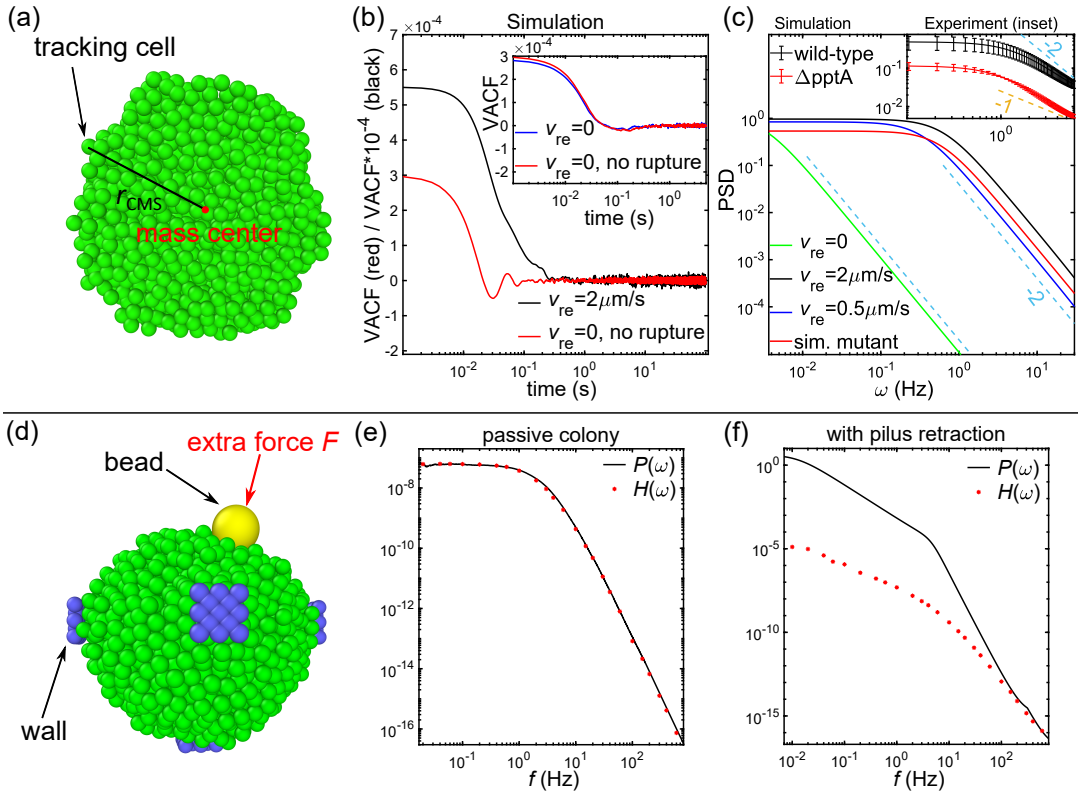

Figure 3.4: (a) Simulated setup for quantifying boundary fluctuations by measuring the radial distance r_{CMS} between a fixed angular position on the surface and the colony center. (b) Active pilus retraction results in a slower decay of the velocity autocorrelation function (VACF) of the surface point. Main plot: colonies are first grown from cells with retracting pili and the role of pili is studied after growth is switched off. Inset: colonies are grown with retraction-deficient cells. (c) Active pilus retraction produces a power spectral density of fluctuations characteristic for a visco-elastic material with an elastic behavior at low frequencies. For passive colonies, $v_{\mathrm{re}} = 0$, bond rupture results in a viscous material behavior. Colony size is 4000 cells. For comparison with experimental data, a small colony with 600 mutant cells is simulated having a higher binding rate $k_{\mathrm{bind}}^{\mathrm{mutant}} = 50\,\mathrm{s}^{-1}$, lower rupture rate $k_{\mathrm{rupt}}^{\mathrm{mutant}} = 1\,\mathrm{s}^{-1}$ and lower retraction velocity $v_{\mathrm{re}} = 0.5\,\mu\mathrm{m/s}$. Inset: experimental data for wild-type cells and a *ΔpptA* strain, error bars show standard deviations of the 3 samples. (d) Simulated setup for colony-shape perturbation. (e) Simulated mutant colonies with retraction-deficient pili that form permanent bonds. The equilibrium fluctuation-response relationship holds. (f) For simulated wild-type cells, the equilibrium fluctuation-response relationship is strongly violated ($v_{\mathrm{re}} = 1.0\,\mu\mathrm{m/s}$, $d_{\mathrm{bind}} = 3.0\,\mu\mathrm{m}$)

3.6 A first look at active colony spreading on a surface

An important aspect of growing bacterial colonies is the colonization of surfaces and the invasion of tubes and channels. In this subsection, we present first results about interaction of cells with surfaces. An in-depth study of the surface-wetting behavior of colonies is presented in the next chapter. To investigate the role of active adhesion forces for the colony behavior in such situations, we consider the interaction of cells with walls that provide attachment sites for pili. Walls are represented by a layer of immobile, soft spheres. Cell-wall interactions are represented by the same conservative potential employed for cell-cell repulsion. Since biomolecular binding affinities are typically determined by the unbinding rate, the pilus unbinding rate k_{plane}, corresponding to k_{rupt} for pilus-pilus unbinding, is varied. The other parameters governing pilus-wall binding are assumed to be the same as for pilus-pilus interactions, see Tab. 2.1. Experimentally, such wall properties can be realized, e.g., by coating hydrogel surfaces with pilin.

For colonies spreading on a planar wall, the shape results from a competition between the cell-cell interactions within the colony and the interactions of the cells with the substrate. Previous simulation studies showed that the radius of the contact zone between the colony and the wall increases with the rupture force scale [20], which can be called "partial wetting". Here, we vary the dissociation-rate constant of the pilus-wall bonds to assess the wetting transition. Simulation snapshots of colonies growing on a planar surface are shown in Fig. 3.5(a-c). If the dissociation-rate constant of the pilus-wall bonds is smaller than the dissociation rate constant for pilus-pilus bonds, $k_{\mathrm{plane}} \lesssim 2\,\mathrm{s}^{-1} < k_{\mathrm{rupt}} = 3\,\mathrm{s}^{-1}$, we find that the colonies dissolve and the bacteria are evenly dispersed along the surface, see Fig. 3.5(a,d), which corresponds to complete wetting. For $k_{\mathrm{plane}} \geq k_{\mathrm{rupt}}$, the colonies assume rounded shapes that can still remain in loose contact with the surface, see Fig. 3.5(b,c). To assess the dynamics of the wetting process, we next record the diameter d_{surface} of the contact zone of a spreading colony on the surface. For a passive, Newtonian fluid on a planar surface, the diameter of a spreading droplet asymptotically obeys a power-law dependence on time t as $d_{\mathrm{surface}} \sim t^{\vartheta}$, known as Tanner's law [163–165]. The exponent ϑ depends on droplet size and on the dimension. Droplets that are much smaller than the capillary length obey in three dimensions for long times the scaling $\sim t^{1/10}$ [165],

which results from a leading-order balance of capillary forces with dissipation close to the wetting line. It has also been theoretically predicted that thermal fluctuations promote spreading of nanodroplets and lead to a scaling of $\sim t^{1/6}$ [166]. In our simulations of active bacterial colonies, a regime with the classical passive-liquid scaling $\sim t^{1/10}$ is not observed. Rather, we find that the diameter d_{surface} obeys a power law with an exponent close to $1/4$, which is very similar for different parameter choices, see Fig. 3.5(e). Such a scaling indicates that the dynamics is dominated by a balance of surface-attraction and dissipation in the bulk of the colony. The scaling breaks down at long times when the colony reaches a stationary, rounded shape on the surface.

3.7 Active colony invasion of narrow channels

We next simulate the invasion of small channels by colonies. The colonization of protective niches can present a selective advantage in abiotic environments and can also be an important aspect of host-pathogen interaction. Previous work on *Neisseria meningitidis*, the causative agent of meningitis, showed that attractive forces generated by T4P fluidize the bacterial colonies, which is required for efficient colonization of the blood capillary network during infection. Furthermore, simulations of *N. gonorrhoeae* migration through asymmetric corrugated channels show a rectification of motion for active bacteria [4]. However, a systematic assessment of the conditions necessary for the active invasion of constrictions is missing. To focus on the role of pilus activity, we only consider colonies that are not growing or dividing and channels are represented with the same methods as walls in Sec. 3.6.

Like for cell-surface interaction, the behavior of active colonies is seen to be qualitatively similar to a liquid minimizing surface energy. Active pilus retraction can cause a rapid and complete invasion of the channel, see Fig. 3.6(a-e). For passive cells ($v_{\mathrm{re}} = 0$), colonies can attach to the walls but proper invasion of the whole channel is not observed, see Fig. 3.6(f). A complete entrance of passive colonies into the channels never occurs in our simulations, even for large surface affinity, $k_{\mathrm{plane}} \simeq 0.01\,\mathrm{s}^{-1}$, and very long simulation times. For active colonies, the onset of channel invasion occurs rather suddenly when increasing the affinity for the substrate ($\sim 1/k_{\mathrm{plane}}$), see Fig. 3.6(d). However, the threshold value of k_{plane} below which channel invasion occurs is not the same as the threshold required for complete wetting of a planar substrate shown in Fig. 3.5. The reason for different threshold affinities is presumably

that the formation of a monolayer of cells on a planar surface is energetically more costly than formation of a cylindrical colony with finite internal volume. Consistent with this interpretation, we find that the narrower the channel is, the higher the surface-binding affinity has to be to achieve channel invasion, see Fig. 3.6(g). For very narrow channels, $w \lesssim 2.5\,\mu\mathrm{m}$, we find that the invasion does not occur through collective motion of an intact colony but that individual cells and small collections of cells break off from the colony and individually explore the channel, see Fig. 3.6(e). A possible cause for this break-up is that the high curvature of very narrow channels results in a surface area per cell that is larger than the surface area per cell on a plane. Since the number of T4P is limited, the geometry of narrow channels increases the effective binding affinity between cells and walls and decreases the effective binding affinity among cells is reduced. The break-up of colonies during invasion of these channels is therefore due to the finite inherent length scale of the "bacterial active fluid".

To quantify the dynamics of colony invasion, we next record the speed of the front of the colony moving down the channel and plot it as a function of the enter length $L(t)$, see Fig. 3.6(h). For passive liquids, the penetration dynamics into horizontal capillary tubes under the assumption of negligible gravity and inertia obeys an approximate scaling of $L(t) \sim \sqrt{t}$, which is derived as follows [167]. The liquid viscosity is denoted by η_p, the presumably constant surface-contact angle is θ_p, the surface tension is σ_p and the channel diameter w. Then, the balance of capillary driving force with viscous friction can be written as $8\eta_\mathrm{p} L(t)\dot{L}(t)/w^2 = \sigma_\mathrm{p}\cos\theta_\mathrm{p}/w$. Solution of this differential equation for $L(t)$ yields the Lucas-Washburn equation [168, 169]

$$L(t) = \sqrt{\frac{w\,\sigma_\mathrm{p}\cos\theta_\mathrm{p}}{8\,\eta_\mathrm{p}}}\sqrt{t}. \tag{3.11}$$

For our active colonies, we find that the invasion dynamics for thin channels of width $w = 3.3\,\mu\mathrm{m}$ obey the $L(t) \sim \sqrt{t}$ scaling of passive liquids. These channels are wide enough to prevent colony break-up. For thicker channels the Lucas-Washburn-like scaling no longer holds in our simulations, as is the case for passive liquids, where the deviations are attributed to inertial effects and to a dependence of the contact angle on the wetting dynamics.

Overall, channel invasion by active bacterial colonies displays a striking qualitative similarity to capillary wetting by passive liquids. However, for passive colonies, having a mesoscopic internal length scale, we do not observe

channel invasion in simulations. The main role of pilus-mediated random activity is to increase the fluidity and to thereby change the dynamics of colony-surface interactions. Thus, T4P activity allows the occurrence of channel invasion and surface spreading on biologically relevant time scales.

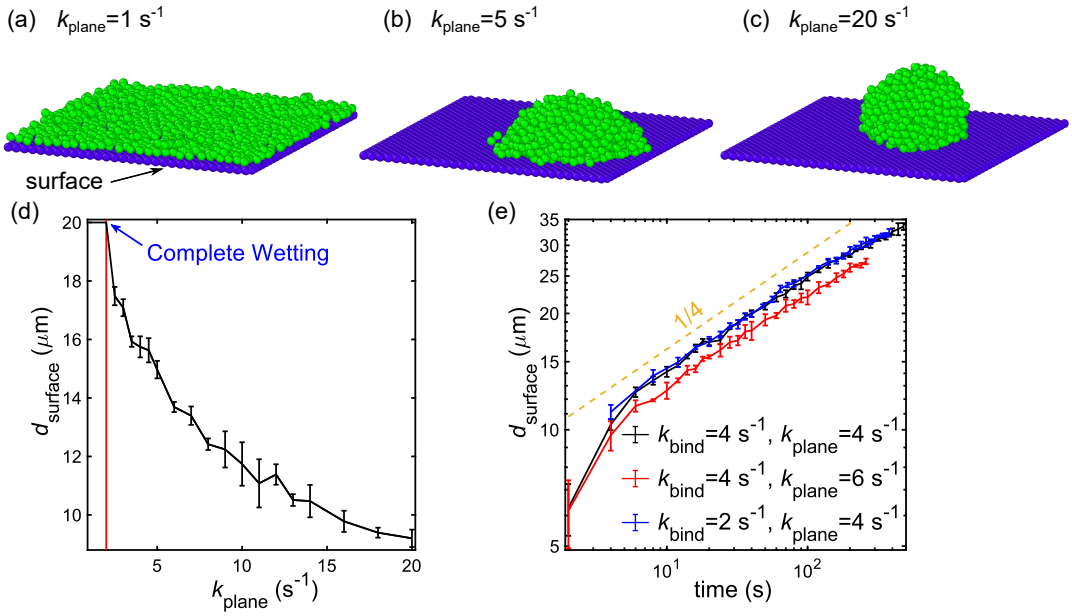

Figure 3.5: (a-c) Colonies spreading on planar surfaces. Depending on the dissociation rate constant of pilus-surface bonds, k_{plane}, colonies undergo a partial or complete wetting transition. (d) A complete wetting occurs when $k_{\mathrm{plane}} \ll k_{\mathrm{rupt}} = 2\,\mathrm{s}^{-1}$. Error bars represent sample standard deviations. (e) The time dependence of the diameter of the spreading colony, d_{surface}, obeys approximately a power law. If not given otherwise, pilus-substrate binding rates and rupture forces are assumed to be the same as for pilus-pilus bonds, see Tab. 2.1. Error bars represent standard deviations of the 3 samples.

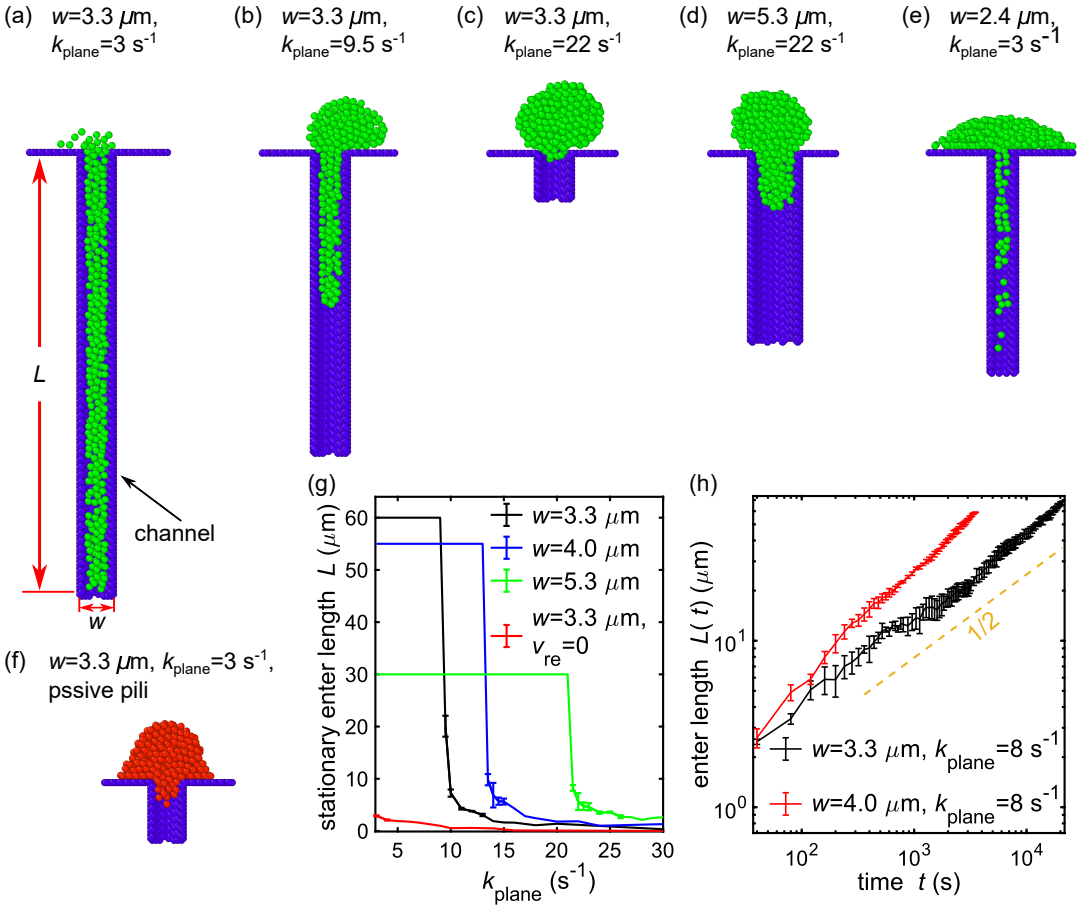

Figure 3.6: Colonies atop surfaces containing channels. (a-c) Simulated wild-type colonies that are initially positioned on top of a narrow channel can invade the channel by making use of pilus activity if the pilus-substrate bonds are strong. The length that a colony enters a channel is denoted by L. (d) Colonies more easily invade a wider channel. (e) Invasion of very narrow channels is possible, but colonies break up in this geometry (f) Passive colonies are not seen to invade channels fully in simulations. (g) Stationary lengths of colonies after entering channels of different widths. Depending on the channel width, full entrance of the colony occurs below a critical value of k_{plane}. (h) The time evolution of the enter length is described approximately by a power law. Error bars represent standard deviations of the 3 samples.

3.8 Summary

We have introduced a simulation model to study the non-equilibrium structure and dynamics of colonies of active, growing bacteria on different time- and length scales. Bacterial cells are modeled with an algorithm akin to dissipative particle dynamics. Parameter values are carefully chosen to allow comparison of the simulation results with experimental measurements.

We investigate different physical aspects of *N. gonorrhoeae* colonies, including growth dynamics, local ordering, and self-sorting of bacteria in colonies. Simulation results are in good qualitative agreement with experimental data. We also propose a setup for measuring fluctuations in the colony shape and its response to external force. The simulations predict a strong, measurable violation of the equilibrium fluctuation-response relationship. Furthermore, the model shows that actively fluctuating adhesion forces can allow the bacterial invasion of narrow channels. Thus, active force generation is not only required for bacterial migration, but can determine the rheology of cell colonies and drive the colonization of constricted environments, which represent central aspects for host infection and bacterial contamination of abiotic environments. At present, basic physical mechanisms underlying the collective interaction of active particles with complex surfaces are hardly understood. We expect that future experimental and theoretical work on the non-equilibrium properties of bacterial colonies will generate insights that deepen our understanding of the emergent properties of such active matter systems.

3.9 Appendix

3.9.1 Power spectral density

According to Parseval's theorem the total energy of a signal can be calculated by integrating the intensity in the time domain or the Fourier-transformed signal in the frequency domain as

$$E = \int_{-\infty}^{\infty} |x(t)|^2 \mathrm{d}t = \int_{-\infty}^{\infty} |\hat{x}(f)|^2 \mathrm{d}f, \tag{3.12}$$

where $\hat{x}(f) \equiv \int_{-\infty}^{\infty} x(t) e^{-2\pi i t f} dt$ is the Fourier transform of $x(t)$.

For discrete-time signals, the discrete Fourier transform (DFT) yields

$$\sum_{n=0}^{N-1} |x[n]|^2 = \frac{1}{N} \sum_{k=0}^{N-1} |\hat{x}[k]|^2. \tag{3.13}$$

The average power P of a signal $x(t)$ is given by the following time average

$$P = \lim_{T\to\infty} \frac{1}{2T} \int_{-T}^{T} |x(t)|^2 \mathrm{d}t = \frac{1}{2\pi} \int_{-\infty}^{\infty} S(\omega) \mathrm{d}\omega, \tag{3.14}$$

where the PSD is given by

$$S(\omega) \equiv \lim_{T\to\infty} \frac{1}{2T}|\hat{x}(\omega)|^2. \tag{3.15}$$

The Wiener-Khinchin theorem states that the PSD of a stationary random process is given by the Fourier transform of the autocorrelation function of that process

$$S(\omega) = \frac{1}{2\pi}\int_{-\infty}^{\infty} e^{-i\omega\tau} G(\tau)\mathrm{d}\tau, \tag{3.16}$$

where the autocorrelation function $G(\tau) = \lim_{T\to\infty} \frac{1}{T}\int_0^T x(t)x(t+\tau)\mathrm{d}t$.

Finally, the Nyquist-Shannon sampling theorem states that if a function $x(t)$ contains no frequencies higher than B hertz, it is completely determined by giving its ordinates at a series of points spaced $1/(2B)$ seconds apart. A sufficient sample-rate is therefore anything larger than $2B$ samples per second. Equivalently, for a given sample rate f_s, perfect reconstruction is guaranteed possible for a bandlimit $B < f_s/2$.

3.9.2 A fluctation-response relation for a two-particle system

We consider two particles 1 and 2 that are confined by harmonic potentials, and the two particles are coupled by a harmonic bond. We track the particle 1 and it's position is $x(t)$, the position of the particle 2 is $y(t)$. The two particles' Langevin equations can be described as

$$m_1\ddot{x}(t) = -\gamma_1\dot{x}(t) + k[y(t) - x(t)] - a_1x(t) + \xi_1(t) \tag{3.17}$$

$$m_2\ddot{y}(t) = -\gamma_2\dot{y}(t) - k[y(t) - x(t)] - a_2y(t) + \xi_2(t), \tag{3.18}$$

where

$$\langle\xi_1(t)\xi_1(t')\rangle = 2\gamma_1k_BT_1\delta(t-t') \tag{3.19}$$

$$\langle\xi_2(t)\xi_2(t')\rangle = 2\gamma_2k_BT_2\delta(t-t'), \tag{3.20}$$

where T_1, T_2 are two temperatures that determine the noise magnitudes.

Assuming over-damped motion of the second particle, we set $m_2 = 0$, so that we have

$$0 = -\gamma_2\dot{y}(t) - k[y(t) - x(t)] - a_2y(t) + \xi_2(t). \tag{3.21}$$

A Fourier transform yields

$$\hat{y}(\omega) = \frac{1}{i\omega + (k+a_2)/\gamma_2}[\frac{k}{\gamma_2}\hat{x}(\omega) + \frac{\hat{\xi}_2(\omega)}{\gamma_2}], \tag{3.22}$$

so we can describe $y(t)$ as

$$y(t) = [e^{-(k+a_2)t/\gamma_2}] * [\frac{k}{\gamma_2}x(t) + \frac{1}{\gamma_2}\xi_2(t)], \tag{3.23}$$

where we denote the convolution of two functions f and g as $(f*g)(t) \equiv \int_{-\infty}^{\infty} f(\tau)g(t-\tau)d\tau$. Inserting this solution into the Langevin equation (3.17), we obtain the generalized Langevin equation

$$\begin{aligned} m_1\ddot{x(t)} = &-\gamma_1\dot{x(t)} + k\{[e^{-(k+a_2)t/\gamma_2}] * [\frac{k}{\gamma_2}x(t) + \frac{1}{\gamma_2}\xi_2(t)] - x(t)\} \\ &- a_1x(t) + \xi_1(t), \end{aligned} \tag{3.24}$$

which reads in Fourier space

$$\begin{aligned} \{-m_1\omega^2 + i\gamma_1\omega + a_1 - k[\frac{1}{i\omega + (k+a_2)/\gamma_2}\frac{k}{\gamma_2} - 1]\}\hat{x}(\omega) = \\ k[\frac{1}{i\omega + (k+a_2)/\gamma_2}\frac{1}{\gamma_2}\hat{\xi}_2(\omega)] + \hat{\xi}_1(\omega). \end{aligned} \tag{3.25}$$

We denote the real part of the prefactor to $\hat{x}(\omega)$ by a and the imaginary part by b. Then, the equation reads

$$(a+ib)\hat{x}(\omega) = \hat{\xi}(\omega), \tag{3.26}$$

where

$$b = \gamma_1\omega + \frac{k^2\gamma_2\omega}{(k+a_2)^2 + \gamma_2\omega^2}. \tag{3.27}$$

From equation(3.26) we have the PSD of $x(t)$

$$C_x(\omega) = \frac{C_\xi(\omega)}{|a+ib|^2} = \frac{C_\xi(\omega)}{a^2+b^2}, \tag{3.28}$$

where

$$C_\xi(\omega) = C_{\xi_1}(\omega) + \frac{k^2}{(k+a_2)^2 + \gamma_2^2\omega^2}C_{\xi_2}(\omega) \tag{3.29}$$

$$= 2\gamma_1 k_B T_1 + \frac{k^2}{(k+a_2)^2 + \gamma_2^2\omega^2}2\gamma_2 k_B T_2. \tag{3.30}$$

By setting $T_2 = (1+\alpha)T_1$, we have

$$C_\xi(\omega) = 2k_B T_1[\gamma_1 + \frac{k^2(1+\alpha)\gamma_2}{(k+a_2)^2 + \gamma_2^2\omega^2}]. \tag{3.31}$$

Now, we add an external force $F(t)$ on particle 1, equation(3.26) can be written as

$$(a+ib)\hat{x}(\omega) = \hat{\xi}(\omega) + \hat{F}(\omega), \tag{3.32}$$

we define the response function by averaging over the noise

$$\hat{\chi}(\omega) \equiv \frac{\langle \hat{x}(\omega) \rangle}{\hat{F}(\omega)} \tag{3.33}$$

$$= \frac{a-ib}{a^2+b^2}. \tag{3.34}$$

So that we have

$$C_x(\omega) = \frac{C_\xi(\omega)}{a^2+b^2} = \frac{-\hat{\chi}'(\omega)}{b} C_\xi(\omega), \tag{3.35}$$

where $\hat{\chi}'(\omega)$ is the imaginary part of $\hat{\chi}(\omega)$. Inserting equation(3.31) into equation(3.35), we have

$$\frac{C_x(\omega)}{-\hat{\chi}'(\omega)2k_BT_1/\omega} = \frac{\gamma_1 + \frac{k^2(1+\alpha)\gamma_2}{(k+a_2)^2+\gamma_2^2\omega^2}}{\gamma_1 + \frac{k^2\gamma_2}{(k+a_2)^2+\gamma_2^2\omega^2}} \tag{3.36}$$

$$= 1 + \frac{k^2\gamma_2\alpha}{k^2\gamma_2 + (k+a_2)^2\gamma_1 + \gamma_1\gamma_2^2\omega} \tag{3.37}$$

When $T_1 = T_2$, so that $\alpha = 0$, we have Fluctuation-Response Relation (FRR)

$$\frac{C_x(\omega)}{-\hat{\chi}'(\omega)2k_BT_1/\omega} = 1. \tag{3.38}$$

When $T_1 \neq T_2$, so that $\alpha \neq 0$, the FRR is violated.

Chapter 4

Treatment with an antibiotic stimulates active surface wetting of bacterial colonies

4.1 Introduction

We start by describing the spreading dynamics of a passive liquid on a surface. The spreading behavior can be roughly divided into two stages; in the initial stage it spreads much faster than in the late time. For low-viscosity droplets, the initial spreading is dominated by inertia, and its spreading radius follows a power-law dependence on time t as $R \sim t^{1/2}$ [170–173], while for high-viscosity droplets the scaling is different [174]. At a late stage of the spreading process, the droplet assumes a shape that approximates a spherical cap, and the spreading radius asymptotically obeys a power-law as $R \sim t^{1/10}$, known as Tanner's law [163, 164, 175], which has been observed by many experiments [164, 176, 177]. For a large liquid drop,the effect of gravity on the spreading dynamics dominates surface tension and the spreading, the power law changes into $R \sim t^{1/8}$ [176, 178]. Thermal fluctuations can enhance spreading of nanodroplets which has been predicted to lead to a scaling of $R \sim t^{1/6}$ [166]. Taking into Navier slip condition, $u_s = L_s \partial u/\partial z$ with slip length L_s, the drop spreading behaviour will be affected [179]. Normally, slip length L_s is small compared to the drop thickness h, and dose not change the spreading law [180]. When the slip length is larger than the thickness, $L_s > h$, Tanner's law dose not hold anymore, and a faster spreading law $R \sim t^{1/8}$ shows up [181, 182]. If L_s is much large, it will lead a even faster $1/4$ law [183–185]. When considering both thermal fluctuations and slip condition, a faster spreading law will be obtained [186].

The wetting behavior of passive liquid droplets on surfaces has been extensively studied, but there is relatively limited research on the wetting behavior of active droplets, such as bacterial colonies, on surfaces. The effect of antibiotic treatment on the wetting behavior of bacterial colonies on surfaces is remains unclear.

In this chapter, we study wetting behavior of bacterial colonies spreading on surfaces experimentally and in simulations. We investigate the steady contact angle and spreading dynamic of colonies treated with different concentrations of antibiotics on the surface. We study the slip condition and shear viscosity of bacterial colonies on surfaces.

4.2 Steady-state contact angle

As a bacterial colony approaches a surface, the attachment of bacterial pili to the surface generates an interaction force that drives the colony to spread on the surface. This wetting behavior of the colony eventually reaches an equilibrium between surface tension and adhesion energy, leaving the colony in a steady state. At this point, the shape of the bacterial colony can be approximated as a segment of a sphere with a radius of $r_{\max}$, as shown in Fig. 4.1(a). The contact area between the colony and the surface can be approximated as a circle with a radius of r. Additionally, we refer to the angle formed between the colony and the surface as a steady-state contact angle θ. In most of the experimental data, the steady-state contact angle θ is greater than 90 degrees, indicating that $r < r_{\max}$.

Based on our computer simulations, we predicted that treatment with azithromycin increases the spreading radius of bacterial colonies. Subsequently, these predictions were experimentally verified in the laboratory of Prof. B. Maier, Cologne University. However, we start here by introducing the experimental results before explaining the theoretical analysis and computer simulations in depth. After treatment with azithromycin, tendency of bacterial colonies to wet a surface is enhanced. This implies a reduction in the steady-state contact angle θ of the colony, leading to a larger value of $r/r_{\max}$, as shown in Fig. 4.1(b).

Treating bacterial colonies with different concentrations of azithromycin, the values of $r/r_{\max}$ for the colonies at steady state are shown in Fig. 4.1(c). The minimum inhibitory concentration (MIC) of an antibiotic is the lowest concentration that can inhibit the visible growth of a specific microorganism

strain [187], the unit of antibiotics we use here is the MIC of azithromycin for *N. gonorrhoeae*. The wild-type bacterial colonies (at $0\times$MIC) exhibit the smallest $r/r_{\max}$ value, while the colonies treated with azithromycin demonstrate an increase in $r/r_{\max}$ values. Specifically, colonies treated with a moderate concentration of azithromycin (at $20\times$MIC) present an intermediate $r/r_{\max}$ value, while those treated with high concentrations (at $40, 100\times$MIC) demonstrate a further increase in $r/r_{\max}$ values.

Fig. 4.2(b) shows a recduction of the steady-state contact angles that correspond to larger spreading radii for increasing concentrations of azithromycin.

This observed trend suggests a dependent relationship between concentration of azithromycin and the magnitude of $r/r_{\max}$ and steady-state contact angle θ in treated bacterial colonies. It can be summarised that higher concentrations of azithromycin prompted colonies to exhibit greater wetting capacity.

It is noteworthy that bacterial colonies treated with azithromycin at $40, 100\times$MIC demonstrate comparable wetting capacity on the surface. This suggests that the wetting capacity of colonies on the surface does not escalate consistently with concentration of antibiotic, implying that there is a limit to this capacity.

Bacterial colonies spreading on surfaces are simulated using previously introduced models. The simulations initiate with the growth of a single bacterium above the surface, and the growth of the bacteria is stopped when the number of bacteria reaches N. This results in the formation of a bacterial colony consisting of a fixed number of bacteria. Once the colony growth is complete, a planar surface is created below the colony. The binding of the pili of the bacteria to the surface generates an interaction force which drives the colony to migrate towards the surface. The colony reaches a steady state when this spreading process is complete.

In the simulations, the adjustment of two parameters is employed to replicate colonies treated with varying concentrations of antibiotics. Experimental measurements have indicated that azithromycin-treated bacteria demonstrate a reduced probability of pilus binding. Consequently, the pilus binding rate k_{bind} is selected as the first parameter. The second parameter is the cell-cell DPD friction γ, a friction parameter that determines dissipation in non-equilibrium states. Since there is no net energy dissipation in equilibrium states, γ should not play a role for equilibrium configurations. However, somewhat surprisingly, we found that this parameter does affect the

steady-state contact angle for active bacterial colonies.

The steady-state contact angles of the simulated colonies are shown in Fig. 4.2(c). It can be observed that the steady-state contact angle increases with increasing pilus binding rate k_{bind} or cell-cell DPD friction γ. To align simulated results with experimental data for wild-type bacterial colonies, a specific set of parameters (dot 1: $k_{\mathrm{bind}} = 50\,\mathrm{s}^{-1}$, $\gamma = 240\,\mathrm{pN}\cdot\mathrm{s}/\mu\mathrm{m}$) is chosen. This choice aims to establish a correspondence between the steady-state contact angles of simulated and experimental colonies, ensuring that they are approximately equal. Based on this approach, three more sets of parameters (dots 2, 3 ,4) are selected, each corresponding to the bacterial colonies treated with three different concentrations (20, 40, 100×MIC) of azithromycin in the experiments. This systematic approach ensures the alignment of simulated parameters with the observed behaviors in antibiotic-treated bacterial colonies, facilitating a representation of varying antibiotic concentrations in the simulated model.

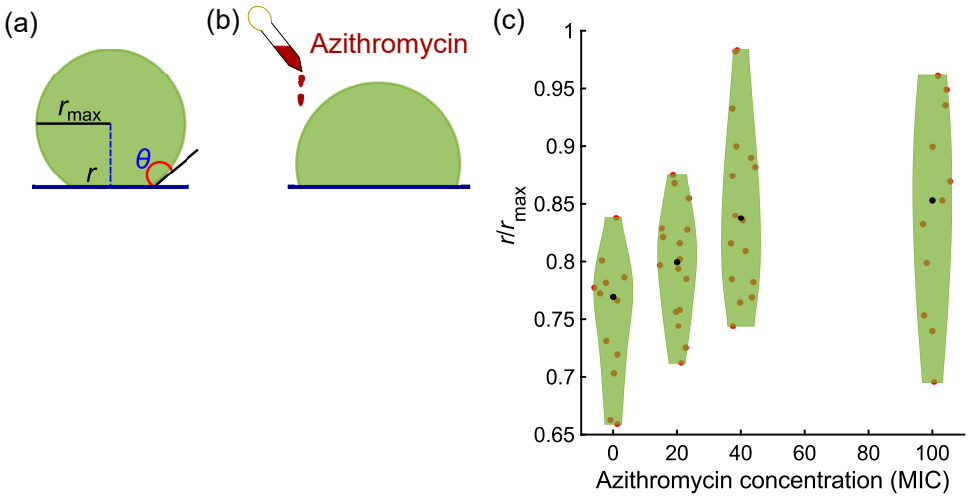

Figure 4.1: (a) Sketch of colonies wetting surfaces. The colony on the surface can be approximated as part of a sphere of radius r_{max}, and the area of contact with the surface is approximated as a circle of radius r, forming a contact angle θ. Left: a colony of wild type bacteria; right: a colony of azithromycin-treated bacteria. (b) The relative steady-state spreading radius r/r_{max} as a function of the azithromycin concentration in the experiments. The unit of x-axis is the MIC of azithromycin for *N. gonorrhoeae*.

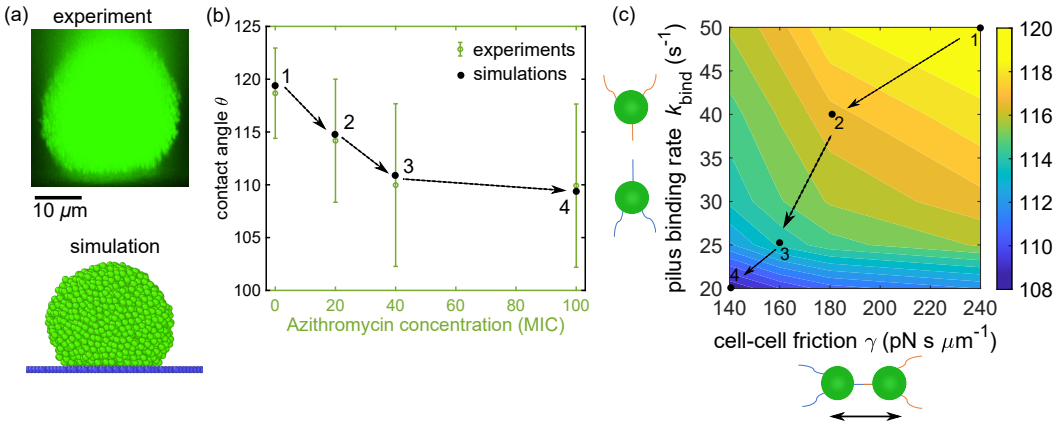

Figure 4.2: (a) Spreading bacterial colony imaged by confocal microscopy of fluorescently labeled cells (top), and an image of a simulated spreading colony (bottom). Scale bar: $10\,\mu$m. (b) Experimental (green) and simulated (black) variation of steady-state contact angle of colonies wetting surfaces with azithromycin concentration. The 1, 2, 3,4 dots in here correspond to these four dots in figure (c). (c) Steady-state contact angle of simulated colonies wetting on a surface. The steady-state contact angle as a function of the the two most important parameters (k_{bind}, γ). With increase of the azithromycin concentration, the contact angle moves to lower values.

4.3 Size dependence of the steady-state contact angle

Surface tension is defined as the ratio of the change in energy to the change in surface area

$$\sigma = \frac{\mathrm{d}E}{\mathrm{d}A}, \tag{4.1}$$

where E is the energy, and A is the surface area. Young's equation relates the equilibrium contact angle θ_e with the surface tensions as

$$\sigma \cos\theta_e = \sigma_{sv} - \sigma_{sl}, \tag{4.2}$$

where σ is the liquid-vapor surface tension, σ_{sv} is the solid-vapor surface tension, σ_{sl} is the solid-liquid surface tension, and θ_e is the stationary Young's angle.

For idealized liquids with an infinitely thin liquid-gas interface zone, the equilibrium contact angle does not depend on the size of the spreading droplet. Whether the Young's equation holds for active bacterial surface wetting is unclear. A variation of the contact angle with the size of the colony in experiments is shown in Fig. 4.3(a) with dots. We simulate colonies with different size spreading on surfaces, the spreading radius and the stationary contact

angles θ are shown in Fig. 4.3(a) with dashed lines. Evidently, for bacterial colonies, $\cos(\theta)$ depends approximately linearly on the inverse of the colony radius. We attribute this dependence to the finite interface. The slope of the linear relationship between the the inverse radius and $\cos(\theta)$ is the so-called Tolman length, which we estimate from the concentration profiles in simulations to be of the order of a few cell radii.

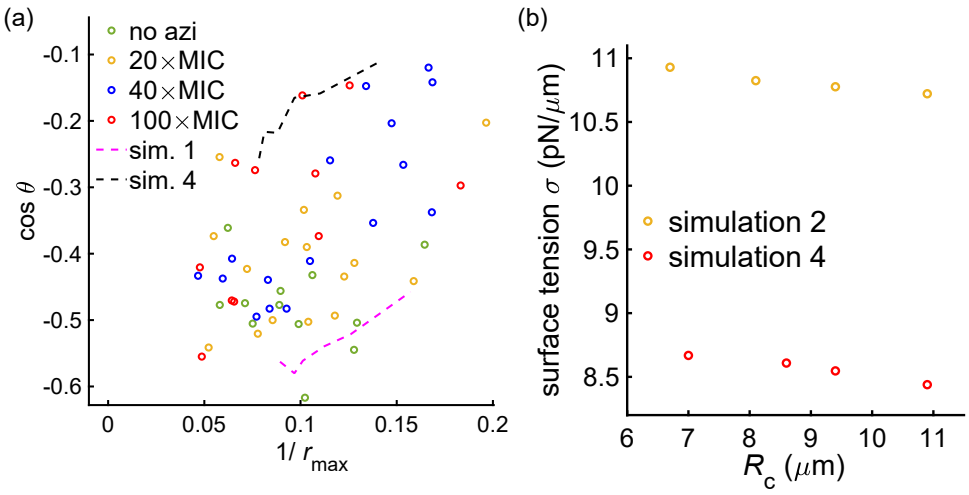

Figure 4.3: The steady-state contact angle and surface tension of colonies changes with the size of colonies which is quantified by the radius $r_{\max}$. (a) Cosine of the steady-state contact angle as a function of $1/r_{\max}$ under different azithromycin concentration in experimental data (dots) and simulations (dashed lines). (b) Surface tension σ as a function of radius of colonies R_c in simulations.

To characterise the size-dependent stationary contact angle, a modified Young's equation [188–191] has been proposed

$$\cos\theta_e = \cos\theta - \frac{\tau\sigma}{r}, \tag{4.3}$$

where τ is line tension at three phase contact line. The stationary contact angle θ of a droplet can only reach Young's angle θ_e if its spreading radius is infinite $r \to \infty$.

To verify the influence of line tension on the wetting behavior of active bacterial colonies on surfaces, cylindrical colonies of infinite length are simulated as shown in Fig. 4.4(a). Periodic boundary conditions (PRC) are applied along the axial direction of the cylindrical colonies, allowing them to be considered as effectively infinite in length. It has been demonstrated that the line tension of such cylindrical liquid structures is negligible when the contact angle exceeds 90 degrees $\theta > 90°$. For simulated colonies $\cos(\theta)$ as a

function of $1/r$ is shown in Fig. 4.4(b), revealing a noticeable influence of $1/r$ on the contact angle θ. Neglecting the effect of linear tension of cylindrical colonies on the contact angle, a size dependent surface tension is required. For spherical droplets the curvature dependent surface tension is given by

$$\sigma(R_{\mathrm{c}}) = \sigma_{\mathrm{flat}}(1 - \frac{2\delta_{\mathrm{T}}}{R_{\mathrm{c}}}), \tag{4.4}$$

where σ_{flat} is the surface tension of the flat interface, δ_{T} is the Tolman length. For cylindrical droplets the curvature dependent surface tension is given by

$$\sigma_{\mathrm{c}}(R_{\mathrm{c}}) = \sigma_{\mathrm{flat}}(1 - \frac{\delta_{\mathrm{T}}}{R_{\mathrm{c}}}). \tag{4.5}$$

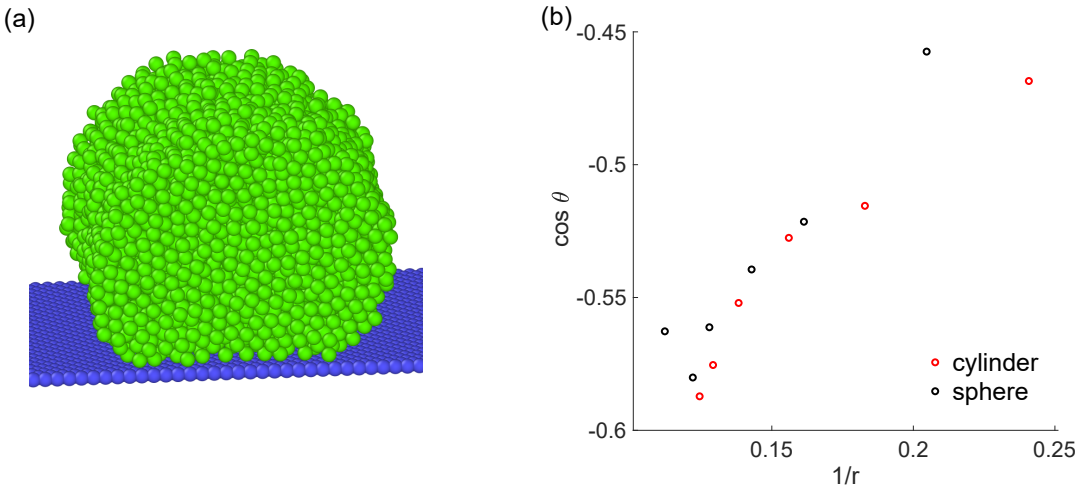

Figure 4.4: Steady-state contact angles for spherical and cylindrical colonies in simulations. (a) A simulation for cylindrical colonies wetting on a surface, PRC are applied along the axial direction of the cylindrical colonies. (b) The contact angle for surface wetting of spherical and cylindrical colonies as a function of curvature of colony.

The surface tension σ of simulated colonies is measured by micropipette aspiration, as shown in Fig. 4.5(a). The bacterial pili cannot bind to the simulated micropipette in here. A total driving force F_{d} is applied to all bacteria inside the micropipette, generating a pressure

$$P_{\mathrm{d}} = \frac{F_{\mathrm{d}}}{\pi R_{\mathrm{p}}^2}, \tag{4.6}$$

where R_{p} is the radius of the micropipette. If the pressure P_{d} exceeds the critical pressure to aspirate P_{c}, the bacterial colony will enter the micropipette

completely. Otherwise, it will not enter the micropipette. The critical pressure to aspirate P_c is given by the Laplace law

$$P_c = \frac{2\sigma}{R_p} - \frac{2\sigma}{R_c}, \tag{4.7}$$

where R_c is the radius of the colony. For different colony radii R_c , the critical pressures P_c are shown in Fig. 4.5(b). Therefore the corresponding surface tension σ can be calculated by Eq. 4.7, and the results are shown in Fig. 4.3(b).

We now consider the Tolman length effect, Eq. 4.7 can be modified as

$$P_c^T = \frac{2\sigma_{flat}(1 - \frac{\delta_T}{R_p})}{R_p} - \frac{2\sigma_{flat}(1 - \frac{2\delta_T}{R_c})}{R_c}. \tag{4.8}$$

The curves fitted to Tolman length-dependent critical pressures P_c^T are shown with dashed curves in Fig. 4.5(b). The fitted results are $\sigma_{flat} = 9.324$, $\delta_T = -0.1898$ for simulation 2, and $\sigma_{flat} = 6.652$, $\delta_T = -0.3447$ for simulation 4.

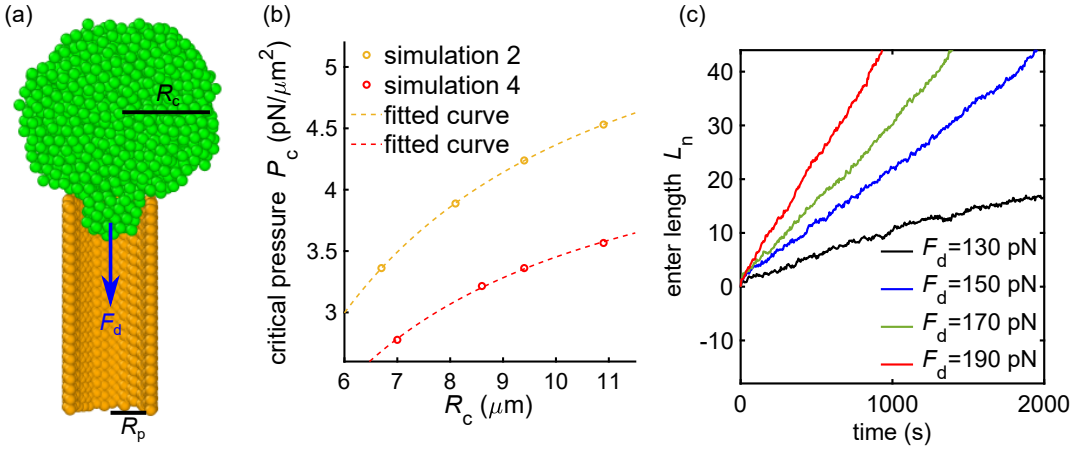

Figure 4.5: Micropipette aspiration of simulated colonies. (a) Snapshot of simulated colonies and micropipette aspiration. The bacteria colony with radius $R_c = 10.5\mu m$ is aspirated into a pipette with radius $R_p = 3.3\mu m$. (b) The critical pressure p_c as a function of colony radius R_c for simulation 2 and simulation 4. The curves fitted to Tolman length-dependent critical pressures P_c^T are shown with dashed curves. (c) The enter length L_n as a function of time for different driving forces F_d.

4.4 Slip length and shear viscosity

As mentioned above, the spreading dynamics of passive liquids depends strongly on the solid-liquid boundary condition. For no-slip boundary conditions, dissipation occurs mainly at the outer rim of the spreading droplet.

These small lengthscales involved lead to strong friction and a balance of capillary forces and frictional forces is results in a generic scaling prediction for the time-dependence of the radius, known as Tanner's law. If, however, the fluid is allowed to slip on the surface, dissipation is no longer localized to the edges and different spreading laws result. To understand the spreading dynamics of active bacterial colonies, we first investigate which boundary conditions would be appropriate for describing the flow of this material.

Couette flow and Poiseuille flow are two ways commonly used to measure the slip length [192]. Confining bacteria in two parallel smooth plates with a distance H, Couette flow is generated by moving only the upper plate at a constant velocity U, see Fig. 4.6(a). The slip length of bacteria on the plates is given by

$$L_{\mathrm{s}} = u_{\mathrm{s}}/\beta, \tag{4.9}$$

where u_{s} is the slip velocity, the shear rate $\beta = \partial u/\partial z$, u is the velocity profiles in x-direction. The shear stress in such flow is given by

$$\sigma_{\mathrm{s}} = F_x/A, \tag{4.10}$$

where the F_x is summation of the forces in x-direction on the upper wall, A is the area of the wall. The flow's shear viscosity can be calculated from

$$\eta = \sigma_{\mathrm{s}}/\beta. \tag{4.11}$$

The T4P of bacteria can bind to the surface, this binding produces attractive interactions among bacteria and surfaces. The active binding ($v_{\mathrm{wall}} = 1\mu m/s$) can generate a large slip length, on the contrary, the passive binding ($v_{\mathrm{wall}} = 0$), which the pili binding to the surfaces do not retract, only generates a small slip length as shown in Fig. 4.6(b).

Next, we asses whether fluid slip depends on a dependence of the viscosity on the shear rate. The corresponding shear viscosity and fitted lines in log-log plot are shown in Fig. 4.6(c). As we can see the shear viscosity depends on the shear rate as

$$\eta = k\beta^{n-1}, \tag{4.12}$$

where k is the consistency coefficient, n is the power exponent. For Newtonian fluids $n = 1$, for shear-thinning fluids $n < 1$, and for shear-thickening fluids $n > 1$. The power exponent $n \approx 0.78$ in our simulations means that the

colonies we simulated are shear-thinning liquids. During spreading, flow velocities are however very low and shear thinning therefore affects the process only weakly.

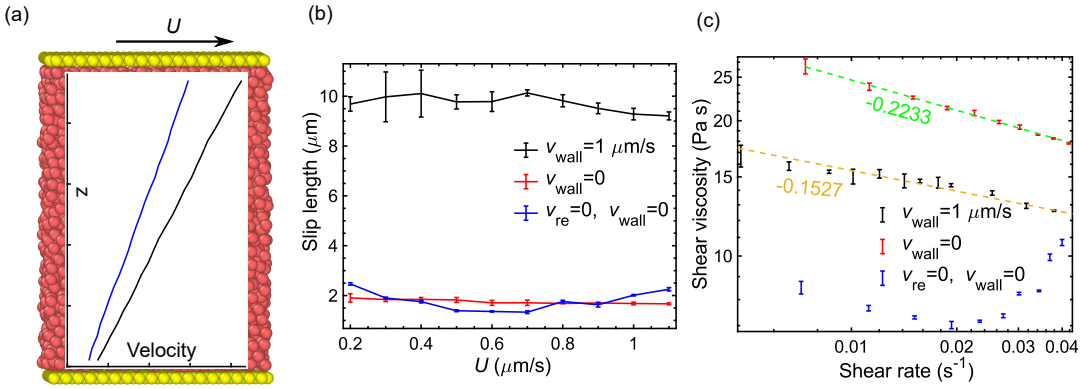

Figure 4.6: Measurement of slip length and shear viscosity of colonies.

4.5 Spreading dynamics

The steady state of colonies wetting surfaces has been studied in previous sections. However, further research is needed to explore the spreading process from the initial contact of the colony with the surface to the achievement of a steady state.

Experimental results for the variation of the spreading radius of wild-type and azithromycin-treated bacterial colonies over time are depicted in Fig. 4.7(b). The results indicate that wild-type bacterial colonies take longer time to reach the same spreading radius as azithromycin-treated bacterial colonies. Bacterial colonies treated with higher concentrations of azithromycin exhibit a more fast spreading on the surface. The spreading radius of the simulated colonies is shown in Fig. 4.7(c), the results demonstrate wetting behavior similar to that observed in experiments.

The exponent of the spreading radius r during the wetting of the colony on the surface is displayed in Fig. 4.7(d). For colonies treated with high concentrations ($40, 100\times$MIC) of azithromycin, the maximum value of the exponent of the spreading radius is approximately 0.38, whereas for untreated colonies, the maximum value of the exponent of the spreading radius is around 0.25. The azithromycin-treated colonies exhibit a larger exponent of the spreading radius. In the later stages of diffusion, the exponent of the diffusion radius gradually decreases to 0.

Azithromycin treatment not only decreases the steady-state contact angle but also accelerates spreading in colonies. Consequently, it can be inferred that the wetting behavior of the colonies on the surface is improved by azithromycin treatment.

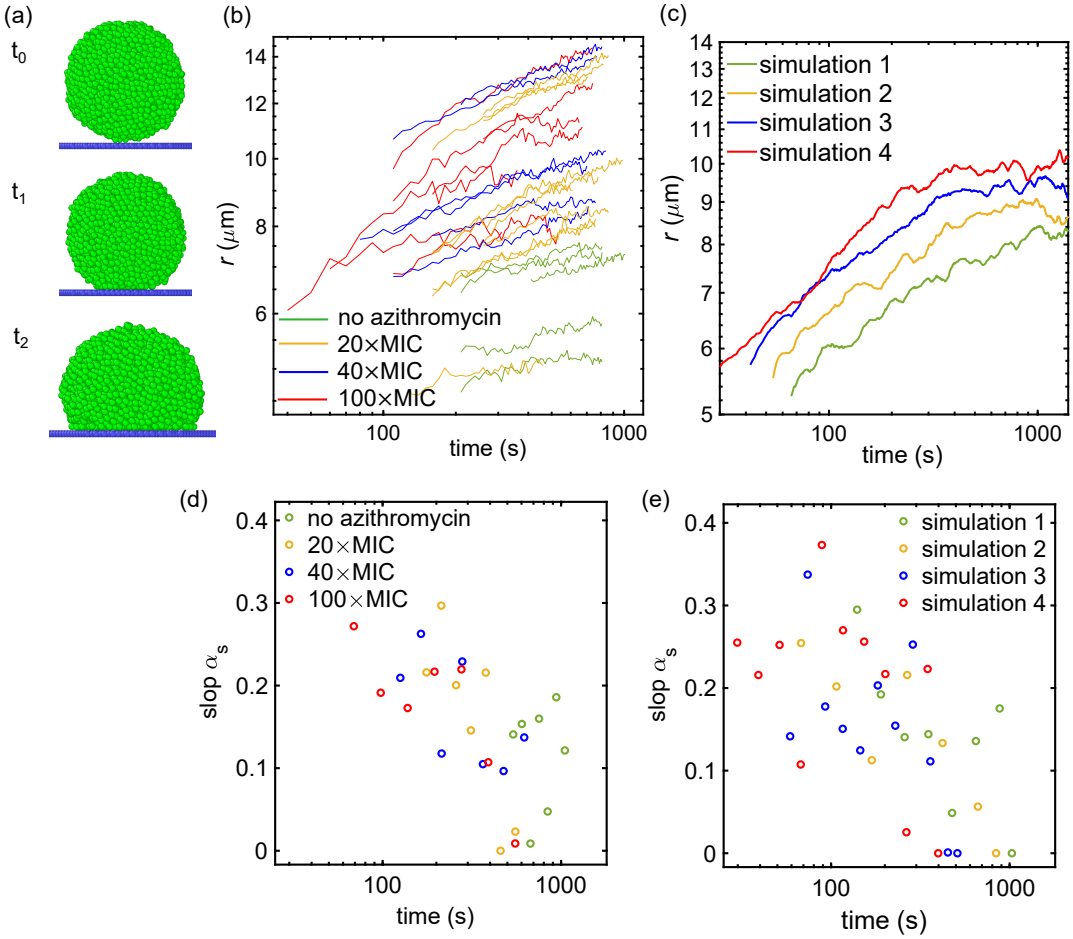

Figure 4.7: Spreading radius of bacterial colonies wetting on a surface. (a) Snapshots from a simulated spreading process for wild-type bacteria. (b) Spreading radius r of untreated bacterial colonies and bacterial colonies treated with different concentrations ($20, 40, 100\times$MIC) of azithromycin. (c) Spreading radius r of simulated colonies. (d) The exponent of the spreading radius r as a function of time.

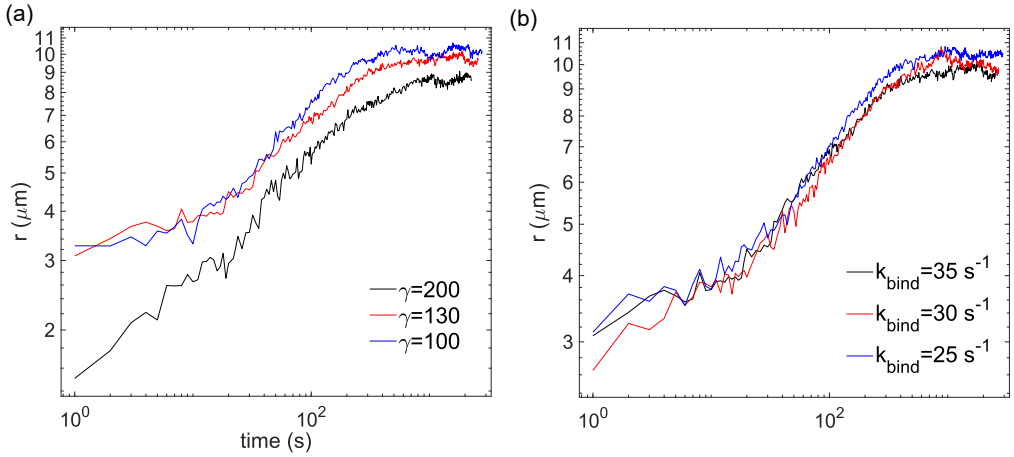

Figure 4.8: Spreading radius simulated with various parameters.

4.6 MSD and VACF of individual bacteria in colonies

Bacteria within the bulk of the colonies exhibit approximately the same number density everywhere, allowing the bulk of the colonies to be considered as homogeneous. Bacteria at distances greater than $3.5\,\mu$m from the colony surface $d_{\text{edge}} > 3.5\,\mu$m are regarded as part of the bulk as shown in Fig. 4.9(a). The MSD of bacteria in the bulk of the colony is calculated as

$$\text{MSD}(t) \equiv \frac{1}{M}\sum_{i=1}^{M} |\mathbf{r}_i(t) - \mathbf{r}_i(0)|^2, \tag{4.13}$$

where M is the number of bacteria in the bulk of the colony, and t is time.

The experimental measurements of the MSD of untreated and azithromycin-treated colonies are shown in Fig. 4.9(b). This experimental data was generated by Dr. M. Hennes in the laboratory of Prof. B. Maier at Cologne University. The MSD of bacteria in azithromycin-treated colonies is larger than that of bacteria in untreated colonies. We define a time-dependent exponent $\alpha(t)$ which serves to characterize the random walk of the bacteria and is related to the MSD as

$$\text{MSD}(t) \sim t^{\alpha(t)}. \tag{4.14}$$

The MSD exponent for a free Brownian particle tends to one ($\alpha(t) = 1$) over long time scales. If the exponent is less than one ($\alpha(t) < 1$), the particle is characterized as undergoing subdiffusion, and an exponent greater than one ($\alpha(t) > 1$) is characterized as superdiffusion. An exponent equal to two ($\alpha(t) = 2$) defines ballistic diffusion, e.g. particles moving in a fixed direction at a constant velocity. The exponent of the MSD for azithromycin-treated

bacterial colonies is shown in the inset of Fig. 4.9(b). For both untreated and azithromycin-treated bacterial colonies, the bacteria exhibit superdiffusion on small timescales ($0.01\mathrm{s} < t < 0.2\mathrm{s}$), and transition to subdiffusion on larger time scales ($1\,\mathrm{s} < t < 10\,\mathrm{s}$). It should be noted that here the colonies were treated with azithromycin for 5 hours, which differs from the experiment mentioned in the other sections, where the treatment with azithromycin lasted only for $0.5 - 1.0$ hours.

The MSD of the corresponding simulations is shown in Fig. 4.9(c), which shows that the MSD of the colony in simulation 1 is the smallest, while the MSD of the colony in simulation 4 is the largest. All simulated colonies show superdiffusion ($\alpha(t) < 1$) at the short-time range ($0.01\,\mathrm{s} < t < 0.2\,\mathrm{s}$), and simulation 1 clearly shows subdiffusion ($\alpha(t) > 1$) at long-time range ($1\,\mathrm{s} < t < 10\,\mathrm{s}$). This suggests that increasing the concentration of azithromycin in treated colonies decreases the MSD of bacteria in the bulk of the colony.

To characterize the long-term mobility of bacteria, the effective diffusion coefficient D is defined as

$$D \equiv \frac{\mathrm{MSD}(t)}{2d \cdot t}|_{t=1\mathrm{s}}, \tag{4.15}$$

where d is the number of dimensions. The effective diffusion coefficient D of simulated colonies as a function of distance from the colony surface d_{edge} is shown in Fig. 4.9(c). It can be summarized as increasing the concentration of azithromycin in treated colonies increases the diffusion coefficient of bacteria over long time. Furthermore, the effective diffusion coefficient D decreases with increasing the distance from the colony surface d_{edge}, eventually reaching an approximately stable value. This suggests that bacteria closer to the colony surface have a larger diffusion coefficient, while all bacteria in the bulk of the colony exhibit approximately the same diffusion coefficient.

The MSD of bacteria within the bulk of the colony has been simulated with variations in the parameters of pilus binding rate k_{bind} and cell-cell DPD friction coefficient γ, and the results are shown in Fig. 4.10. Increasing the pilus binding rate k_{bind} will decrease the exponent α of the MSD at the long-time range ($1\,\mathrm{s} < t < 10\,\mathrm{s}$). Increasing the cell-cell DPD friction coefficient γ reduces the MSD.

The experimental measurements of the VACF for untreated and azithromycin-treated colonies are shown in Fig. 4.12(a). Similar to the MSD measurement, the VACF is measured only for bacteria in the bulk of the colony. The azithromycin-treated colony exhibits a higher VACF at short times ($0.01\,\mathrm{s} <$

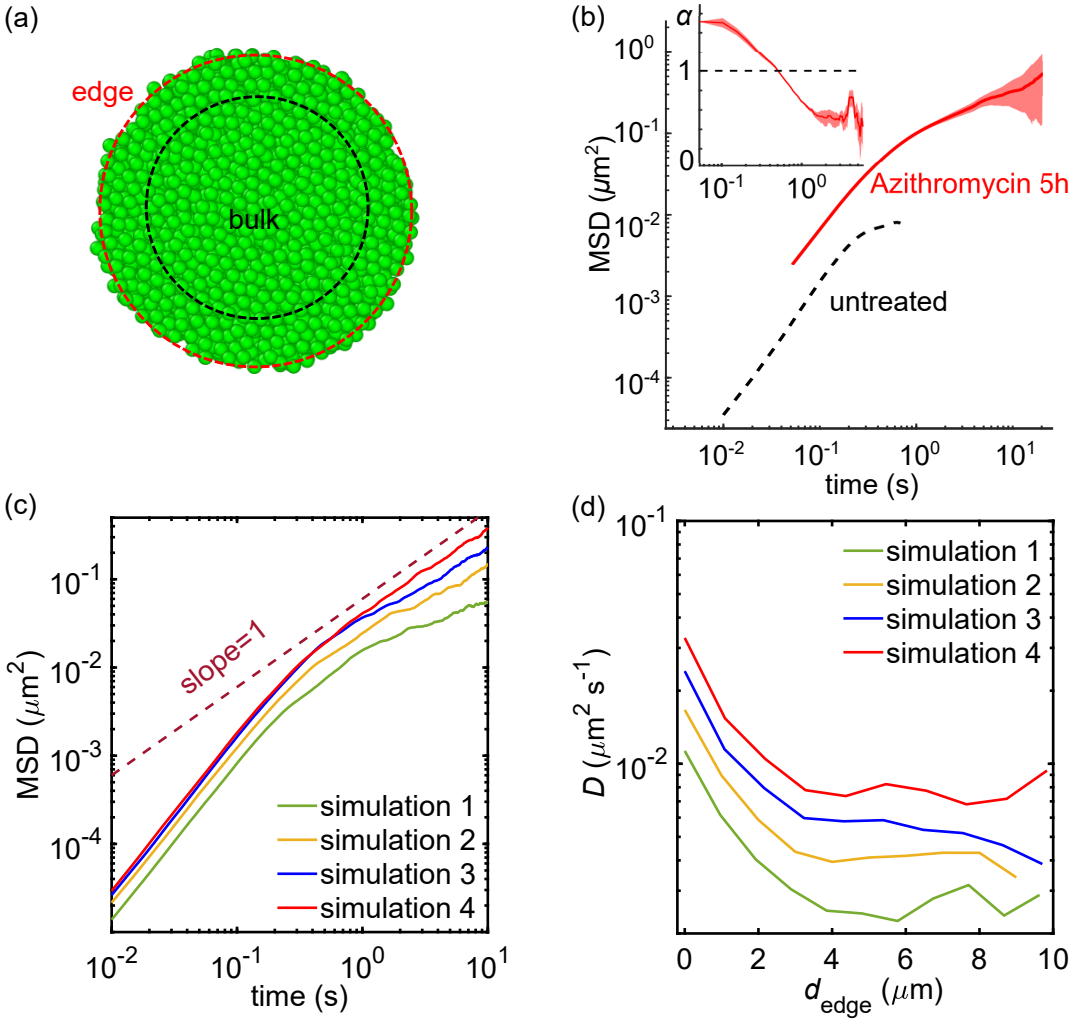

Figure 4.9: The MSD and the effective diffusion coefficient of the bacteria in the colonies. (a) A simulated bacterial colony, with surface and bulk labeling. (b) The experimental MSD of bacteria in the bulk of the colonies, both untreated and azithromycin-treated for 5 hours. (c) The MSD of bacteria in the bulk of the colonies for simulated colonies. As in Fig. 4.2, the parameter values for simulations 1-4 are chosen to represent increasing concentrations of azithromycin. (d) The effective diffusion coefficient D of simulated colonies as a function of distance from the colony surface d_{edge}.

$t < 0.2\,\mathrm{s}$). The relaxation times for both colonies are approximately 0.5 s. The VACF of the simulated colonies are displayed in Fig. 4.12(b). The results indicate an increase in VACF with increasing azithromycin concentration in the short-time range. Relaxation times (approximately 0.5 s) comparable to the experimental results have been obtained.

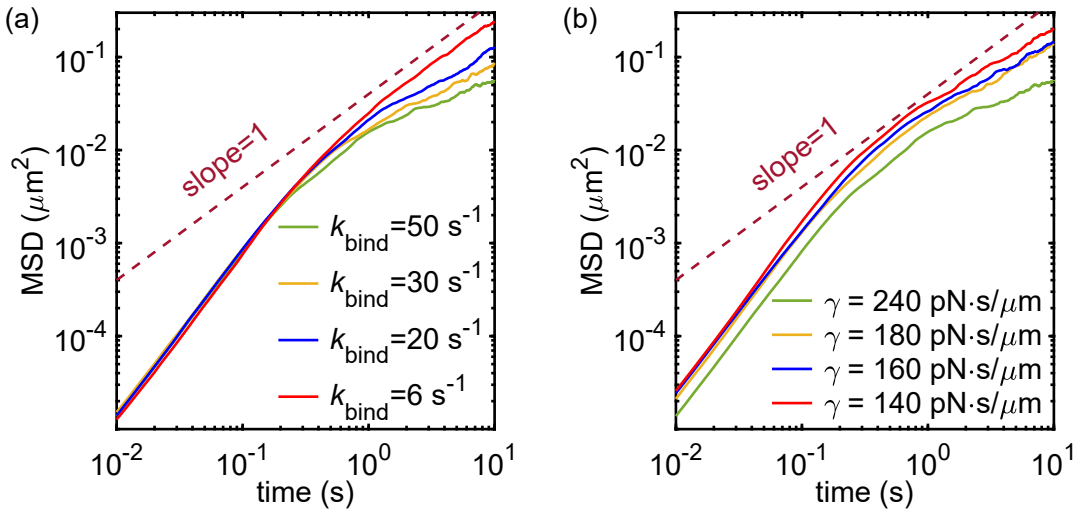

Figure 4.10: The MSD of bacteria in the bulk of the colonies for different simulation parameters: (a) pilus binding rate k_{bind} and (b) cell-cell DPD friction coefficient γ.

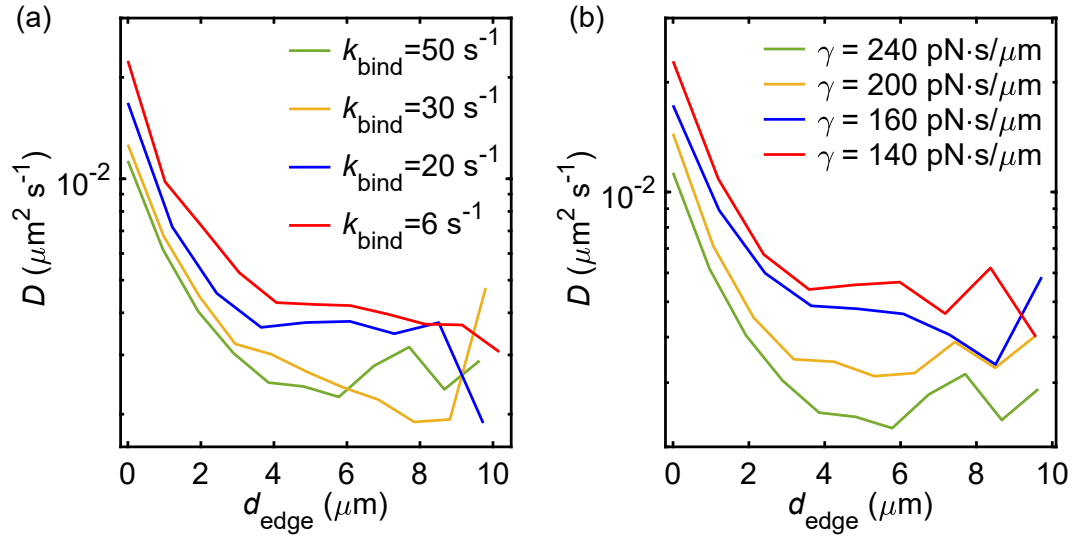

Figure 4.11: The effective diffusion coefficient D of the bacteria in the colonies for different simulation parameters: (a) pilus binding rate k_{bind} and (b) cell-cell DPD friction coefficient γ.

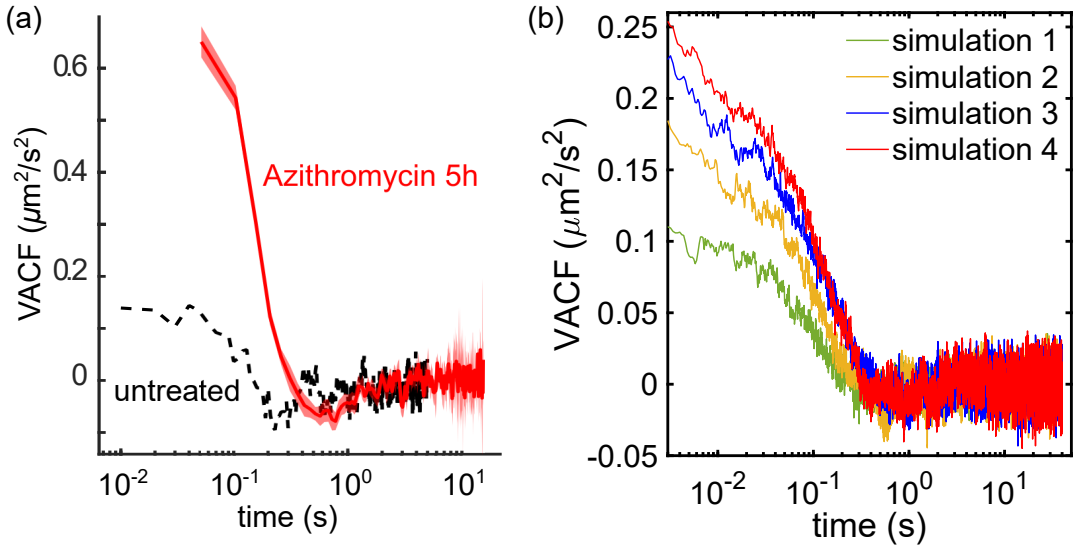

Figure 4.12: The VACF of bacteria in the bulk of the colonies. (a) The experimental measurements of the VACF of untreated and azithromycin-treated colonies. (b) The VACF of the simulated colonies.

4.7 Summary

Experiments investigating the wetting behavior of bacterial colonies on surfaces have been carried out in the laboratory of Prof. Dr. Berenike Maier at University of cologne. The results indicate that these colonies exhibit a large steady-state contact angles ($\theta > 90°$) on the surface. In addition, the experimental results on azithromycin-treated bacterial colonies highlight a significant influence of azithromycin treatment on the wetting behavior of the colonies. Specifically, it was observed that azithromycin treatment decreased the steady-state contact angle of the colonies, indicating an increase in the wetting capacity of the colonies. Furthermore, the wetting behavior of bacterial colonies treated with different concentrations of antibiotics has been investigated. The experimental results indicate that increasing the concentration of azithromycin increases the wetting capacity of the colonies. To gain deeper insight, we introduce a simulation model that includes individual bacteria and surfaces to study colony wetting behavior. The simulated colonies exhibit wetting behavior akin to that observed in experiments by choosing appropriate parameters. Notably, both experimental and simulation findings reveal a correlation between the steady-state contact angle and colony size. Specifically, the steady-state contact angles increase with colony size. In addition to analyzing the steady-state, we also investigate the dynamics of colony wetting. Findings from both experimental and simulation studies suggest that colonies treated with higher concentrations of azithromycin exhibit faster surface spreading, resulting in a greater spreading law. The effect of azithromycin treatment on the mobility of bacteria in the colonies has been investigated experimentally and in simulations. The results reveal that azithromycin treatment induces an increase in both the MSD and the diffusion coefficient of bacteria within the colonies.

4.8 Appendix

4.8.1 Parameters values

Parameters values that are used for the simulations in this chapter are listed in Tab. 4.1, parameters not listed here use the same values as in Tab. 2.1.

Table 4.1: The choice of parameters for the simulations in this chapter.

Parameter	Value	Unit
cell radius R	0.5	d_c
cell mass m	0.1	$f_\mathrm{c} t_\mathrm{c}^2 d_\mathrm{c}^{-1}$
pilus spring constant k	500	$f_\mathrm{c} d_\mathrm{c}^{-1}$
pilus stall force f_s	180	f_c
maximum retraction velocity of pili v_0	1.0	$d_\mathrm{c} t_\mathrm{c}^{-1}$
number of pili per cell	7	
simulation time step Δt	1×10^{-4}	t_c
pilus rupture rate k_rupt	0.5	t_c^{-1}
pilus binding cutoff distance d_bind	2.0	d_c
pilus binding rate k_bind	50	t_c^{-1}
pilus-pilus bond rupture force scale F_rupt	30	f_c
maximum conservative force a_0	2000	$f_\mathrm{c} d_\mathrm{c}^{-1}$
conservative force cutoff $d_\mathrm{con} = 2R$	1.0	d_c
diplococcus spring constant a_growth	2000	$f_\mathrm{c} d_\mathrm{c}^{-1}$
friction coefficient γ	240	$f_\mathrm{c} t_\mathrm{c} d_\mathrm{c}^{-1}$
thermal energy scale $k_\mathrm{B}T$	1×10^{-2}	$f_\mathrm{c} d_\mathrm{c}$
dissipative and random force cutoff d_dpd	1.7	d_c

Chapter 5

A folding instability in bacterial colonies

5.1 Introduction

Bacteria locate at the edge of a colony receive greater amounts of nutrients and oxygen in comparison to those located at the center. Experiments have shown that bacteria within colonies decrease pili activity in response to oxygen and nutrient depletion. Experimental and simulation studies have shown that the mixing bacteria with different pili interactions induces a sorting phenomenon. Specifically, bacteria characterized by stronger pili interactions tend to aggregate at the center of the colony, while those with weaker pili interactions disperse toward the edge of the colony. This spatial sorting suggests a correlation between the strength of pili interactions and the positioning of bacterial clusters within the colony. It has been experimentally observed that colony sorting occurs when the bacteria inside the colony are transformed into inactive bacteria, similar to the mixing of bacteria with different pilus interactions. Specifically, clusters of inactive bacteria undergo a relocation process from the interior of the colony to its surface, and eventually inactive bacteria surround the cluster of active bacteria. This spatial sorting signifies a discernible consequence of the transformation of bacterial activity states within the colony. The phenomenonof sorting was found to be sometimes accompanied by the occurrence of a large-scale instability that we term folding. Colony folding is a translocation of inactive bacterial clusters inside the colony on to the colony surface by folding the shells of active bacteria.

5.2 Folding during colony sorting

To simulate the transformation of bacteria inside the colony into inactive bacteria due to depletion of nutrients or oxygen, the bacteria in the center of the colony are altered into a variant with reduced activity of their pili, these inactive bacteria are referred to as inactive bacteria. This reduced pili activity is simulated in this study by decreasing the pilus binding rate k_{bind} and/or the retraction velocity v_{re} of the pilus.

To investigate the influence of the size of inactive bacterial clusters on the process of colony folding, different transition cluster radii are simulated as shown in Fig. 5.1. At the beginning of the simulations, all bacteria are active (green bacteria), with a total number of bacteria $N = 6000$ they aggregate into a colony with radius $R_{\mathrm{c}} \approx 11.0\,\mu$m as shown in Fig. 5.1(a). At a certain time t_0, active bacteria within a distance R_{i} from the center of mass of the colony transform into inactive bacteria (red bacteria). These inactive bacteria form a cluster with a radius of R_{i} at the center of the colony. Three colonies with different radii ($R_{\mathrm{i}} = 8.0, 6.5, 5.0\,\mu$m) of inactive bacterial clusters are simulated. Thereby, we aim to systematically analyze how variations in the size of inactive bacterial clusters contribute to the observed dynamics of colony restructuring.

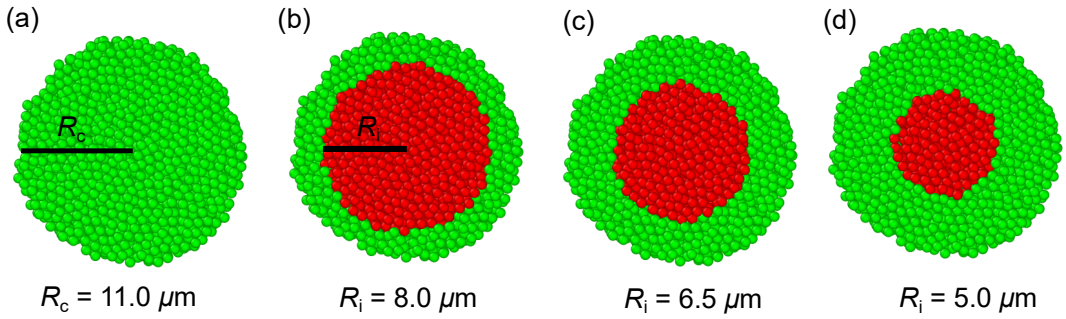

Figure 5.1: A cluster of inactive bacteria at the center of the colony. (a) Active bacteria (green) numbering 6000 aggregate into a colony with a radius of approximately $11\,\mu$m ($R_{\mathrm{c}} \approx 11.0\,\mu$m). Inactive bacteria form a cluster with a radius of $R_{\mathrm{i}} =$ (b) $8.0\,\mu$m, (c) $6.5\,\mu$m, (d) $5.0\,\mu$m, at the center of the colony.

Following the transformation of bacteria in the central region into inactive bacteria, the colony undergoes sorting. This sorting is driven by the fact that active bacteria near the colony edge exhibit stronger interaction forces between pili than inactive bacteria. The differential strength of pili-mediated interactions plays a critical role in the spatial organization of the colony, resulting in the observed sorting dynamics.

For active bacteria, their pili have a binding rate of $k_{\mathrm{bind}} = 50\,\mathrm{s}^{-1}$ and a retraction velocity of $v_{\mathrm{re}} = 2.0\,\mu\mathrm{m/s}$. The pili activity of inactive bacteria is reduced, and in this section, the parameters for inactive bacteria are chosen with a lower pilus binding rate of $k^{\mathrm{i}}_{\mathrm{bind}} = 5\,\mathrm{s}^{-1}$ and a lower pilus retraction velocity of $v^{\mathrm{i}}_{\mathrm{re}} = 0.6\,\mu\mathrm{m/s}$.

Simulations for the colony with an inactive cluster radius of $R_{\mathrm{i}} = 6.5\,\mu\mathrm{m}$ have been done, the sorting process of the colony is illustrated in Fig. 5.2(a). The active bacteria within a distance $R_{\mathrm{i}} = 6.5\,\mu\mathrm{m}$ from the center of mass of the colony transform into inactive bacteria at time t_0. Subsequently, at time t_1, the cluster of inactive bacteria establishes a channel leading to the colony surface, forming a depression on the colony surface. The colony begins to exhibit a rapid instability termed folding from this stage onward. An increasing number of inactive bacteria move through this channel to the colony surface, causing the channel to widen. Simultaneously, a large defect forms on the colony surface at time t_2. As most of the inactive bacteria migrate to the colony surface, the colony undergoes a distinct folding, assuming a hat-like shape rather than maintaining its spherical shape at time t_3. Eventually, almost all of the inactive bacteria migrate to the colony surface and distribute uniformly on the colony surface, while the active bacteria aggregate at the center of the colony, restoring the colony to a spherical shape at time t_4.

A colony with a smaller inactive bacterial cluster radius of $R_{\mathrm{i}} = 5.0\,\mu\mathrm{m}$ is simulated and diffusive sorting is observed as shown in Fig. 5.2(b). In contrast to the folding observing during the sorting process of the colony with $R_{\mathrm{i}} = 6.5\,\mu\mathrm{m}$, no folding is observed during the sorting process of the colony with $R_{\mathrm{i}} = 5.0\,\mu\mathrm{m}$. The inactive bacteria move individually to the surface of the colony, and they are no longer able to maintain a cluster. As the inactive bacterial cluster decreases in size, almost all of the inactive bacteria eventually drift to the surface of the colony. During this process, no defects are formed on the colony surface and the shape of the colony does not change significantly.

The colony with an inactive cluster radius of $R_{\mathrm{i}} = 7.0, 6.0, 5.5, 4.5, 3.5, 3.0\,\mu\mathrm{m}$ also have been simulated. The results can be summarized as follows: colony folding is observed for bacterial clusters with a radius $6.0\,\mu\mathrm{m} < R_{\mathrm{i}} < 8.0\,\mu\mathrm{m}$, while no folding is observed for colonies with $R_{\mathrm{i}} < 6.0\,\mu\mathrm{m}$. Therefore, it can be stated that the folding phenomenon during the sorting process of colonies depends on the size of the inactive bacterial cluster. When the radius of the inactive bacterial cluster is small, folding is hardly observable.

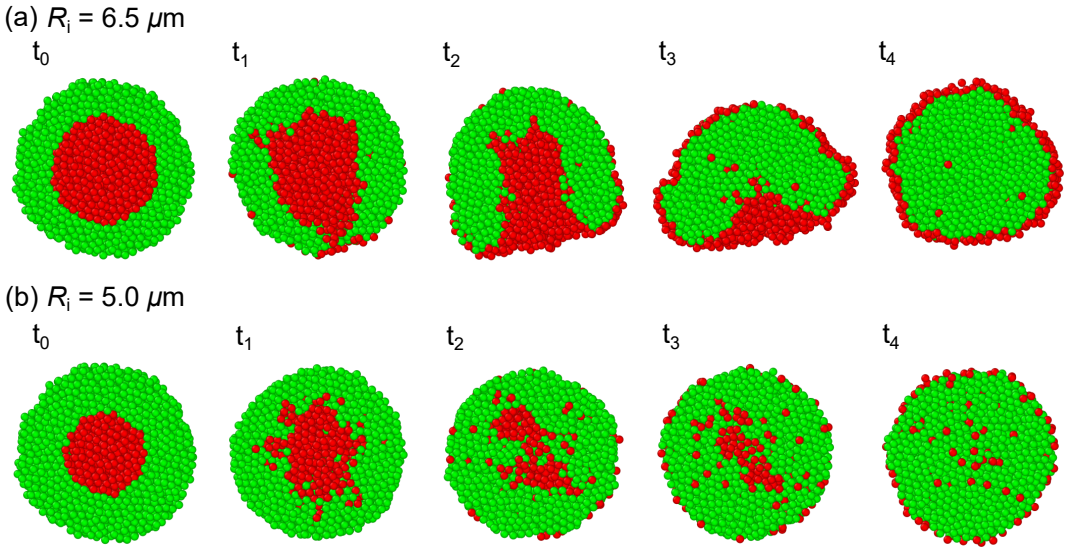

Figure 5.2: The process of colony sorting. For active bacteria (green), their pili have a binding rate of $k_{\mathrm{bind}} = 50\,\mathrm{s}^{-1}$ and a retraction velocity of $v_{\mathrm{re}} = 2.0\,\mu\mathrm{m/s}$. For inactive bacteria (red), their pili have a binding rate of $k^{\mathrm{i}}_{\mathrm{bind}} = 5\,\mathrm{s}^{-1}$ and a retraction velocity of $v^{\mathrm{i}}_{\mathrm{re}} = 0.6\,\mu\mathrm{m/s}$. (a) A colony with an inactive bacterial cluster radius of $R_{\mathrm{i}} = 6.5\,\mu$m. The active bacteria within a distance $R_{\mathrm{i}} = 6.5\,\mu$m from the center of mass of the colony transform into inactive bacteria at time t_0. At time t_1, the cluster of inactive bacteria establishes a channel leading to the colony surface, forming a depression on the colony surface. At time t_2, a wide channel to the surface of the colony is formed by the inactive bacterial cluster, and a large defect appears on the surface of the colony. Most of the inactive bacteria are on the surface of the colony, and the colony is folded into a shape resembling a hat at time t_3. At time t_4, almost all of the inactive bacteria distribute uniformly on the colony surface, while the active bacteria aggregate at the center of the colony, giving the colony exhibits a spherical shape. (b) A colony with an inactive bacterial cluster radius of $R_{\mathrm{i}} = 5.0\,\mu$m. The shape of the colony does not change significantly during this process.

5.3 Dependence of colony folding on pilus activity

To investigate the dependence of the colony folding phenomenon on the activity of inactive bacterial pili, colonies consisting of inactive bacteria with different pilus binding rate $k^{\mathrm{i}}_{\mathrm{bind}}$ and pilus retraction velocity $v^{\mathrm{i}}_{\mathrm{re}}$ are simulated.

For colonies with a inactive bacterial cluster radius of $R_{\mathrm{i}} = 6.5\,\mu$m, the results can be classified into three categories: folding, no folding, and weak folding, as illustrated in Fig. 5.3(a). It can be observed that the occurrence of colony folding is highly dependent on the pilus binding rate of inactive bacteria. A

lower pilus binding rate of inactive bacteria ($k^{\mathrm{i}}_{\mathrm{bind}} \leqslant 5\,\mathrm{s}^{-1}$) is more prone to induce the folding phenomenon.

At relatively high pilus binding rates ($k^{\mathrm{i}}_{\mathrm{bind}} > 5\,\mathrm{s}^{-1}$), inactive bacteria are observed to migrate to the colony surface without inducing colony folding, as shown in Fig. 5.4. The process of colony sorting without folding is similar to the sorting process described in the previous section for smaller inactive bacterial clusters (e.g., $R_{\mathrm{i}} = 5.0\,\mu$m, see Fig. 5.2(b)).

In comparison to the typical folding phenomenon, a weak folding is observed in a colony, as shown in Fig. 5.5. Unlike regular folding, this weak folding dose not induce significant changes in the overall shape of the colony. Instead, inactive bacterial clusters form only a small depression on the surface of the colony.

Analogous simulations are performed for colonies with a inactive bacterial cluster radius of $R_{\mathrm{i}} = 8.0\,\mu$m, and the results are presented in Fig. 5.3(b). The results indicate a similar dependence as observed for colonies with $R_{\mathrm{i}} = 6.5\,\mu$m, except that the weak folding phenomenon is not observed in this case.

The results from colonies with inactive bacterial cluster radii of $R_{\mathrm{i}} = 6.5$ and $8.0\,\mu$m both indicate a strong dependence of the folding phenomenon on the pilus binding rate $k^{\mathrm{i}}_{\mathrm{bind}}$ of the inactive bacteria, while the pilus retraction velocity $v^{\mathrm{i}}_{\mathrm{re}}$ of the inactive bacterial does not have a significant effect on folding.

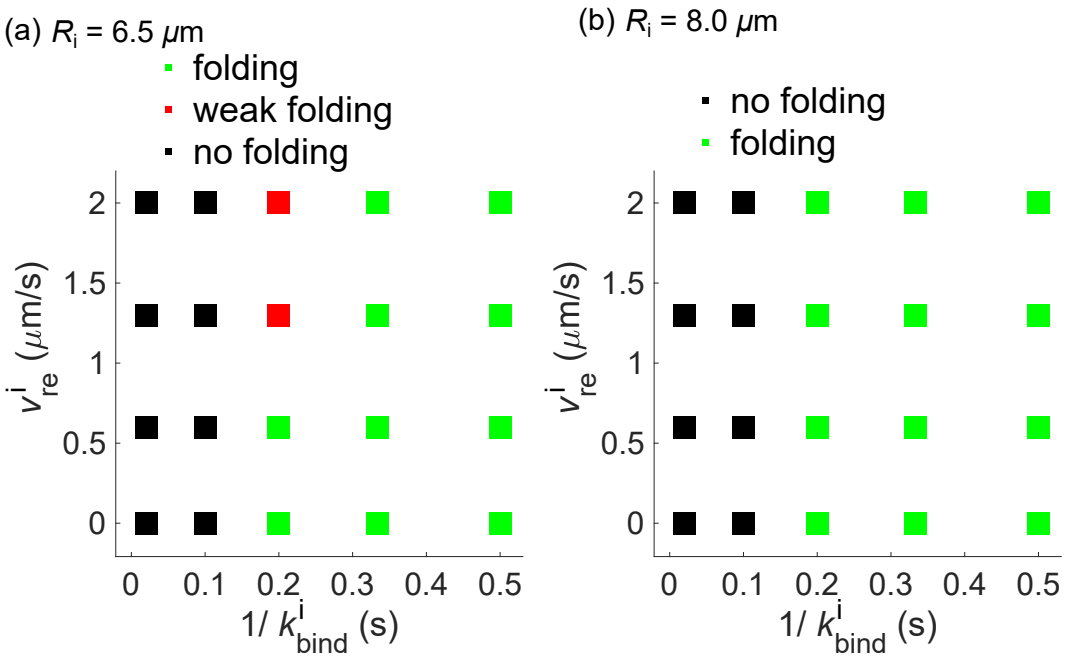

Figure 5.3: The dependence of colony folding on the pilus binding rate $k^{\mathrm{i}}_{\mathrm{bind}}$ and pilus retraction velocity $v^{\mathrm{i}}_{\mathrm{re}}$ of inactive bacteria. For active bacteria, the pilus binding rate of $k_{\mathrm{bind}} = 50\,\mathrm{s}^{-1}$ and pilus retraction velocity of $v_{\mathrm{re}} = 2.0\,\mu\mathrm{m/s}$ are fixed. (a) Folding phenomenon of colonies with a inactive bacterial cluster radius of $R_{\mathrm{i}} = 6.5\,\mu$m. Three different morphologies can be displayed during colony sorting: folding (green), weak folding (red), no folding (black). (b) Folding phenomenon of colonies with a inactive bacterial cluster radius of $R_{\mathrm{i}} = 8.0\,\mu$m.

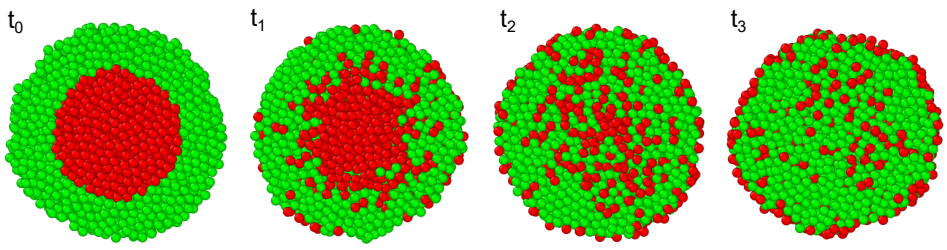

Figure 5.4: Colony sorting process without folding. A simulated colony with an inactive bacterial cluster radius of $R_{\mathrm{i}} = 6.5\,\mu$m. For active bacteria (green), their pili have a binding rate of $k_{\mathrm{bind}} = 50\,\mathrm{s}^{-1}$ and a retraction velocity of $v_{\mathrm{re}} = 2.0\,\mu\mathrm{m/s}$. For inactive bacteria (red), their pili have a binding rate of $k^{\mathrm{i}}_{\mathrm{bind}} = 10\,\mathrm{s}^{-1}$ and a retraction velocity of $v^{\mathrm{i}}_{\mathrm{re}} = 0.6\,\mu\mathrm{m/s}$. Inactive bacteria at the center the colony individually drift to the surface of the colony, and no folding phenomenon occurs.

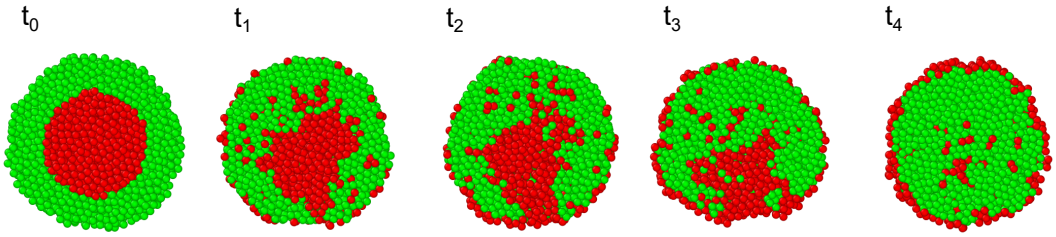

Figure 5.5: Weak folding during colony sorting. A simulated colony with an inactive bacterial cluster radius of $R_{\mathrm{i}} = 6.5\,\mu\mathrm{m/s}$, and the pilus binding rate $k^{\mathrm{i}}_{\mathrm{bind}} = 5\,\mathrm{s}^{-1}$ and pilus retraction velocity $v^{\mathrm{i}}_{\mathrm{re}} = 2.0\mu\mathrm{m/s}$ of inactive bacteria. The colony weakly fold during sorting and does not undergo major deformation.

5.4 Transport speed during colony folding

During colony folding, clusters of inactive bacteria are transported to the surface of the colony along the channels they form, as shown the blue arrows in Fig. 5.6. Inactive bacteria that have reached the surface of the colony walk randomly along the surface of the active bacteria.

To investigate the transport speed of inactive bacterial clusters to the colony surface during colony folding, inactive bacteria within a distance of R_{d} from the center of mass of the colony are traced, as shown the black dashed line in Fig. 5.6. The transport speed $v_{\mathrm{tr}}(t)$ of inactive bacterial clusters is defined as

$$v_{\mathrm{tr}}(t) \equiv \frac{1}{\Delta_{\mathrm{tr}}} \left| \sum_{i=1}^{I} (\mathbf{r}_i(t + \Delta_{\mathrm{tr}}) - \mathbf{r}_i(t)) \right|, \tag{5.1}$$

where I is inactive bacteria within a distance of $R_{\mathrm{d}} = 4.5\,\mu\mathrm{m}$ from the center of mass of the colony, Δ_{tr} is the time interval for tracking the inactive bacteria.

The parameters for inactive bacteria are chosen with a pilus binding rate of $k^{\mathrm{i}}_{\mathrm{bind}} = 5\,\mathrm{s}^{-1}$ and a pilus retraction velocity of $v^{\mathrm{i}}_{\mathrm{re}} = 0.6\,\mu\mathrm{m/s}$. For the colony with a inactive bacterial cluster radius of $R_{\mathrm{i}} = 6.5\,\mu\mathrm{m}$, the transport speed $v_{\mathrm{tr}}(t)$ of the inactive bacterial cluster is shown in Fig. 5.7(a). The time $= 0\,\mathrm{s}$ corresponds to the moment of transition of the bacteria t_0 in Fig. 5.2(a). The moment t_1, when the colony starts to fold, and the moment t_3, when the colony is folded into the shape of a hat, are marked with red dashed lines in the figure. It can be observed that the transport speed $v_{\mathrm{tr}}(t)$ of the inactive bacterial cluster is greater between the moments t_1 and t_3 compared to speeds at other times.

The colony with a inactive bacterial cluster radius of $R_{\mathrm{i}} = 8.0\,\mu\mathrm{m}$ is simulated, the result is shown in Fig. 5.7(b). It can be observed that between the moments t_1 and t_3, the transport speed $v_{\mathrm{tr}}(t)$ of the inactive bacterial cluster is faster compared to colonies with $R_{\mathrm{i}} = 6.5\,\mu\mathrm{m}$.

An average transportation speed v_{ave} between the moments t_1 and t_3 is calculated. For the colony with a inactive bacterial cluster radius of $R_{\mathrm{i}} = 8.0\,\mu\mathrm{m}$, $v_{\mathrm{ave}} = 0.02\mu\mathrm{m/s}$, and for the colony with a inactive bacterial cluster radius of $R_{\mathrm{i}} = 6.5\,\mu\mathrm{m}$, $v_{\mathrm{ave}} = 0.0151\mu\mathrm{m/s}$.

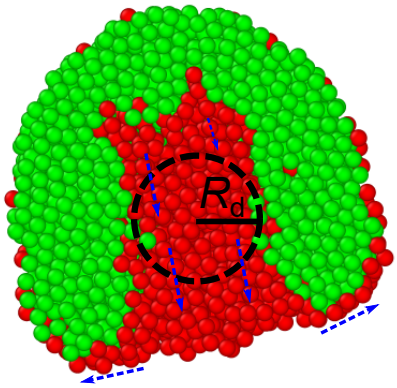

Figure 5.6: Inactive bacteria are transported to the surface of the colony along the channel they form during colony folding. Inactive bacteria within a distance of R_d from the center of mass of the colony (black dashed line) are traced.

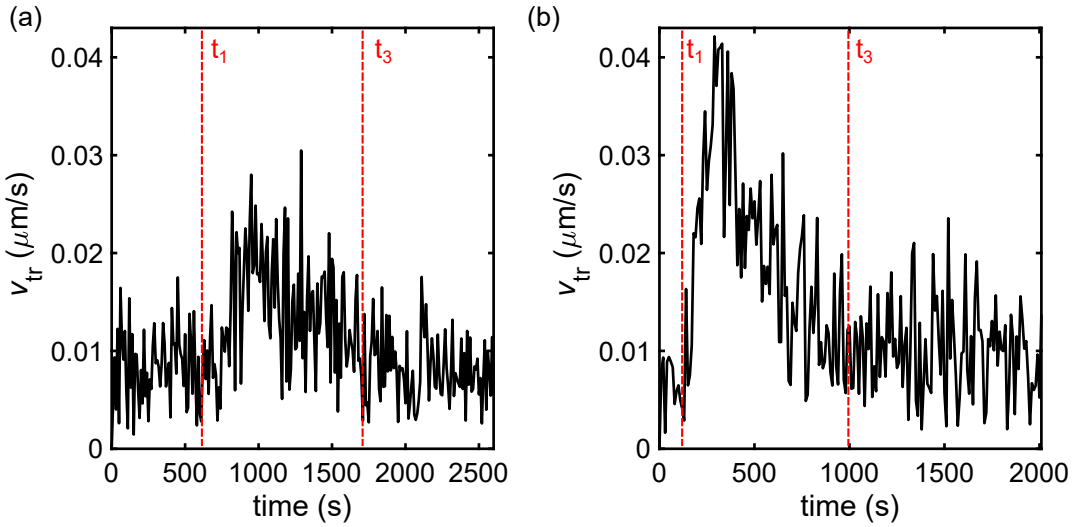

Figure 5.7: The transport speed $v_\mathrm{tr}(t)$ of the inactive bacterial cluster for The colony with a inactive bacterial cluster radius of (a)$R_\mathrm{i} = 6.5\,\mu$m and (b)$R_\mathrm{i} = 8.0\,\mu$m.

5.5 Summary

Over time, bacteria at the center of a colony experience a decline in pili activity attributable to the depletion of nutrients or oxygen. Consequently, such colonies undergo sorting, which is sometimes accompanied by the folding phenomenon. To study colony folding, simulations are performed with colonies containing inactive bacteria. By choosing appropriate parameters for the inactive bacteria, the colony folding phenomenon is reproduced in simulations. Our investigation reveals that the size of inactive clusters has a

significant impact on the folding dynamics of the colony. In particular, folding is observed for colonies with relatively large radii of inactive bacterial clusters ($6.0\,\mu\mathrm{m} < R_\mathrm{i} < 8.0\,\mu\mathrm{m}$) , while no folding is observed for colonies with smaller cluster radii $R_\mathrm{i} < 6.0\,\mu\mathrm{m}$. Further investigation of the dependence of colony folding on parameters related to inactive bacteria reveals that the pilus binding rate plays a significant role in colony folding. In particular, the lower the pilus binding rate of inactive bacteria, the more likely folding is observed. Conversely, the pilus retraction velocity has a negligible effect. The transport velocity of inactive bacteria during the colony folding process is investigated, and results show that colonies with larger clusters ($R_\mathrm{i} = 8.0\,\mu\mathrm{m}$) of inactive bacteria have faster transport speeds.

5.6 Appendix

5.6.1 Parameters values

Parameters values that are used for the simulations in this chapter are listed in Tab. 5.1, parameters not listed here use the same values as in Tab. 2.1.

Table 5.1: The choice of parameters for the simulations in this chapter.

Parameter	Value	Unit
cell radius R	0.5	d_c
cell mass m	0.1	$f_\mathrm{c} t_\mathrm{c}^2 d_\mathrm{c}^{-1}$
pilus spring constant k	500	$f_\mathrm{c} d_\mathrm{c}^{-1}$
pilus stall force f_s	180	f_c
maximum retraction velocity of pili v_0	2.0	$d_\mathrm{c} t_\mathrm{c}^{-1}$
number of pili per cell	7	
simulation time step Δt	1×10^{-4}	t_c
pilus rupture rate k_rupt	0.5	t_c^{-1}
pilus binding cutoff distance d_bind	2.0	d_c
pilus binding rate k_bind	50	t_c^{-1}
pilus-pilus bond rupture force scale F_rupt	60.0	f_c
maximum conservative force a_0	2000	$f_\mathrm{c} d_\mathrm{c}^{-1}$
conservative force cutoff $d_\mathrm{con} = 2R$	1.0	d_c
diplococcus spring constant a_growth	2000	$f_\mathrm{c} d_\mathrm{c}^{-1}$
friction coefficient γ	300	$f_\mathrm{c} t_\mathrm{c} d_\mathrm{c}^{-1}$
thermal energy scale $k_\mathrm{B}T$	2×10^{-2}	$f_\mathrm{c} d_\mathrm{c}$
dissipative and random force cutoff d_dpd	1.7	d_c

Chapter 6

Directed migration of bacterial colonies on sawtooth patterns

6.1 Introduction

A droplet of water can undergo directed motion on a serrated surface under non-equilibrium conditions. Cells perform directional migration on geometrically asymmetric ratchets [193–195], on which droplets can directionally move [196, 197]. When cells move in a random walk through asymmetric channels they can generate a net transport in one direction [4, 26, 198, 199].

Here, we propose that bacterial colonies may be able to directionally migrate on geometrically asymmetric surfaces. Unlike cells and droplets, the migration of colonies on geometrically asymmetric surfaces is driven by the bacterial pili binding to the surfaces. Pili can result in unbalanced active forces on the colony by binding to asymmetric ratchets. The unbalanced forces in the horizontal direction drive the colony forward. The shape of the ratchets affects pili binding, therefore we propose that the direction of migration can be controlled by changing the geometry of the ratchets. In addition to the sawtooth surfaces, the inherent properties of the bacterial colony may also potentially influence the directional migration of the colony.

6.2 Description of sawtooth patterns

Each sawtooth pattern is composed of many identical right-angled triangles, where the width of these triangles is l, and the height is g, as shown in Fig. 6.1. Thus, the difference between the sawtooth patterns is determined only by the width l and height g of the small right triangles that make them up. The

width of the pattern is W_{p} and its total length L_{p} is given by

$$L_{\mathrm{p}} = N_{\mathrm{p}} l, \tag{6.1}$$

where N_{p} is the number of small right-angled triangles constituting the pattern. In our simulations, periodic boundary conditions are employed, allowing the length and width of the pattern to be considered infinite ($L_{\mathrm{p}} \to \infty, W_{\mathrm{p}} \to \infty$).

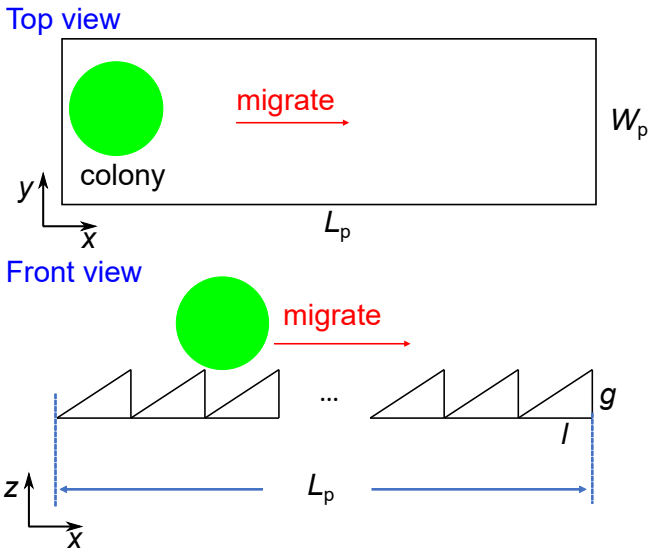

Figure 6.1: Sketch of the sawtooth pattens. The sawtooth patterns are made up of many small identical rectangular triangles arranged in close proximity. These small triangles have a width of l and a height of g, forming a pattern with a length of L_{p} and a width of W_{p}. The colony migrates along the direction of the length of the pattern, which is defined as the x-axis. In this figure it is assumed that colonies migrate along the positive x-axis direction (to the right).

Various different patterns have been designed, and three typical patterns are displayed in Fig. 6.2. The width l and height g of the small rectangular triangles that make up each of these three patterns (pattern 1: $l = 1.4\,\mu\mathrm{m}$, $g = 1.0\,\mu\mathrm{m}$; pattern 2: $l = 2.71\,\mu\mathrm{m}$, $g = 1.18\,\mu\mathrm{m}$; pattern 3: $l = 1.38\,\mu\mathrm{m}$, $g = 0.89\,\mu\mathrm{m}$) are shown in the up of the figure. In the simulations, each hypotenuse and height of the rectangular triangles are formed by many small fixed particles (blue), as depicted in the down of Fig. 6.2. Periodic Boundary Conditions (PBC) are used in the simulations, so these simulated patterns are equivalent to being composed of an infinite number of small rectangular triangles.

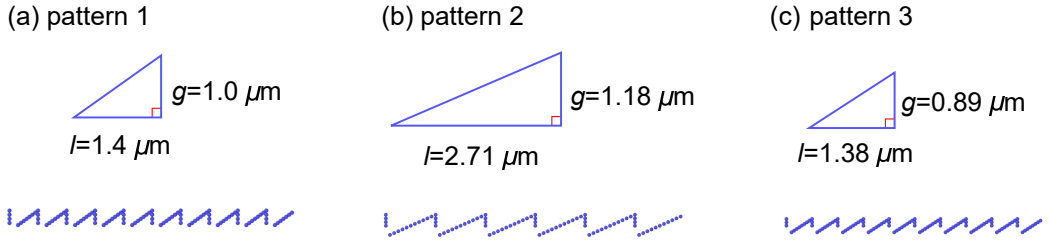

Figure 6.2: Three designed sawtooth patterns. Up: the structures of three small right triangles; down: simulated patterns are formed by many small fixed particles (blue). In the simulations PBC is used, so the patterns can be considered as consisting of an infinite number of small right triangles.

The simulations are initiated with the growth of a single bacterium above the pattern, as shown in Fig. 6.3(a). As the number of bacteria increases, they aggregate into a microcolony, see Fig. 6.3(b). The growth of the bacteria is stopped when the number of bacteria reaches $N = 400$, and the pili of bacteria bind to the pattern, causing the colony to adhere to the pattern, as shown in Fig. 6.3(c). Bacterial growth is stopped to eliminate the influence of growth on the migration of the colony on the surface.

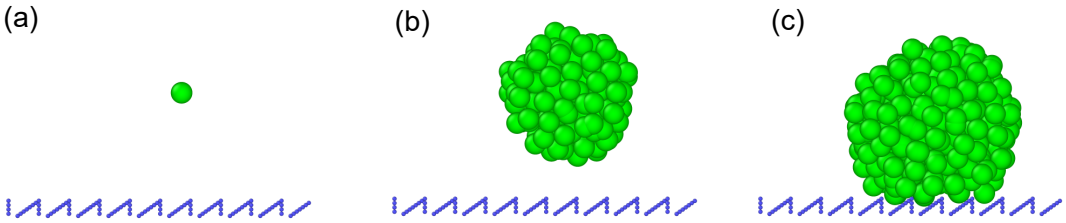

Figure 6.3: Bacteria growing into a colony on the patterns. (a) A single bacterium (green) above the pattern (blue). (b) Bacteria aggregate into a colony. (c) The colony with the number of bacteria $N = 400$ adheres to the pattern.

6.3 Migration speed of colonies on the patterns

To quantitatively study the migration of bacterial colonies on the patterns, some parameters relevant to bacteria are chosen. The number of bacteria in the colony is chosen as $N = 400$, the binding distance of the bacterial pili is set to $d_{\mathrm{bind}} = 1.8\,\mu\mathrm{m}$, and the retraction velocity of the pili binding to the patterns is chosen as $v_{\mathrm{p}} = 1.0\,\mu\mathrm{m/s}$. Such a colony adhering to different patterns exhibits markedly different migration behaviors. Specifically, the colony on pattern 1 migrates to the right (positive x-axis direction), as shown in Fig. 6.4(a), while the colony on pattern 2 migrates to the left (negative x-axis direction), as displayed in Fig. 6.4(b).

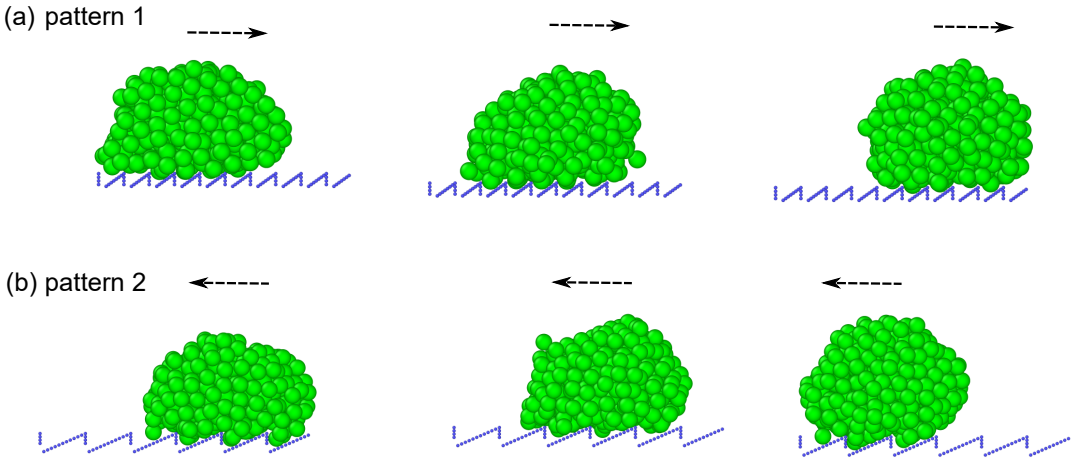

Figure 6.4: Snapshots of colonies migrating on the patterns. (a) The colony with the number of bacteria $N = 400$ migrates to the right on pattern 1. (b) The colony migrates to the right on pattern 2.

To characterize the migration direction and speed of bacterial colonies on the patterns, the displacement $d_{\mathrm{m}}(t)$ of the mass center of the colonies in the x-direction is defined as

$$d_{\mathrm{m}}(t) = \sum_{i=1}^{N}(x_i(t) - x_i(0)), \tag{6.2}$$

where N is the number of bacteria, x_i is the x-coordinate of the bacteria with index i.

The displacement $d_{\mathrm{m}}(t)$ of colony migration on these three patterns as a function of time are shown in Fig. 6.5. It is evident that on pattern 1 and pattern 3 the colony migrates along the positive x-axis (to the right), while on pattern 2 the colony migrates along the negative x-axis (to the left). The displacement of the colony on the patterns as a function of time exhibits an approximately linear relationship, indicating that the colony moves uniformly along the x-axis on the patterns. Therefore, the average migration speed s_{m} of colonies on the patterns can be defined as

$$s_{\mathrm{m}} = \frac{d_{\mathrm{m}}(t)}{t}|_{t\to\infty}. \tag{6.3}$$

The migration speed of the colony on pattern 1 ($s_{\mathrm{m}} = 0.0436\,\mu\mathrm{m/s}$) is greater than that on pattern 2 ($s_{\mathrm{m}} = 0.0076\,\mu\mathrm{m/s}$), while on pattern 3, the migration speed ($s_{\mathrm{m}} = -0.0308\,\mu\mathrm{m/s}$) is negative, as shown in Fig. 6.5.

To investigate the effect of colony size on the migration behavior of the colony

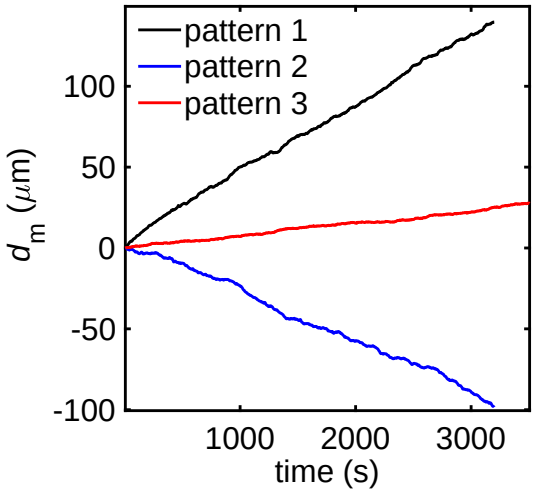

Figure 6.5: The displacement $d_{\mathrm{m}}(t)$ of the mass center of colonies as a function of time during the migration on the patterns.

on the patterns, colonies with a larger number of bacteria ($N = 1000$) are simulated. The migration of these colonies on pattern 1 and pattern 2 is shown in Fig. 6.6(a) and (b), respectively, and the displacement of the colonies as a function of time is plotted in Fig. 6.6(c). It is evident that larger colonies ($s_{\mathrm{m}} = 0.0436\,\mu\mathrm{m/s}$) on pattern 1 migrate significantly slower than smaller colonies ($s_{\mathrm{m}} = 0.0251\,\mu\mathrm{m/s}$) . On pattern 2, larger colonies ($s_{\mathrm{m}} = -0.0308\,\mu\mathrm{m/s}$) exhibit slightly faster migration compared to smaller colonies ($s_{\mathrm{m}} = -0.0316\,\mu\mathrm{m/s}$). These results suggest that the size of the colony can influence the migration speed of the colonies on the patterns.

To investigate the dependence of colony migration on the bacterial pilus binding distance, colonies with different pilus binding distances ($d_{\mathrm{bind}} = 2.6, 2.0, 1.8, 1.5, 1.4\,\mu\mathrm{m}$) are simulated. The displacement of these colonies as a function of time on pattern 1 is shown in Fig. 6.7. Colonies with longer pilus binding distances ($d_{\mathrm{bind}} = 2.6, 2.0, 1.8\,\mu\mathrm{m}$) show forward migration along the positive x-axis (to the right) on pattern 1, consistent with the results of the previous sections. Surprisingly, however, colonies with shorter pilus binding distances ($d_{\mathrm{bind}} = 1.5, 1.4\,\mu\mathrm{m}$) migrate in the opposite direction (to the left). Furthermore, it is evident from the figure that the migration speed s_{m} of the colony decreases with a reduction in the pilus binding distance d_{bind}. These results can be summarized as the pilus binding distance d_{bind} not only influences the migration speed s_{m} of the colony but also can change the direction of migration on the patterns. This implies that the migration direction of the colony on the patterns is jointly determined by both the patterns and the parameters of the colony.

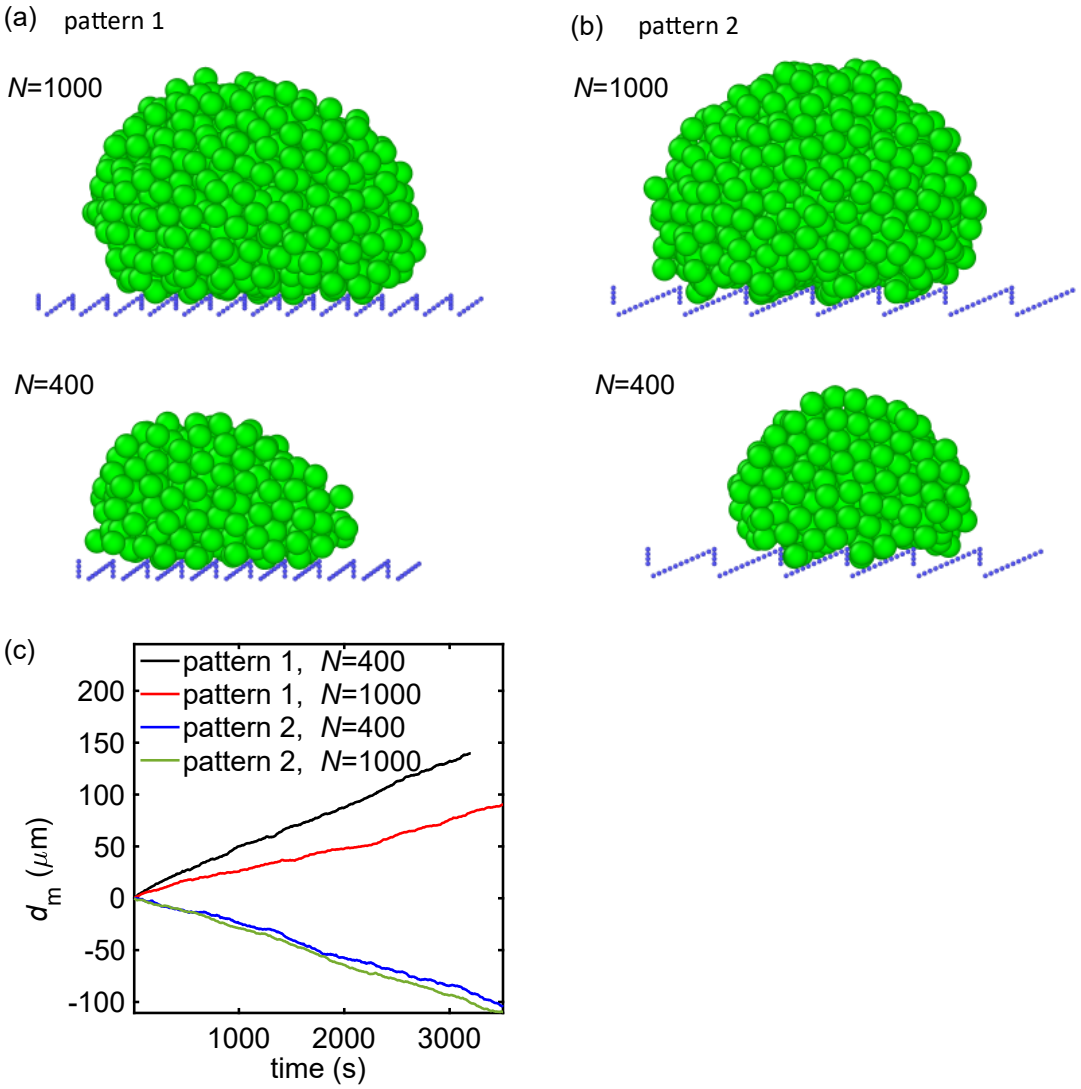

Figure 6.6: The simulated colonies with different numbers of bacteria $N = 1000, 400$ on (a) pattern 1 and (b) pattern 2. (c) The displacement $d_{\mathrm{m}}(t)$ of colonies with different numbers of bacteria migrating on these two patterns.

The binding of pili to the sawtooth surface generates asymmetric interaction forces that drive the directed migration of the colony on the pattern. These interaction forces are caused by two factors: the retraction of the pili and the motility of the bacteria. To verify whether the directed migration of the colony depends on the retraction of the surface-binding pili, colonies are simulated with a retraction velocity of 0 ($v_{\mathrm{p}} = 0$) of the surface-binding pili. The migration displacements of these colonies on patterns 1 and 2 are shown in Fig. 6.8. It is evident that colonies with$v_{\mathrm{p}} = 0$ still exhibit directed migration on the patterns. Furthermore, colonies with $v_{\mathrm{p}} = 0$ show higher magnitudes of migration speeds on patterns 1 and 2 compared to colonies

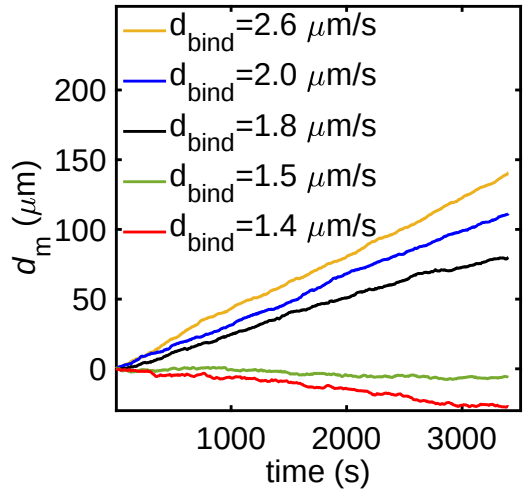

Figure 6.7: The displacement $d_{\mathrm{m}}(t)$ of the colonies with different pilus binding distances d_{bind} migrating on pattern 1.

with $v_{\mathrm{p}} = 1.0\,\mu\mathrm{m/s}$. This indicates that eliminating the retraction of surface-binding pili enhances the directed migration of the colony.

Although the driving force for twitching motility is pili retraction, our simulations show that colonies can still migrate directionally even without retraction between the bacteria and the surface.

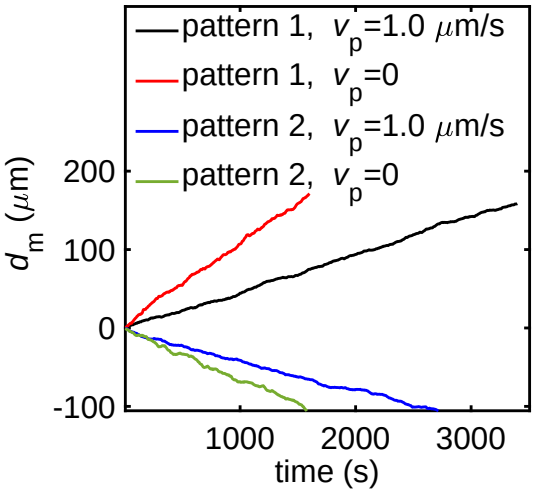

Figure 6.8: The displacement $d_{\mathrm{m}}(t)$ of the colonies with different retraction velocities v_{p} of the surface-binding pili migrating on pattern 1 and pattern 2.

6.4 Effective model

The migration velocity $v_{\mathrm{m}}(t)$ of the colony under the influence of unbalanced active forces can be described by the following Langevin equation

$$m_{\mathrm{colony}}\frac{\mathrm{d}v_{\mathrm{m}}(t)}{\mathrm{d}t} = -\gamma_{\mathrm{eff}}v_{\mathrm{m}}(t) + F_{\mathrm{drive}} + \xi_{\mathrm{f}}(t), \tag{6.4}$$

where m_{colony} is the mass of the colony, γ_{eff} is an effective translational friction coefficient, F_{drive} is a constant force that drives the colony to migrate, $\xi_{\mathrm{f}}(t)$ represents fluctuating forces with vanishing mean. The velocity of the colony $v_{\mathrm{m}}(t)$ reaches an average stationary value of

$$v_{\mathrm{m}}^{0} = \frac{F_{\mathrm{drive}}}{\gamma_{\mathrm{eff}}}. \tag{6.5}$$

Now, we add an extra force F_{ext} to the colony to obtain an equation of motion as

$$m_{\mathrm{colony}}\frac{\mathrm{d}v_{\mathrm{m}}(t)}{\mathrm{d}t} = -\gamma_{\mathrm{eff}}v_{\mathrm{m}}(t) + F_{\mathrm{drive}} + F_{\mathrm{ext}} + \xi_{\mathrm{f}}(t). \tag{6.6}$$

The colony eventually reaches a constant average velocity given by

$$v_{\mathrm{m}}^{1} = \frac{F_{\mathrm{drive}} + F_{\mathrm{ext}}}{\gamma_{\mathrm{eff}}}. \tag{6.7}$$

Insertion of this result into Eq. (6.5) yields the effectiv friction coefficient

$$\gamma_{\mathrm{eff}} = \frac{F_{\mathrm{ext}}}{v_{\mathrm{m}}^{1} - v_{\mathrm{m}}^{0}}. \tag{6.8}$$

The constant migration velocity v_{m}^{1} of the colony on pattern 2 as a function of the extra force F_{ext} is shown in Fig. 6.9. The results can be fitted into a straight line with a slope of α_{m}. Thus, we have the value for $\gamma_{\mathrm{eff}} = 1/\alpha_{\mathrm{m}}$. In this figure, the slope $\alpha_{\mathrm{m}} = 0.0084$, indicating that the effective friction for the colony migration motion on pattern $\gamma_{\mathrm{eff}} = 1/\alpha_{\mathrm{m}} = 119.5\,\mathrm{pN}\cdot\mathrm{s}/\mu\mathrm{m}$, therefore the driving force $F_{\mathrm{drive}} = v_{\mathrm{m}}^{0}\gamma_{\mathrm{eff}} = -4.362\,\mathrm{pN}$.

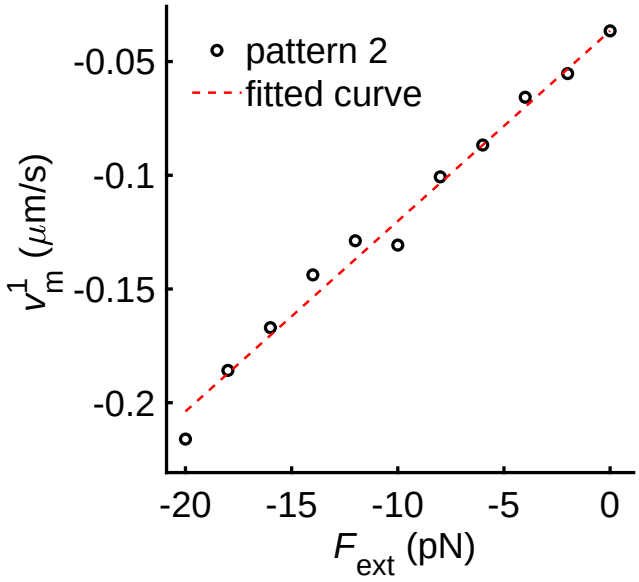

Figure 6.9: The constant velocity v_{m}^{1} of the colony's migration on pattern 1 under the traction of an extra force F_{ext}.

6.5 Summary

The movement of bacterial colonies on an asymmetric surface is simulated. The colonies rely on pili to adhere to a sawtooth pattern. we observe that the colonies can exhibit directed movement on certain patterns. The direction and speed of the motion depend sensitively on the shape of the pattern. The speed depends on the size of the colonies but a clear correlation between speeds and colony size on different patterns could not be established. The cutoff distance for pilus binding, corresponding to the maximum length of pili, affects both the direction and speed of motion on different patterns. By eliminating the active retraction of surface-binding pili, we find that the force generated by pili at the surface is not a necessary condition for a directed migration of the colony. Overall, we have shown that directional motion of colonies on sawtooth pattern is a complex and intriguing behavior whose occurrence is demonstrated in simulations.

6.6 Appendix

6.6.1 Parameters values

Parameters values that are used for the simulations in this chapter are listed in Tab. 6.1, parameters not listed here use the same values as in Tab. 2.1.

Table 6.1: The choice of parameters for the simulations in this chapter.

Parameter	Value	Unit
cell radius R	0.5	d_c
cell mass m	1.0	$f_\mathrm{c} t_\mathrm{c}^2 d_\mathrm{c}^{-1}$
pilus spring constant k	500	$f_\mathrm{c} d_\mathrm{c}^{-1}$
pilus stall force f_s	180	f_c
maximum retraction velocity of pili v_0	2.0	$d_\mathrm{c} t_\mathrm{c}^{-1}$
number of pili per cell	7	
simulation time step Δt	2×10^{-4}	t_c
pilus rupture rate k_rupt	3.0	t_c^{-1}
pilus binding cutoff distance d_bind	1.8	d_c
pilus binding rate k_bind	50	t_c^{-1}
pilus-pilus bond rupture force scale F_rupt	22.5	f_c
maximum conservative force a_0	2000	$f_\mathrm{c} d_\mathrm{c}^{-1}$
conservative force cutoff $d_\mathrm{con} = 2R$	1.0	d_c
diplococcus spring constant a_growth	2000	$f_\mathrm{c} d_\mathrm{c}^{-1}$
friction coefficient γ	50	$f_\mathrm{c} t_\mathrm{c} d_\mathrm{c}^{-1}$
thermal energy scale $k_\mathrm{B} T$	1×10^{-4}	$f_\mathrm{c} d_\mathrm{c}$
dissipative and random force cutoff d_dpd	1.5	d_c

Chapter 7

Summary and Concluding Remarks

In this dissertation, we investigate the non-equilibrium dynamics of bacterial colonies through the integration of experimental observations, computational simulations, and theoretical analyses .

The *N. gonorrhoeae* have a spherical cell body with a diameter of roughly 1 m, and T4P are isotropically displayed on their entire cell surface. T4P are helical polymers consisting mainly of the major subunit PilE. T4P undergo polymerization and depolymerization processes, resulting in cycles of elongation and retraction. During retraction, T4P are capable of generating high forces. *N. gonorrhoeae* do not exhibit active swimming in a liquid medium or the ability to sense chemical gradients. Their mechanism of surface twitching motility and cell-cell attraction is mediated by the retraction of T4P. Bacteria grow and aggregate into colonies through the interaction of their T4P.

We have introduced a simulation model to study the non-equilibrium dynamics of bacterial colonies. Bacteria are modeled by solvent-free dissipative particle dynamics. A DPD particle represents a single bacterium and the volume repulsion, dissipation and thermal fluctuations of the bacteria are included. By adding an additional force to represent the interaction between T4P, the binding, retraction and rupture of pili are also taken into account. The choice of some critical simulation parameters is based on experimental measurements, such as bacterial radius, number of pili per cell, pilus length, pilus spring constant, pilus stall force, maximum retraction velocity of pili, pilus characteristic rupture force.

We have established a bacterial growth model in which one single bacterium can grow and divide to form a colony. The simulation results show that cell

numbers and colony radii increase exponentially with time. The local order in the simulated colonies is investigated by calculating the radial distribution function. The simulations indicate that decreasing the pilus retraction velocity increases the spatial ordering, and higher numbers of pili result in a higher degree of spatial ordering.

Phase separation in mixed colonies has been simulated. For a mixture of two cell types carrying different numbers of pili, the colonies segregate and the cells that have many pili (14 pili) concentrate in the center of the colony, while cells with fewer pili (7 pili) form a spherical shell at the periphery. For a mixture of two cell types that have high pilus rupture forces among each other, but lower rupture forces for pairs of different cells, simulations show the formation of two segregated half-spheres. These simulations produce results that are consistent with experimental data.

We quantifiy the power spectral density of simulated bacterial colonies and compare the results with experimental data. The simulation results are in good qualitative agreement with the experimental data. We also propose a setup for measuring fluctuations in the colony shape and its response to external force. The simulations yield a significant violation of the equilibrium fluctuation-response relationship. Our simulations also show that the force generated by the surface-binding pili can drive colonies to invade narrow channels.

We investigate the spreading behavior of colonies on solid surfaces. Experiments investigating the wetting behavior of bacterial colonies on surfaces have been carried out in the laboratory of Prof. Dr. Berenike Maier at University of cologne. The results indicate that these colonies exhibit a large steady-state contact angles ($\theta > 90°$) on the surface. The impact of azithromycin treatment on the wetting behavior of bacterial colonies is notable. Experimental results reveal a significant decrease in the steady-state contact angle of the colonies, suggesting an enhanced wetting capacity due to azithromycin treatment. We present a simulation model that incorporates individual bacteria and surfaces to investigate colony wetting behavior. Both the experimental and simulation results indicate that the steady-state contact angle correlates with colony size, showing an increase with increasing colony size. Azithromycin treatment not only decreases the steady-state contact angle but also accelerates the spreading in the colonies. Therefore, it can be concluded that the wetting behavior of the colonies on the surface is improved by azithromycin treatment.

The dynamics of colonies consisting of two types of bacteria is studied. By choosing appropriate parameters for the inactive bacteria, the colony folding phenomenon is reproduced in simulations. The simulations show that the configuration of such mixed colonies can become unstable, leading to a rapid folding and reorganization of the colony structure. The simulation results indicate that both the radius of the inactive bacterial cluster and the pilus binding rate play a significant role in colony folding.

The movement of bacterial colonies on geometrically asymmetric surfaces is simulated. These simulations show that colonies can exhibit directed movement on certain sawtooth patterns. The direction and speed of the motion depend sensitively on the shape of the pattern. The cutoff distance for pilus binding affects both the direction and speed of motion on different patterns. Our simulations have demonstrated that the directional motion of colonies on a sawtooth pattern is a complex and intriguing behavior.

Bibliography

[1] Navish Wadhwa and Howard C Berg. "Bacterial motility: machinery and mechanisms". In: *Nat. Rev. Microbiol.* 20.3 (2022), pp. 161–173.

[2] Rasika M Harshey. "Bacterial motility on a surface: many ways to a common goal". In: *Annu. Rev. Microbiol.* 57.1 (2003), pp. 249–273.

[3] Daniel B Kearns. "A field guide to bacterial swarming motility". In: *Nat. Rev. Microbiol.* 8.9 (2010), pp. 634–644.

[4] Konark Bisht and Rahul Marathe. "Rectification of twitching bacteria through narrow channels: A numerical simulations study". In: *Phys. Rev. E* 101.4 (2020), p. 042409.

[5] John S Mattick. "Type IV pili and twitching motility". In: *Annu. Rev. Microbiol.* 56.1 (2002), pp. 289–314.

[6] Alexey J Merz, Magdalene So, and Michael P Sheetz. "Pilus retraction powers bacterial twitching motility". In: *Nature* 407.6800 (2000), pp. 98–102.

[7] Jeffrey M Skerker and Howard C Berg. "Direct observation of extension and retraction of type IV pili". In: *PNAS* 98.12 (2001), pp. 6901–6904.

[8] Claudia Meel et al. "Three-dimensional obstacles for bacterial surface motility". In: *Small* 8.4 (2012), pp. 530–534.

[9] Claudia Holz et al. "Bacterial motility and clustering guided by microcontact printing". In: *Nano Lett.* 9.12 (2009), pp. 4553–4557.

[10] Berenike Maier. "The bacterial type IV pilus system–a tunable molecular motor". In: *Soft Matter* 9.24 (2013), pp. 5667–5671.

[11] Lisa Craig, Katrina T Forest, and Berenike Maier. "Type IV pili: dynamics, biophysics and functional consequences". In: *Nat. Rev. Microbiol.* 17.7 (2019), pp. 429–440.

[12] Berenike Maier and Gerard CL Wong. "How bacteria use type IV pili machinery on surfaces". In: *Trends Microbiol.* 23.12 (2015), pp. 775–788.

[13] Rahul Marathe et al. "Bacterial twitching motility is coordinated by a two-dimensional tug-of-war with directional memory". In: *Nat. Commun.* 5.1 (2014), pp. 1–10.

[14] Berenike Maier et al. “Single pilus motor forces exceed 100 pN”. In: *PNAS* 99.25 (2002), pp. 16012–16017.

[15] Robert Zöllner, Tom Cronenberg, and Berenike Maier. “Motor properties of PilT-independent type 4 pilus retraction in gonococci”. In: *J. Bacteriol.* 201.18 (2019), e00778–18.

[16] Anton Welker et al. “Molecular motors govern liquidlike ordering and fusion dynamics of bacterial colonies”. In: *Phys. Rev. Lett.* 121.11 (2018), p. 118102.

[17] Nicolas Biais et al. “Cooperative retraction of bundled type IV pili enables nanonewton force generation”. In: *PLoS Biol.* 6.4 (2008), e87.

[18] Claudia Holz et al. “Multiple pilus motors cooperate for persistent bacterial movement in two dimensions”. In: *Phys. Rev. Lett.* 104.17 (2010), p. 178104.

[19] Vasily Zaburdaev et al. “Uncovering the mechanism of trapping and cell orientation during Neisseria gonorrhoeae twitching motility”. In: *Biophys. J.* 107.7 (2014), pp. 1523–1531.

[20] Wolfram Pönisch et al. “Multiscale modeling of bacterial colonies: how pili mediate the dynamics of single cells and cellular aggregates”. In: *New J. Phys.* 19.1 (2017), p. 015003.

[21] Wolfram Pönisch, Christoph A Weber, and Vasily Zaburdaev. “How bacterial cells and colonies move on solid substrates”. In: *Phys. Rev. E* 99.4 (2019), p. 042419.

[22] Daria Bonazzi et al. “Intermittent pili-mediated forces fluidize Neisseria meningitidis aggregates promoting vascular colonization”. In: *Cell* 174.1 (2018), pp. 143–155.

[23] M Reza Shaebani et al. “Computational models for active matter”. In: *Nat. Rev. Phys.* 2.4 (2020), pp. 181–199.

[24] Johannes Taktikos et al. “Pili-induced clustering of N. gonorrhoeae bacteria”. In: *PLoS One* 10.9 (2015), e0137661.

[25] Robert Zöllner et al. “Type IV pilin post-translational modifications modulate material properties of bacterial colonies”. In: *Biophys. J.* 116.5 (2019), pp. 938–947.

[26] Dustin L Higashi et al. “Dynamics of Neisseria gonorrhoeae attachment: microcolony development, cortical plaque formation, and cytoprotection”. In: *Infect. Immun.* 75.10 (2007), pp. 4743–4753.

[27] Lena Dewenter, Thorsten E Volkmann, and Berenike Maier. "Oxygen governs gonococcal microcolony stability by enhancing the interaction force between type IV pili". In: *Integr. Biol.* 7.10 (2015), pp. 1161–1170.

[28] Wolfram Pönisch et al. "Pili mediated intercellular forces shape heterogeneous bacterial microcolonies prior to multicellular differentiation". In: *Sci. Rep.* 8.1 (2018), pp. 1–10.

[29] Emad Moeendarbary, Teng Yong Ng, and M Zangeneh. "Dissipative particle dynamics: introduction, methodology and complex fluid applicationsa review". In: *Int. J. Appl. Mech.* 1.04 (2009), pp. 737–763.

[30] Akira Satoh. *Introduction to practice of molecular simulation: molecular dynamics, Monte Carlo, Brownian dynamics, Lattice Boltzmann and dissipative particle dynamics*. Elsevier, 2010.

[31] Pep Espanol and Patrick B Warren. "Perspective: Dissipative particle dynamics". In: *J. Chem. Phys.* 146.15 (2017).

[32] Shiyi Chen and Gary D Doolen. "Lattice Boltzmann method for fluid flows". In: *Annu. Rev. Fluid Mech.* 30.1 (1998), pp. 329–364.

[33] R Robert Nourgaliev et al. "The lattice Boltzmann equation method: theoretical interpretation, numerics and implications". In: *Int. J. Multiph. Flow* 29.1 (2003), pp. 117–169.

[34] Ulf D Schiller, Timm Krüger, and Oliver Henrich. "Mesoscopic modelling and simulation of soft matter". In: *Soft matter* 14.1 (2018), pp. 9–26.

[35] Xiaoyi He and Li-Shi Luo. "Theory of the lattice Boltzmann method: From the Boltzmann equation to the lattice Boltzmann equation". In: *Phys. Rev. E* 56.6 (1997), p. 6811.

[36] Raymond Kapral. "Multiparticle collision dynamics: Simulation of complex systems on mesoscales". In: *Adv. Chem. Phys* 140 (2008), p. 89.

[37] Anatoly Malevanets and Raymond Kapral. "Mesoscopic model for solvent dynamics". In: *J. Chem. Phys.* 110.17 (1999), pp. 8605–8613.

[38] T Ihle and DM Kroll. "Stochastic rotation dynamics: A Galilean-invariant mesoscopic model for fluid flow". In: *Phys. Rev. E* 63.2 (2001), p. 020201.

[39] CM Pooley and JM Yeomans. "Kinetic theory derivation of the transport coefficients of stochastic rotation dynamics". In: *J. Phys. Chem. B* 109.14 (2005), pp. 6505–6513.

[40] Thomas Ihle, E Tüzel, and Daniel M Kroll. "Equilibrium calculation of transport coefficients for a fluid-particle model". In: *Phys. Rev. E* 72.4 (2005), p. 046707.

[41] Ingo O Götze, Hiroshi Noguchi, and Gerhard Gompper. "Relevance of angular momentum conservation in mesoscale hydrodynamics simulations". In: *Phys. Rev. EE* 76.4 (2007), p. 046705.

[42] Anatoly Malevanets and Raymond Kapral. "Solute molecular dynamics in a mesoscale solvent". In: *J. Chem. Phys.* 112.16 (2000), pp. 7260–7269.

[43] Pep Español. "Fluid particle dynamics: A synthesis of dissipative particle dynamics and smoothed particle dynamics". In: *Europhys. Lett.* 39.6 (1997), p. 605.

[44] Pep Espanol. "Dissipative particle dynamics with energy conservation". In: *Europhys. Lett.* 40.6 (1997), p. 631.

[45] Eirik G Flekkøy and Peter V Coveney. "From molecular dynamics to dissipative particle dynamics". In: *Phys. Rev. Lett.* 83.9 (1999), p. 1775.

[46] Eirik G Flekkøy, Peter V Coveney, and Gianni De Fabritiis. "Foundations of dissipative particle dynamics". In: *Phys. Rev. E* 62.2 (2000), p. 2140.

[47] T Kinjo and S Hyodo. "Linkage between atomistic and mesoscale coarse-grained simulation". In: *Mol. Simulat.* 33.4-5 (2007), pp. 417–420.

[48] Robert D Groot and KL Rabone. "Mesoscopic simulation of cell membrane damage, morphology change and rupture by nonionic surfactants". In: *Biophys. J.* 81.2 (2001), pp. 725–736.

[49] René Pool and Peter G Bolhuis. "Can purely repulsive soft potentials predict micelle formation correctly?" In: *Phys. Chem. Chem. Phys.* 8.8 (2006), pp. 941–948.

[50] PJ Hoogerbrugge and JMVA Koelman. "Simulating microscopic hydrodynamic phenomena with dissipative particle dynamics". In: *Europhys. Lett.* 19.3 (1992), p. 155.

[51] JMVA Koelman and PJ Hoogerbrugge. "Dynamic simulations of hard-sphere suspensions under steady shear". In: *Europhys. Lett.* 21.3 (1993), p. 363.

[52] Pep Espanol and Patrick Warren. "Statistical mechanics of dissipative particle dynamics". In: *Europhys. Lett.* 30.4 (1995), p. 191.

[53] Daan Frenkel and Berend Smit. *Understanding molecular simulation: from algorithms to applications*. Academic Press San Diego, 2002.

[54] J Bonet Avalos and AD Mackie. "Dissipative particle dynamics with energy conservation". In: *Europhys. Lett.* 40.2 (1997), p. 141.

[55] CA Marsh and PV Coveney. "Detailed balance and H-theorems for dissipative particle dynamics". In: *J. Phys. A: Math. Gen.* 31.31 (1998), p. 6561.

[56] AA Louis, PG Bolhuis, and JP Hansen. "Mean-field fluid behavior of the Gaussian core model". In: *Phys. Rev. E* 62.6 (2000), p. 7961.

[57] PB Warren. "Vapor-liquid coexistence in many-body dissipative particle dynamics". In: *Phys. Rev. E* 68.6 (2003), p. 066702.

[58] I Pagonabarraga and D Frenkel. "Dissipative particle dynamics for interacting systems". In: *J. Chem. Phys.* 115.11 (2001), pp. 5015–5026.

[59] Patrick B Warren. "Hydrodynamic bubble coarsening in off-critical vapor-liquid phase separation". In: *Phys. Rev. Lett.* 87.22 (2001), p. 225702.

[60] SY Trofimov, ELF Nies, and MAJ Michels. "Thermodynamic consistency in dissipative particle dynamics simulations of strongly nonideal liquids and liquid mixtures". In: *J. Chem. Phys.* 117.20 (2002), pp. 9383–9394.

[61] Aziz Ghoufi, Janine Emile, and Patrice Malfreyt. "Recent advances in many body dissipative particles dynamics simulations of liquid-vapor interfaces". In: *Eur. Phys. J. E* 36 (2013), pp. 1–12.

[62] Marco Arienti et al. "Many-body dissipative particle dynamics simulation of liquid/vapor and liquid/solid interactions". In: *J. Chem. Phys.* 134.20 (2011).

[63] Samy Merabia and Ignacio Pagonabarraga. "Density dependent potentials: Structure and thermodynamics". In: *J. Chem. Phys.* 127.5 (2007).

[64] Aziz Ghoufi and Patrice Malfreyt. "Calculation of the surface tension from multibody dissipative particle dynamics and Monte Carlo methods". In: *Phys. Rev. E* 82.1 (2010), p. 016706.

[65] Patrick B Warren. "No-go theorem in many-body dissipative particle dynamics". In: *Phys. Rev. E* 87.4 (2013), p. 045303.

[66] Maryam Atashafrooz and Nargess Mehdipour. "Many-body dissipative particle dynamics simulation of liquid–vapor coexisting curve in sodium". In: *J. Chem. Eng. Data* 61.10 (2016), pp. 3659–3664.

[67] Patrick B Warren. "A manifesto for one-body terms: the simplest of all many-body interactions?" In: *J. Phys.: Condens.Matter* 15.48 (2003), S3467.

[68] Xijun Fan et al. "Simulating flow of DNA suspension using dissipative particle dynamics". In: *Phys. Fluids* 18.6 (2006).

[69] Huan Lei et al. "Modeling nanoscale hydrodynamics by smoothed dissipative particle dynamics". In: *J. Chem. Phys.* 142.19 (2015).

[70] Xin Bian et al. "Multiscale modeling of particle in suspension with smoothed dissipative particle dynamics". In: *Phys. Fluids* 24.1 (2012).

[71] Adolfo Vázquez-Quesada, Xin Bian, and Marco Ellero. "Three-dimensional simulations of dilute and concentrated suspensions using smoothed particle hydrodynamics". In: *Comp. Part. Mech.* 3 (2016), pp. 167–178.

[72] Nicolas Moreno et al. "Multiscale modeling of blood flow: coupling finite elements with smoothed dissipative particle dynamics". In: *Procedia. Comput. Sci.* 18 (2013), pp. 2565–2574.

[73] Kathrin Müller, Dmitry A Fedosov, and Gerhard Gompper. "Margination of micro-and nano-particles in blood flow and its effect on drug delivery". In: *Sci. Rep.* 4.1 (2014), p. 4871.

[74] S Litvinov, XY Hu, and NA Adams. "Numerical simulation of tethered DNA in shear flow". In: *J. Phys.: Condens.Matter* 23.18 (2011), p. 184118.

[75] Sergey Litvinov et al. "Simulation of individual polymer chains and polymer solutions with smoothed dissipative particle dynamics". In: *Fluids* 1.1 (2016), p. 7.

[76] Sergey Litvinov et al. "Smoothed dissipative particle dynamics model for polymer molecules in suspension". In: *Phys. Rev. E* 77.6 (2008), p. 066703.

[77] Cedric Thieulot, LPBM Janssen, and Pep Español. "Smoothed particle hydrodynamics model for phase separating fluid mixtures. I. General equations". In: *Phys. Rev. E* 72.1 (2005), p. 016713.

[78] Cedric Thieulot and Pep Español. "Non-isothermal diffusion in a binary mixture with smoothed particle hydrodynamics". In: *Comput. Phys. Commun.* 169.1-3 (2005), pp. 172–176.

[79] Nikolai D Petsev, L Gary Leal, and M Scott Shell. "Multiscale simulation of ideal mixtures using smoothed dissipative particle dynamics". In: *J. Chem. Phys.* 144.8 (2016).

[80] Adolfo Vázquez-Quesada, Marco Ellero, and Pep Español. "Smoothed particle hydrodynamic model for viscoelastic fluids with thermal fluctuations". In: *Phys. Rev. E* 79.5 (2009), p. 056707.

[81] Sergey Litvinov et al. "A splitting scheme for highly dissipative smoothed particle dynamics". In: *J. Comput. Phys.* 229.15 (2010), pp. 5457–5464.

[82] Dan S Bolintineanu et al. "Particle dynamics modeling methods for colloid suspensions". In: *Comp. Part. Mech.* 1 (2014), pp. 321–356.

[83] Mohamed Laradji and Michael JA Hore. "Nanospheres in phase-separating multicomponent fluids: A three-dimensional dissipative particle dynamics simulation". In: *J. Chem. Phys.* 121.21 (2004), pp. 10641–10647.

[84] Zhigang Li and German Drazer. "Hydrodynamic interactions in dissipative particle dynamics". In: *Phys. Fluids* 20.10 (2008).

[85] N Phan-Thien, N Mai-Duy, and BC Khoo. "A spring model for suspended particles in dissipative particle dynamics". In: *J. Rheol.* 58.4 (2014), pp. 839–867.

[86] ES Boek et al. "Simulating the rheology of dense colloidal suspensions using dissipative particle dynamics". In: *Phys. Rev. E* 55.3 (1997), p. 3124.

[87] Jonathan B Gibson et al. "Simulation of colloid-polymer systems using dissipative particle dynamics". In: *Mol. Simulat.* 23.1 (1999), pp. 1–41.

[88] Victor Pryamitsyn and Venkat Ganesan. "A coarse-grained explicit solvent simulation of rheology of colloidal suspensions". In: *J. Chem. Phys.* 122.10 (2005).

[89] W Pan, IV Pivkin, and GE Karniadakis. "Single-particle hydrodynamics in DPD: A new formulation". In: *Europhys. Lett.* 84.1 (2008), p. 10012.

[90] Wenxiao Pan, Bruce Caswell, and George Em Karniadakis. "Rheology, microstructure and migration in Brownian colloidal suspensions". In: *Langmuir* 26.1 (2010), pp. 133–142.

[91] Martin Whittle and Karl P Travis. "Dynamic simulations of colloids by core-modified dissipative particle dynamics". In: *J. Chem. Phys.* 132.12 (2010).

[92] Dmitry A Fedosov et al. "Predicting human blood viscosity in silico". In: *PNAS* 108.29 (2011), pp. 11772–11777.

[93] Dinar Katanov, Gerhard Gompper, and Dmitry A Fedosov. "Microvascular blood flow resistance: Role of red blood cell migration and dispersion". In: *Microvasc. Res.* 99 (2015), pp. 57–66.

[94] Xuejin Li, Petia M Vlahovska, and George Em Karniadakis. "Continuum- and particle-based modeling of shapes and dynamics of red blood cells in health and disease". In: *Soft matter* 9.1 (2013), pp. 28–37.

[95] Ting Ye, Nhan Phan-Thien, and Chwee Teck Lim. "Particle-based simulations of red blood cellsA review". In: *J. Biomech.* 49.11 (2016), pp. 2255–2266.

[96] Moubin Liu, Paul Meakin, and Hai Huang. "Dissipative particle dynamics with attractive and repulsive particle-particle interactions". In: *Phys. Fluids* 18.1 (2006).

[97] JanetteáL Jones, J áNoel Ruddock, NeiláA Spenley, et al. "Dynamics of a drop at a liquid/solid interface in simple shear fields: a mesoscopic simulation study". In: *Faraday Discuss.* 112 (1999), pp. 129–142.

[98] Yuxiang Wang and Shuo Chen. "Droplets impact on textured surfaces: mesoscopic simulation of spreading dynamics". In: *Appl. Surf. Sci.* 327 (2015), pp. 159–167.

[99] Maddalena Venturoli et al. "Mesoscopic models of biological membranes". In: *Phys. Rep.* 437.1-2 (2006), pp. 1–54.

[100] GJA Sevink and JGEM Fraaije. "Efficient solvent-free dissipative particle dynamics for lipid bilayers". In: *Soft Matter* 10.28 (2014), pp. 5129–5146.

[101] Liuyang Zhang, Matthew Becton, and Xianqiao Wang. "Designing nanoparticle translocation through cell membranes by varying amphiphilic polymer coatings". In: *J. Phys. Chem. B* 119.9 (2015), pp. 3786–3794.

[102] Haizhen Zhang et al. "Cooperative transmembrane penetration of nanoparticles". In: *Sci. Rep.* 5.1 (2015), p. 10525.

[103] Gernot Guigas and Matthias Weiss. "Membrane protein mobility depends on the length of extra-membrane domains and on the protein concentration". In: *Soft Matter* 11.1 (2015), pp. 33–37.

[104] NA Spenley. "Scaling laws for polymers in dissipative particle dynamics". In: *Europhys. Lett.* 49.4 (2000), p. 534.

[105] JT Padding and Willem J Briels. "Uncrossability constraints in mesoscopic polymer melt simulations: non-Rouse behavior of C 120 H 242". In: *J. Chem. Phys.* 115.6 (2001), pp. 2846–2859.

[106] Anand TN Kumar et al. "Investigations of amplitude and phase excitation profiles in femtosecond coherence spectroscopy". In: *J. Chem. Phys.* 114.2 (2001), pp. 701–724.

[107] Johan T Padding and Willem J Briels. "Time and length scales of polymer melts studied by coarse-grained molecular dynamics simulations". In: *J. Chem. Phys.* 117.2 (2002), pp. 925–943.

[108] Vasileios Symeonidis, George Em Karniadakis, and Bruce Caswell. "Dissipative particle dynamics simulations of polymer chains: scaling laws and shearing response compared to DNA experiments". In: *Phys. Rev. Lett.* 95.7 (2005), p. 076001.

[109] Petri Nikunen, Ilpo Vattulainen, and Mikko Karttunen. "Reptational dynamics in dissipative particle dynamics simulations of polymer melts". In: *Phys. Rev. E* 75.3 (2007), p. 036713.

[110] Florent Goujon, Patrice Malfreyt, and Dominic J Tildesley. "Mesoscopic simulation of entanglements using dissipative particle dynamics: Application to polymer brushes". In: *J. Chem. Phys.* 129.3 (2008).

[111] Mikio Yamanoi, Oliver Pozo, and Joao M Maia. "Linear and nonlinear dynamics of entangled linear polymer melts by modified tunable coarse-grained level Dissipative Particle Dynamics". In: *J. Chem. Phys.* 135.4 (2011).

[112] JT Padding and Willem J Briels. "Systematic coarse-graining of the dynamics of entangled polymer melts: the road from chemistry to rheology". In: *J. Phys.: Condens.Matter* 23.23 (2011), p. 233101.

[113] GJA Sevink, M Charlaganov, and JGEM Fraaije. "Coarse-grained hybrid simulation of liposomes". In: *Soft Matter* 9.10 (2013), pp. 2816–2831.

[114] Kai Zhou et al. "Non-equilibrium dynamics of bacterial coloniesgrowth, active fluctuations, segregation, adhesion, and invasion". In: *Commun. Phys.* 5.1 (2022), p. 251.

[115] Jonas Ranft et al. "Fluidization of tissues by cell division and apoptosis". In: *PNAS* 107.49 (2010), pp. 20863–20868.

[116] Markus Basan et al. "Dissipative particle dynamics simulations for biological tissues: rheology and competition". In: *Phys. Biol.* 8.2 (2011), p. 026014.

[117] Denis F Hinz et al. "Particle-based simulations of self-motile suspensions". In: *Comput. Phys. Commun.* 196 (2015), pp. 45–57.

[118] Robert D Groot and Patrick B Warren. "Dissipative particle dynamics: Bridging the gap between atomistic and mesoscopic simulation". In: *J. Chem. Phys.* 107.11 (1997), pp. 4423–4435.

[119] I Pagonabarraga, MHJ Hagen, and D Frenkel. "Self-consistent dissipative particle dynamics algorithm". In: *Europhys. Lett.* 42.4 (1998), p. 377.

[120] Tony Shardlow. "Splitting for dissipative particle dynamics". In: *SIAM J. Sci. Comput.* 24.4 (2003), pp. 1267–1282.

[121] Petri Nikunen, Mikko Karttunen, and Ilpo Vattulainen. "How would you integrate the equations of motion in dissipative particle dynamics simulations?" In: *Comput. Phys. Commun.* 153.3 (2003), pp. 407–423.

[122] G De Fabritiis et al. "Efficient numerical integrators for stochastic models". In: *Phys. A* 361.2 (2006), pp. 429–440.

[123] Mar Serrano et al. "A stochastic Trotter integration scheme for dissipative particle dynamics". In: *Math. Comput. Simulat.* 72.2-6 (2006), pp. 190–194.

[124] Fabrice Thalmann and Jean Farago. "Trotter derivation of algorithms for Brownian and dissipative particle dynamics". In: *J. Chem. Phys.* 127.12 (2007).

[125] Anuj Chaudhri and Jennifer R Lukes. "Velocity and stress autocorrelation decay in isothermal dissipative particle dynamics". In: *Phys. Rev. E* 81.2 (2010), p. 026707.

[126] Benedict Leimkuhler and Xiaocheng Shang. "On the numerical treatment of dissipative particle dynamics and related systems". In: *J. Comput. Phys.* 280 (2015), pp. 72–95.

[127] Benedict Leimkuhler and Xiaocheng Shang. "Pairwise adaptive thermostats for improved accuracy and stability in dissipative particle dynamics". In: *J. Comput. Phys.* 324 (2016), pp. 174–193.

[128] Oded Farago and Niels Grønbech-Jensen. "On the connection between dissipative particle dynamics and the Itô-Stratonovich dilemma". In: *J. Chem. Phys.* 144.8 (2016).

[129] Udo Seifert. "Stochastic thermodynamics, fluctuation theorems and molecular machines". In: *Rep. Prog. Phys.* 75.12 (2012), p. 126001.

[130] Takahiro Harada and Shin-ichi Sasa. "Equality connecting energy dissipation with a violation of the fluctuation-response relation". In: *Phys. Rev. Lett.* 95.13 (2005), p. 130602.

[131] Jacques Prost, J-F Joanny, and Juan MR Parrondo. "Generalized fluctuation-dissipation theorem for steady-state systems". In: *Phys. Rev. Lett.* 103.9 (2009), p. 090601.

[132] Federico S Gnesotto et al. "Broken detailed balance and non-equilibrium dynamics in living systems: a review". In: *Rep. Prog. Phys.* 81.6 (2018), p. 066601.

[133] Daisuke Mizuno et al. "Nonequilibrium mechanics of active cytoskeletal networks". In: *Science* 315.5810 (2007), pp. 370–373.

[134] Roland R Netz. "Fluctuation-dissipation relation and stationary distribution of an exactly solvable many-particle model for active biomatter far from equilibrium". In: *J. Chem. Phys.* 148.18 (2018), p. 185101.

[135] Anton Welker et al. "Spatiotemporal dynamics of growth and death within spherical bacterial colonies". In: *Biophys J.* 120.16 (2021), pp. 3418–3428.

[136] B Westling-Häggström et al. "Growth pattern and cell division in Neisseria gonorrhoeae". In: *J. Bacteriol.* 129.1 (1977), pp. 333–342.

[137] Mustafa Mir et al. "Optical measurement of cycle-dependent cell growth". In: *PNAS* 108.32 (2011), pp. 13124–13129.

[138] Manuel Campos et al. "A constant size extension drives bacterial cell size homeostasis". In: *Cell* 159.6 (2014), pp. 1433–1446.

[139] Ariel Amir. "Cell size regulation in bacteria". In: *Phys. Rev. Lett.* 112.20 (2014), p. 208102.

[140] Lisa Willis and Kerwyn Casey Huang. "Sizing up the bacterial cell cycle". In: *Nat. Rev. Microbiol.* 15.10 (2017), pp. 606–620.

[141] Ahmet Nihat Simsek et al. "Substrate-rigidity dependent migration of an idealized twitching bacterium". In: *Soft Matter* 15.30 (2019), pp. 6224–6236.

[142] Pep Espanol. "Hydrodynamics from Dissipative Particle Dynamics". In: *Phys. Rev. E* 52 (1995), p. 1734.

[143] Steve Plimpton. "Fast parallel algorithms for short-range molecular dynamics". In: *J. Comput. Phys.* 117.1 (1995), pp. 1–19.

[144] Alexander Stukowski. "Visualization and analysis of atomistic simulation data with OVITO–the Open Visualization Tool". In: *Modell. Simul. Mater. Sci. Eng.* 18.1 (2009), p. 015012.

[145] Enno R Oldewurtel et al. "Differential interaction forces govern bacterial sorting in early biofilms". In: *eLife* 4 (2015), e10811.

[146] DAVID S Stephens, JOHN W Krebs, and ZA McGee. "Loss of pili and decreased attachment to human cells by Neisseria meningitidis and Neisseria gonorrhoeae exposed to subinhibitory concentrations of antibiotics". In: *Infect. Immun.* 46.2 (1984), pp. 507–513.

[147] Tom Cronenberg et al. "Antibiotics modulate attractive interactions in bacterial colonies affecting survivability under combined treatment". In: *PLoS Pathog.* 17.2 (2021), e1009251.

[148] Marc Hennes, Tom Cronenberg, and Berenike Maier. "Caging dynamics in bacterial colonies". In: *Phys. Rev. Res.* 4.1 (2022), p. 013187.

[149] Michael E Cates and Julien Tailleur. "Motility-induced phase separation". In: *Annu. Rev. Condens. Matter Phys.* 6.1 (2015), pp. 219–244.

[150] Thomas Speck et al. "Effective Cahn-Hilliard equation for the phase separation of active Brownian particles". In: *Phys. Rev. Lett.* 112.21 (2014), p. 218304.

[151] Andreas Zöttl and Holger Stark. "Emergent behavior in active colloids". In: *J. Phys.: Condens. Matter* 28.25 (2016), p. 253001.

[152] Pasquale Digregorio et al. "Full phase diagram of active Brownian disks: From melting to motility-induced phase separation". In: *Phys. Rev. Lett.* 121.9 (2018), p. 098003.

[153] Clara Del Junco, Laura Tociu, and Suriyanarayanan Vaikuntanathan. "Energy dissipation and fluctuations in a driven liquid". In: *PNAS* 115.14 (2018), pp. 3569–3574.

[154] Ming Han et al. "Effective temperature concept evaluated in an active colloid mixture". In: *PNAS* 114.29 (2017), pp. 7513–7518.

[155] Hui-Shun Kuan et al. "Continuum theory of active phase separation in cellular aggregates". In: *Phys. Rev. Lett.* 126.1 (2021), p. 018102.

[156] Nils Podewitz, Morgan Delarue, and J Elgeti. "Tissue homeostasis: A tensile state". In: *Europhys. Lett.* 109.5 (2015), p. 58005.

[157] Nirmalendu Ganai et al. "Mechanics of tissue competition: interfaces stabilize coexistence". In: *New J. Phys.* 21.6 (2019), p. 063017.

[158] K Younge et al. "A model system for examining the radial distribution function". In: *Am. J. Phys.* 72.9 (2004), pp. 1247–1250.

[159] Bernd AF Kopera and Markus Retsch. "Computing the 3D radial distribution function from particle positions: an advanced analytic approach". In: *Anal. Chem.* 90.23 (2018), pp. 13909–13914.

[160] Albert K Harris. "Is cell sorting caused by differences in the work of intercellular adhesion? A critique of the Steinberg hypothesis". In: *J. Theor. Biol.* 61.2 (1976), pp. 267–285.

[161] Sebastian Kraus-Römer et al. "External Stresses Affect Gonococcal Type 4 Pilus Dynamics." In: *Front. Microbiol.* 13 (2022), pp. 839711–839711.

[162] Hervé Turlier et al. "Equilibrium physics breakdown reveals the active nature of red blood cell flickering". In: *Nat. Phys.* 12.5 (2016), pp. 513–519.

[163] OV Voinov. "Hydrodynamics of wetting". In: *Fluid Dyn.* 11.5 (1976), pp. 714–721.

[164] LH Tanner. "The spreading of silicone oil drops on horizontal surfaces". In: *J. Phys. D: Appl. Phys.* 12.9 (1979), p. 1473.

[165] Daniel Bonn et al. "Wetting and spreading". In: *Rev. Mod. Phys.* 81.2 (2009), p. 739.

[166] Benny Davidovitch, Esteban Moro, and Howard A Stone. "Spreading of viscous fluid drops on a solid substrate assisted by thermal fluctuations". In: *Phys. Rev. Lett.* 95.24 (2005), p. 244505.

[167] G Martic et al. "A molecular dynamics simulation of capillary imbibition". In: *Langmuir* 18.21 (2002), pp. 7971–7976.

[168] Richard Lucas. "Ueber das Zeitgesetz des kapillaren Aufstiegs von Flüssigkeiten". In: *Kolloid-Zeitschrift* 23.1 (1918), pp. 15–22.

[169] Edward W Washburn. "The dynamics of capillary flow". In: *Phys. Rev.* 17.3 (1921), p. 273.

[170] Anne-Laure Biance, Christophe Clanet, and David Quéré. "First steps in the spreading of a liquid droplet". In: *Phys. Rev. E* 69.1 (2004), p. 016301.

[171] James C Bird, Shreyas Mandre, and Howard A Stone. "Short-time dynamics of partial wetting". In: *Phys. Rev. Lett.* 100.23 (2008), p. 234501.

[172] Koen G Winkels et al. "Initial spreading of low-viscosity drops on partially wetting surfaces". In: *Phys. Rev. E* 85.5 (2012), p. 055301.

[173] Surjyasish Mitra and Sushanta K Mitra. "Understanding the early regime of drop spreading". In: *Langmuir* 32.35 (2016), pp. 8843–8848.

[174] Antonin Eddi, Koen G Winkels, and Jacco H Snoeijer. "Short time dynamics of viscous drop spreading". In: *Phys. Fluids* 25.1 (2013), p. 013102.

[175] Pierre-Gilles De Gennes. "Wetting: statics and dynamics". In: *Rev. Mod. Phys.* 57.3 (1985), p. 827.

[176] AM Cazabat and MA Cohen Stuart. "Dynamics of wetting: effects of surface roughness". In: *J. Phys. Chem.* 90.22 (1986), pp. 5845–5849.

[177] Jing-Den Chen. "Experiments on a spreading drop and its contact angle on a solid". In: *J. Colloid Interf. Sci.* 122.1 (1988), pp. 60–72.

[178] Jaime Lopez, Clarence A Miller, and Eli Ruckenstein. "Spreading kinetics of liquid drops on solids". In: *J. Colloid Interf. Sci.* 56.3 (1976), pp. 460–468.

[179] Ying-Chih Liao, Yen-Ching Li, and Hsien-Hung Wei. "Drastic changes in interfacial hydrodynamics due to wall slippage: slip-intensified film thinning, drop spreading, and capillary instability". In: *Phys. Rev. Lett.* 111.13 (2013), p. 136001.

[180] LM Hocking. "Rival contact-angle models and the spreading of drops". In: *J. Fluid Mech.* 239 (1992), pp. 671–681.

[181] Uwe Albrecht, Achim Otto, and Paul Leiderer. "Two-dimensional liquid polymer diffusion: experiment and simulation". In: *Phys. Rev. Lett.* 68.21 (1992), p. 3192.

[182] Hsien-Hung Wei, Heng-Kwong Tsao, and Kang-Ching Chu. "Slipping moving contact lines: critical roles of de Genness footin dynamic wetting". In: *J. Fluid Mech.* 873 (2019), pp. 110–150.

[183] F Brochard-Wyart, G Debregeas, and PG De Gennes. "Spreading of viscous droplets on a non viscous liquid". In: *Colloid Polym. Sci.* 274.1 (1996), pp. 70–72.

[184] Laurent Bacri, G Debregeas, and Françoise Brochard-Wyart. "Experimental study of the spreading of a viscous droplet on a nonviscous liquid". In: *Langmuir* 12.26 (1996), pp. 6708–6711.

[185] Seong Jin Kim et al. "Liquid spreading on superhydrophilic micropillar arrays". In: *J. Fluid Mech.* 680 (2011), pp. 477–487.

[186] Chengxi Zhao et al. "Fluctuation-driven dynamics in nanoscale thin-film flows: physical insights from numerical investigations". In: *Phys. Rev. Fluids* 7.2 (2022), p. 024203.

[187] Jennifer M Andrews. "Determination of minimum inhibitory concentrations". In: *J. Antimicrob. Chemoth.* 48.suppl_1 (2001), pp. 5–16.

[188] A Amirfazli and AW Neumann. "Status of the three-phase line tension: a review". In: *Adv. Colloid Interfac.* 110.3 (2004), pp. 121–141.

[189] Matej Kanduč. "Going beyond the standard line tension: Size-dependent contact angles of water nanodroplets". In: *J. Chem. Phys.* 147.17 (2017).

[190] Matej Kanduč et al. "Generalized line tension of water nanodroplets". In: *Phys. Rev. E* 98.3 (2018), p. 032804.

[191] Md Masuduzzaman and BoHung Kim. "Effects of dissimilar molecular interface and ion-concentration on wetting characteristics of nanodroplets". In: *Microfluid. Nanofluid.* 25 (2021), pp. 1–14.

[192] Sridhar Kumar Kannam et al. "Slip length of water on graphene: Limitations of non-equilibrium molecular dynamics simulations". In: *J. Chem. Phys.* 136.2 (2012), p. 024705.

[193] Jordi Comelles et al. "Cells as active particles in asymmetric potentials: motility under external gradients". In: *Biophys. J.* 107.7 (2014), pp. 1513–1522.

[194] David Caballero et al. "Ratchetaxis: long-range directed cell migration by local cues". In: *Trends Cell Biol.* 25.12 (2015), pp. 815–827.

[195] M Le Berre et al. "Geometric friction directs cell migration". In: *Phys. Rev. Lett.* 111.19 (2013), p. 198101.

[196] H Linke et al. "Self-propelled Leidenfrost droplets". In: *Phys. Rev. Lett.* 96.15 (2006), p. 154502.

[197] Yaerim Lee, Gustav Amberg, and Junichiro Shiomi. "Vibration sorting of small droplets on hydrophilic surface by asymmetric contact-line friction". In: *PNAS Nexus* 1.2 (2022), pgac027.

[198] Goher Mahmud et al. "Directing cell motions on micropatterned ratchets". In: *Nat. Phys.* 5.8 (2009), pp. 606–612.

[199] Young-Gwang Ko, Carlos C Co, and Chia-Chi Ho. "Directing cell migration in continuous microchannels by topographical amplification of natural directional persistence". In: *Biomaterials* 34.2 (2013), pp. 353–360.

Erklärung zur Dissertation
gemäß der Promotionsordnung vom 12. März 2020

Diese Erklärung muss in der Dissertation enthalten sein.
(*This version must be included in the doctoral thesis*)

„Hiermit versichere ich an Eides statt, dass ich die vorliegende Dissertation selbstständig und ohne die Benutzung anderer als der angegebenen Hilfsmittel und Literatur angefertigt habe. Alle Stellen, die wörtlich oder sinngemäß aus veröffentlichten und nicht veröffentlichten Werken dem Wortlaut oder dem Sinn nach entnommen wurden, sind als solche kenntlich gemacht. Ich versichere an Eides statt, dass diese Dissertation noch keiner anderen Fakultät oder Universität zur Prüfung vorgelegen hat; dass sie - abgesehen von unten angegebenen Teilpublikationen und eingebundenen Artikeln und Manuskripten - noch nicht veröffentlicht worden ist sowie, dass ich eine Veröffentlichung der Dissertation vor Abschluss der Promotion nicht ohne Genehmigung des Promotionsausschusses vornehmen werde. Die Bestimmungen dieser Ordnung sind mir bekannt. Darüber hinaus erkläre ich hiermit, dass ich die Ordnung zur Sicherung guter wissenschaftlicher Praxis und zum Umgang mit wissenschaftlichem Fehlverhalten der Universität zu Köln gelesen und sie bei der Durchführung der Dissertation zugrundeliegenden Arbeiten und der schriftlich verfassten Dissertation beachtet habe und verpflichte mich hiermit, die dort genannten Vorgaben bei allen wissenschaftlichen Tätigkeiten zu beachten und umzusetzen. Ich versichere, dass die eingereichte elektronische Fassung der eingereichten Druckfassung vollständig entspricht."

Teilpublikationen:

Kai Zhou, Marc Hennes, Berenike Maier, Gerhard Gompper, and Benedikt Sabass. "Non-equilibrium dynamics of bacterial colonies—growth, active fluctuations, segregation, adhesion, and invasion." Communications Physics 5, no. 1 (2022): 251.

Datum, Name und Unterschrift

23.11.2023 Kai Zhou Kai Zhou